Diss. ETH No. 15742

Modeling and observations of seasonal land-surface heat and water exchanges at local and catchment scales over Europe

A dissertation submitted to the
SWISS FEDERAL INSTITUTE OF TECHNOLOGY (ETH)
ZURICH

for the degree of
DOCTOR OF NATURAL SCIENCE

presented by
RETO STÖCKLI
Dipl. Natw. ETH
born 15 July 1973
citizen of Luthern (LU)

accepted on the recommendation of
Prof. Dr. C. Schär, examiner
Dr. P. L. Vidale, co-examiner
Prof. Dr. H. P. Schmid, co-examiner

2004

Front and back cover pictures:
True color visualization of the cloud-free European land surface (August and February 2003): NASA's Blue Marble Next Generation dataset, showing the seasonal changes in land surface reflectance, was derived from MODIS (MODerate resolution Imaging Spectroradiometer) MOD09A1 data by Reto Stöckli, NASA Earth Observatory.

Dedicated to
Eva
for being sunshine, wind, rainfall and heat;
essentials for a creative environment

Abstract

The land surface plays an important role in the global climate system, because it interacts dynamically with the atmosphere through manifold feedback mechanisms on a wide range of spatial and temporal scales. While on the one hand, weather and climate are known to influence vegetation phenology and its geographical distribution, soil and vegetation actively control land surface heat, water, momentum and carbon exchanges, thus influencing boundary layer development and convection. Evapotranspiration and runoff, in particular, which are balanced by precipitation, constitute the land portion of the water cycle, which is known to be a main contributor to climate variability. Knowledge about these processes and the ability to realistically model them is therefore of central importance in climate research. Simulated climate (and variability) are indeed sensitive to land surface parameterizations. There is, however, a gap between the local scale, at which land surface models and parameters are usually developed and evaluated, and the larger scales at which they are applied. This scale-gap needs to be bridged so that the high spatial and temporal dynamics of the land surface water cycle becomes part of modeled climate.

In order to help narrow the uncertainties in the modeling of seasonal-scale land-surface heat and water exchanges, local and catchment scale modeling experiments are performed in this study. Concurrently, different parameterizations are tested regarding their applicability in climate modeling, by exercising them on a wide range of climatic environments. All considered model formulations are embedded in a framework which includes ground and satellite remote sensing measurements, serving as an integration tool for the assessment of land surface processes. Satellite remote sensing is initially used to monitor vegetation state variables over Europe with a high temporal resolution, so that vegetation dynamics in land surface models can be prescribed with observed quantities. In a second stage local-scale measurements from FLUXNET are used for a process-based analysis of model results. Land surface models are applied at local scale using un-tuned large-scale and satellite-derived parameter sets. It is shown that soil storage processes play an important role in the seasonal heat and water fluxes and that vegetation biochemistry is a key component controlling the seasonal land surface water cycle. Finally, the Rhone-AGG initiative provides hydrological measurements on the catchment-scale, allowing for the exploration of scaling issues in the simulated water cycle. Catchment-scale simulations including lateral water fluxes, show that soil moisture drives runoff on the monthly time-scale and is largely controlled by evapotranspiration. While evapotranspiration was not found to be overly sensitive to runoff processes, the use of subgrid-scale topography-driven runoff provides a good simulation of the timing and magnitude of runoff at the daily to seasonal scale.

In summary, this study shows how satellite remote sensing, observations of boundary layer fluxes and ecosystem measurements can assist in developing models of the land surface water cycle which bridge the scale gaps between the processes involved; aboveground biophysics, relevant aspects of biochemistry and soil hydrology should be equally well represented in climate modeling applications.

Zusammenfassung

Die Landoberfläche spielt eine wichtige Rolle im Klimageschehen, weil sie mit der Atmosphäre über vielfältige Rückkopplungsmechanismen, die auf verschiedenen Zeit- und Raumskalen stattfinden, wechselwirkt. Wetter und Klima beeinflussen einerseits die Vegetationsphänologie und die geographische Verteilung der Vegetation, aber der Boden und die Vegetation kontrollieren andererseits Wärme-, Wasser-, Impuls und Kohlenstoffaustauschprozesse zwischen der Landoberfläche und der Atmosphäre, die dann die atmosphärische Grenzschicht und damit Konvektionsprozesse in der Atmosphäre beeinflussen. Verdunstung und Abfluss bilden auf der Landoberfläche den Wasserkreislauf und werden vom Niederschlag in Balance gehalten. Es hat sich gezeigt dass diese Prozesse einen Hauptbeitrag zur Klimavariabilität leisten. Darum ist es wichtig, mehr darüber zu wissen und die Fähigkeit zu besitzen, diese Prozesse realistisch modellieren zu können. Es wurde aber auch gezeigt, dass das modellierte Klimageschehen (und darum die simulierte Klimavariabilität) sehr von dem in der Simulation verwendeten Landoberflächenmodell abhängt. Diese Sensitivität ist vorallem darum vorhanden, weil zwischen den lokalen Skalen, wo diese Modelle entwickelt werden, und den grossen Skalen, wo sie angewendet werden, eine Lücke besteht. Es gilt, diese Lücke zu überbrücken, sodass die grosse räumliche und zeitliche Dynamik des Landoberflächen-Wasserkreislaufes Teil des modellierten Klimas wird.

Damit wir solche Unsicherheiten, die bei der Modellierung des saisonalen Landoberflächen-Wasserkreislaufes bestehen, vermindern können, werden in dieser Studie Modellexperimente durchgeführt, die von lokalen räumlichen Skalen bis zur Grösse von Einzugsgebieten reichen. Gleichzeitig werden verschiedene numerische Formulierungen auf ihre Verwendbarkeit in der Klimamodellierung getestet, indem sie in verschiedenen klimatischen Bedingungen angewendet werden. Diese Experimente sind Teil eines Systems, das Bodenmessungen und Satellitenbeobachtungen einschliesst, die es erlauben, integrativ die modellierten Landoberflächenprozesse zu analysieren: Satellitenbeobachtungen werden in einem ersten Teil gebraucht um die Vegetationsphänologie über Europa mit einer hohen räumlichen und Zeitlichen Auflösung zu überwachen. Die daraus gewonnenen Daten beschreiben dann die Vegetationsphänologie in Landoberflächenmodellen. In einem zweiten Schritt, werden quantitative Oekosystem-Messungen von FLUXNET gebraucht um die Modellresultate auf lokaler Skala prozessorientiert zu untersuchen. Die daraus gewonnenen Erkenntnisse zeigen dass Bodenspeicher-Prozesse für die saisonalen Wärme- und Wasserflüsse eine wichtige Rolle spielen und biochemische Pflanzenprozesse den Wasserkreislauf substantiell mitbestimmen können. Als letzter Schritt werden die Modelle auf Einzugsgebietsskala untersucht, wo sie mit hydrologischen Daten aus der Rhone-AGG Initiative verglichen werden. Diese Experimente erlauben es, unter Einbezug von lateralem

Wasserfluss im Boden, die Sensitivität des modellierten Wasserkreislaufes auf die verwendete räumliche Skala zu untersuchen. Erkenntnisse daraus zeigen dass Bodenfeuchte den monatlichen Gang vom Abfluss durch ihre Wechselwirkung mit der Evapotranspiration bestimmt. Auf der anderen Seite ist Evapotranspiration nicht sehr sensitiv auf den Abfluss in dem untersuchten Gebiet. Der Einbezug von von sub-skaliger Topographie in die Simulation erlaubt es, den täglichen und saisonalen Abfluss - sowohl zeitlich wie auch in seiner Grösse - zu modellieren.

Zusammenfassend zeigt diese Studie, wie Satellitenbeobachtungen, lokale Grenzschicht-Flussmessungen und Oekosystem-Messungen dabei helfen können, die Modellierung des Landoberflächen-Wasserkreislaufes voranzutreiben und die dabei entstehenden Unsicherheiten zu vermindern, indem die Lücken zwischen den dabei beteiligten Prozessen und Skalen überbrückt werden. Dazu ist es von Wichtigkeit, in Modellen sowohl die Biophysik und Biochemie der Pflanzen wie auch die Hydrologie im Boden in gleichem Ausmass zu gewichten.

Contents

Chapter 1

Introduction

1.1 Review of vegetation-climate interactions

It has been known for a long time that climate and weather influence the biosphere. As an example, plant phenology - describing the temporal pattern of plant development and growth - was first scientifically explored by the Swedish botanist Carl von Linné. In 1750 he founded an observational network consisting of 18 stations. Since the beginning of the 20th century, worldwide phenological networks are used in biometeorology to link inter-annual climatic variations to plant phenology. Recent warming trends in the northern hemisphere clearly show up in these time-series with earlier springs (flowering, leaf appearance) and later autumn dates (leaf coloring, leaf fall) (Menzel, 2000; Defila and Clot, 2001). The reason why plant phenology follows the seasonal course of the land surface climate is that vegetation physiology is strongly dependent on solar radiation, humidity, temperature and soil moisture. A deviation from species-dependent optimal environmental conditions inhibits plant physiological activity (such as transpiration or leaf growth), which is reflected for instance in the empirical relationships presented in Jarvis (1976).

Traveling between continents allowed also to recognize spatial patterns of vegetation distribution and relate them to the various climatic environments found over the globe. This was first described by the founder of biogeography, Alexander von Humboldt, early in the 19th century. He travelled in the Americas and among his broad interests in natural sciences are the geographical variations in vegetation types, dependent on latitude and elevation, as shown in his illustrations (Figure 1.1). Making a physical connection between climate and vegetation became possible because Humboldt carried a thermometer, a barometer and a hygrometer. This allowed him to measure atmospheric variables and determine vegetation composition every few hours on his expeditions (v. Humboldt, 1849). These campaigns were strenuous and led him from the tropical humid climate and evergeen vegetation at the Orinoco river (constantly being bitten by mosquitoes and visiting unknown indigenous tribes) up to the over 6300m high Chimborazo mountain (despite suffering from strong altitude sickness) where snow and ice prevent vegetation growth. His measurements finally allowed to state that climatic conditions largely determine the earth's vegetation type distribution:

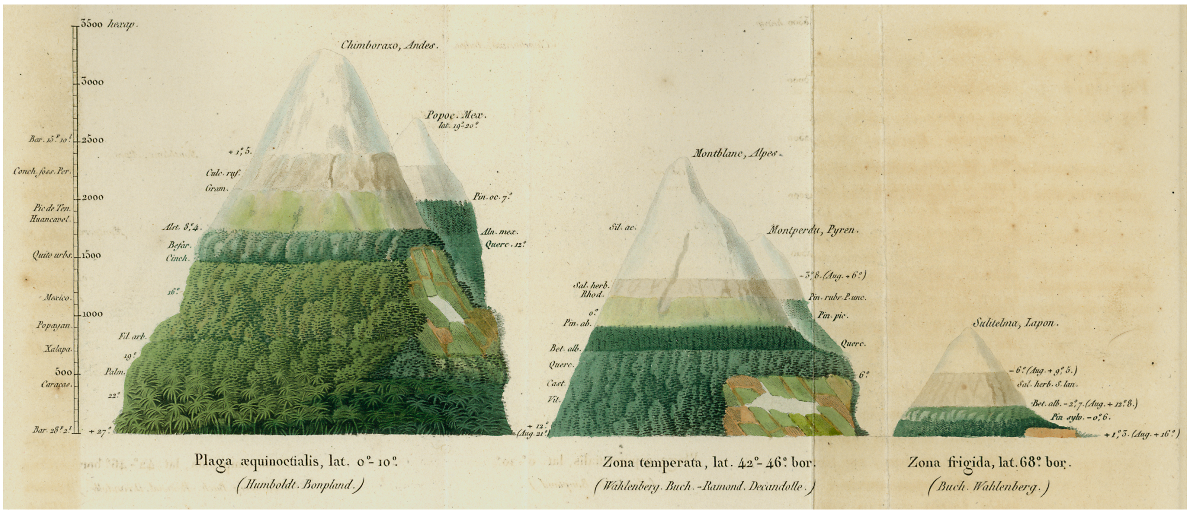

Fig. 1.1: Climatic zones and their vegetation distribution, reproduced from v. Humboldt (1817)

"Even if nature does not produce the same species in similar climates, nevertheless the vegetation exhibits the most striking visual similarities in habit even in the most distant regions. This phenomenon is one of the most remarkable in the history of organic creations ..." (Alexander von Humboldt)

These observations were an important step to understanding time and space patterns of vegetation-climate interactions; but only the availability of better measurement tools and numerical modeling allowed to finally explore the processes behind them. Climate research of the last decades has shown that land surface also influences climate and weather through manifold feedback mechanisms (e.g. described well in Bonan (2002)). To various degrees the land surface determines its radiation, energy and water balance: net radiation (R_n) depends on the vegetation and soil albedo, which varies seasonally with vegetation phenology or on shorter time scales with rain or snowfall. R_n is partitioned into surface-atmosphere sensible (H) and latent (LE) heat fluxes, where LE largely depends on soil water. These turbulent fluxes are controlled by surface roughness, which differs by vegetation type, and by surface layer thermal stability. The atmospheric state, especially convection, can be influenced by land cover type (Pielke Sr, 2001b). Vegetation roughness and snow in high latitudes influence the surface radiation balance and turbulent fluxes (Betts et al., 2001). On global scale tropical deforestation can increase surface temperatures and temperate latitude land cover conversion to crops decreases canopy temperatures (Bounoua et al., 2002). These results can be explained with changes in albedo and LE, providing surface cooling, and changes in the diurnal temperature range, as e.g. shown by Collatz et al. (2000). Interannual variability of surface fluxes is largely related to vegetation phenology (Guillevic et al., 2002). These studies and others reviewed in Pitman (2003) exemplify that the land surface vegetation is not only following the spatial and temporal pattern of climate but also has an effect on the atmosphere and the near-surface climate because plants can regulate their climatic environment by changing physiological and structural properties. These studies, however, are not a proof that the climate system itself is affected by land surface processes. Early global modeling experiments reviewed by Charney et al. (1977) showed sensitivity of climate dynamics to land surface properties like albedo or roughness length. Evapotranspiration produced by land-surface vegetation is an important factor for the earth's climate (Shukla and Mintz, 1982). Tropical land cover changes influence tropical convection but also northern hemisphere winter climate (Chase et al., 2000). Interannual covariability between surface temperature and vegetation is linked globally with teleconnections associated with the El Niño-Southern Oscillation (ENSO) and the Arctic Oscillation (AO) (Buermann et al., 2003). The land surface water cycle is sensitive to regional land cover changes (Reale and Dirmeyer, 2000; Reale and Shukla, 2000; Heck et al., 2001) and to global scale specification of soil water holding capacity (Milly and Dunne, 1994). Soil moisture is the key to seasonal-scale feedbacks between the land surface and the climate (Pielke Sr et al., 1999; Schär et al., 1999) since it offers a monthly-scale terrestrial water storage mechanism (Koster and Suarez, 2001). Schär et al. (1999) further explore soil moisture - rainfall relationships by proposing a close interaction between soil moisture, surface radiation, boundary layer development and cloudiness and proposes that the convective instability is enhanced for wet soils through increased net surface radiation and higher values of moist entropy in the boundary layer. While in most studies (e.g. Koster et al. (2000b), Douville (2003) or Seneviratne et al. (2002)) soil moisture - precipitation feedback mechanisms are explained through root soil moisture, Eltahir (1998) suggests that the convective state of the atmosphere is linked to moisture in the shallow top-soil, which is successfully tested by Zheng and Eltahir (1998) over Western Africa.

Despite the intellectual progress shown above there is a need to further explore and understand processes governing vegetation-climate interactions. Future climate is expected to feature a higher global temperature and regional changes in precipitation due to anthropogenic greenhouse gas emissions, a higher atmospheric CO_2 level and changed land use due to deforestation and agricultural practice (Intergovernmental Panel on Climate Change, 2001). The above modeling results are largely based on the radiative effects of enhanced atmospheric CO_2 on the global climate system and include biophysical feedback mechanisms between the land surface and the atmosphere but they do not include structural and physiological effects of enhanced CO_2 and altered climate on vegetation (and therefore their feedback on the climate system). Stomata on plant leaves regulate CO_2 uptake to maximize assimilation and minimize water loss - the two processes are closely linked. Sellers et al. (1996a) for instance find that physiological effects with doubled CO_2 concentration enhance carbon uptake and amplify the prognosed surface temperature increases in future climate due to reduced evaporative cooling. These effects are partially compensated by structural vegetation changes (increased leaf area) and longer growing seasons in future climate (Betts et al., 2000). Under steady-state conditions CO_2 uptake is almost balanced by soil respiration from heterotrophic decomposition of dead biomass, where only a small fraction of carbon is stored in the soil for longer periods. The long term evolution of carbon fluxes is of particular importance in the context of enhanced anthropogenic CO_2 emissions and human-induced land-cover changes (both being a CO_2 source for the atmosphere) since the land-surface vegetation can act as a potential sink for these emissions. Soil respiration on the other hand is very sensitive to temperature and moisture and therefore depends on the state of future climate, and enhanced assimilation is most likely to result in enhanced soil respiration with a time lag of tens to hundreds of years (Cox et al., 2000). Cramer et al. (2001) present evidence that the enhanced carbon sink of land surface vegetation due to enhanced CO_2 is most likely to be offset by climate change induced increase of soil respiration and reduced carbon uptake due to tropical land cover changes.

1.2 Review of modeling approaches

The above findings are largely based on climate model experiments. Land surface processes in climate models are simulated by Land Surface Models (LSMs). They are required to represent processes that cover typical climate model spatial resolutions of 100km (or larger) and time resolutions of minutes to the total integration time of the climate simulation. Reviewed in Sellers et al. (1997a), Chen et al. (2001) and Pitman (2003), three generations of LSMs have been developed over the last three decades.

1. The first LSM, the so-called bucket model (Manabe, 1969) was intended to provide a lower boundary condition for atmospheric models by solving the surface energy balance equation. It ignored soil heat storage and a simple bucket stored precipitation from which evaporation was controlled by bucket water content. Neglecting plant physiological processes, this model required very few empirical parameters. This scheme allowed numerical experiments testing climate sensitivity to albedo or surface roughness.

2. Empirical parameterization of stomatal conductance as a function of environmental variables (Jarvis, 1976) and the use of the force-restore soil moisture and temperature scheme (Deardorff, 1978) in combination with a bulk canopy layer allowed the development of second-generation schemes. Two prominent second generation schemes are BATS (Dickinson et al., 1986) and SiB (Sellers et al., 1986). They explicitly simulate a biophysical control on surface water fluxes. The use of these models allowed to explore the impact of land cover change on climate and land surface hydrology.

3. A mechanistic formulation of stomatal conductance (Ball et al., 1987; Ball, 1988) as a function of carbon assimilation by Farquhar et al. (1980), motivated the development of third-generation models, namely SiB 2 (Sellers et al., 1996d), LSM (Bonan, 1996), MOSES (Cox et al., 1998) and most recently CLM (Dai et al., 2003). Progress in satellite remote sensing during the 1990s furthermore allowed to relate radiative properties of vegetation to structural and physiological parameters and thus reduce the large parameter sets required in second-generation schemes. In additions to applications of first- and second-generation LSMs, third-generation LSMs help to explore physiological responses to enhanced atmospheric CO_2 and to link the global carbon and water cycle.

The land surface is not simply a static boundary as prescribed by first-generation LSMs and is also not primarily exchanging water as controlled by environmental conditions, such as formulated in second-generation LSMs. The flux of water through stomata is regulated by stomatal conductance, but empirical relationships (Jarvis, 1976) governing this exchange are only known for a discrete number of vegetation types and are bound to current climatic conditions. However, the same plant types grow differently in other climatic environments and future climates with enhanced atmospheric CO_2 can create physiological changes in stomatal conductance (Bounoua et al., 1999). It has been recognized that the land-surface vegetation represents an interactive medium, able to minimize water loss to maximize carbon assimilation, this relationship being the mindset of third-generation LSMs (Pielke Sr, 2001a). Only the mechanistic - rather than empirical - knowledge of the functioning of stomata and leaf photosynthesis allows to model the spatial and temporal dynamics of vegetation biophysics. The choice of CO_2 concentration as a prognostic variable in third-generation LSMs makes it straightforward to model the biospheric sink of CO_2 in climate models and to include the physiological responses of plants to enhanced CO_2 in future climate. Also, photosynthetic activity and carbon uptake are starting to become verifiable from ecosystem to global scale by use of tower flux measurements, aircraft measurements and satellite remote sensing (Canadell et al., 2000).

Despite all these model developments two major drawbacks of third generation models can still be formulated: they firstly do not dynamically simulate structural changes in vegetation, and secondly, soil nutrients and carbon are either given as boundary conditions or simply diagnosed from other state variables. Both these processes are of importance for decadal to centennial climate simulations (Betts et al., 1997; Dickinson, 2001), where carbon and nutrient pools, vegetation distribution and density respond to climatic change and variability at different time scales. So-called dynamic global vegetation models (DGVMs, e.g. TRIFFID by Cox (2001)) have been developed, as reviewed by Foley et al. (2000) and Arora (2002), and allow vegetation structure to react to environmental conditions. Sensitivity of vegetation distribution and structure to climate, as simulated by such models, is demonstrated by Ciret and Henderson-Sellers (1997) and Cramer et al. (2001), and their use in coupled simulations is shown for instance by Levis et al. (2000) and Eastman et al. (2001). Arora and Boer (2003) furthermore explore the use of dynamic root allocation in such models, which is of importance since up to 50% of the total plant biomass is allocated as root biomass, depending on age, plant type and environmental constraints. Dynamic growth of above-ground vegetation and roots depends on assimilation which in turn is controlled by nutrients supply from atmospheric deposition, or decomposition of dead biomass into soil nitrogen and carbon stores. It is important to include nutrient limitation on natural vegetation (Dickinson, 2001; Pitman, 2003), especially considering higher photosynthesis rates in an enhanced CO_2 environment. The integration of biogeochemistry in climate modeling is for instance demonstrated by Parton et al. (1998) and Dickinson et al. (2002). Treatment of the full carbon and nutrient cycles inside a modern LSM allows for their incorporation in the emergent class of GCMs, called Earth System Models: in this context these new land surface processes can meaningfully interact with other components of the earth system, e.g. aerosols, atmospheric chemistry and ocean biogeochemistry. A justification for their use in climate research is given in Fung (2001) and first GCM experiments with such a modeling framework by Cox et al. (2000) present an even stronger accelerated global warming in comparison to past simulations without an interactive land surface.

1.3 Problems of current approaches

- The usability of dynamic carbon, nutrients and vegetation in climate modeling is in its early stages. Such an integrative approach requires the individual components to be tested and validated on many temporal and spatial scales before they can be used in coupled experiments. The validation of biogeochemical parameterizations is currently limited due to missing large-scale and long-term measurements of below-ground processes. Above-ground vegetation distribution and structure can nowadays be derived by satellite remote sensing on global scales (Hansen et al., 2000; Los et al., 2000). Since the above review shows that the dynamics of these properties vary over decadal to centennial time-scales, where only limited (e.g. tree ring analysis) validation data exists, the usability of these new fully prognostic biogeochemistry models for future climate predictions might be questioned at this time. But the task of interactively linking terrestrial ecology to atmospheric dynamics in climate modeling is a noble one because it offers a tool to explore and understand past climatic variations (Petit et al., 1999) and to narrow uncertainty of future climate predictions (Intergovernmental Panel on Climate Change, 2001).

- LSMs of varying complexity as described above have already been applied for three decades in climate modeling, but nevertheless there is no consensus in the community on the superiority of one or the other approach. Gedney et al. (2000) argue that the full range of LSMs (including first generation schemes) is still used for todays climate research and presents GCM experiments demonstrating the sensitivity of surface hydrology to the scheme used. Henderson-Sellers et al. (2003) review LSMs used in AMIP II (Atmospheric Model Intercomparison Project) GCM simulations and find a clustering of results between model generations outlined in the previous paragraphs, earlier approaches generally simulating more LE than recent schemes. They show that the land surface climate in todays GCM simulations is still largely dependent on the used LSM. The interpretation of GCM-type model intercomparison studies is limited, however, because long-term land surface validation data for such studies are generally not available. At the local scale, field campaigns (e.g. FIFE (Sellers et al., 1988), BOREAS (Sellers et al., 1997b), NOPEX (Halldin et al., 1999), LBA (Avissar et al., 2002)) and long-term surface flux and ecosystem measurement initiatives (e.g. FLUXNET (Baldocchi et al., 2001)) provide a thorough validation source for LSMs, and allow for process-based studies. Local-scale model intercomparisons such as PILPS 2(a) (Project for the Intercomparison of Land-Surface Parameterization Schemes) use these data to explore the performance of LSMs used in climate research. Chen et al. (1997) find that for a temperate grassland (Cabauw), simulated LE (H) differ by 30 $\mathrm{Wm^{-2}}$ (25 $\mathrm{Wm^{-2}}$) in the annual mean, and annual runoff shows scheme-dependent ranges of 315 mm. These differences were approximately halved upon exclusion of first generation schemes. PILPS results in other climatic environments show similar inter-model differences and are discussed in Pitman and Henderson-Sellers (1998) and Pitman et al. (1999). Findings by Intergovernmental Panel on Climate Change (2001) (Climate Change 2001: Working Group I: The Scientific Basis, Section 8.5.4.3) show that this uncertainty limits projections of future climate, and justifies further research about the validity of processes simulated by todays LSMs.

- The successful validation of LSMs at the local scale does not guarantee that they can be upscaled to large-scale grids used in GCM-type simulations. Firstly, required vegetation and soil parameters can not always be determined at larger scales and secondly, their area-average values are problematic due to non-linear dependence between parameters and processes. While effective and area-integrated parameters for biophysical vegetation processes can be derived from satellite remote sensing, soil moisture-runoff processes and their parameters vary by orders of magnitude on very small scales (Western et al., 2002). In detailed hydrological models these processes are mostly explicitly resolved, because of the high dependence of runoff on small-scale soil and topographical variations. Due to high computational costs such an approach is not an option in climate modeling. But considering the close linkage of soil moisture, runoff and evapotranspiration (Koster and Milly, 1997), the grid-scale treatment of soil moisture is problematic and can introduce scaling-errors in surface heat and water fluxes. Several model intercomparison studies have been aiming at exploring these scaling issues. PILPS 2(c) (Wood et al., 1998; Lohmann et al., 1998; Liang et al., 1998) revealed a general overprediction of runoff and therefore an underprediction of LE in summer (dry season), which was compensated by an exaggerated LE during winter. The Rhone-AGG model-intercomparison (Boone et al., 2004) showed that todays LSMs simulate very different runoff, but that subgrid-scale soil-moisture improves runoff. These uncertainties of soil moisture related processes due to scaling contrasts their application in current climate models, and it was shown for instance by Ducharne et al. (1998), Gedney et al. (2000), Gedney and Cox (2003), Douville (2003) that climate as simulated by todays GCMs is sensitive to the used soil moisture and runoff parameterizations. These kowledge gaps clearly justify further research on scaling issues of the land surface water cycle.

1.4 How to narrow these uncertainties

As shown above, the simultaneous use of land-surface processes and parameters in coupled climate model experiments reveals a large number of uncertainties, especially in the computation of the seasonal land-surface heat and water balance. The application of LSMs in climate research requires that underlying simulated processes hold for a wide range of spatial and temporal scales. A thorough testing can help to reduce these uncertainties, but is dependent on the availability of land-surface parameters, driver data and validation data. Progress, as shown above, is especially hindered by the lack of long-term validation data on global scales, which would allow for process-based studies in this field. The main motivation for this study is therefore to explore these land-surface processes on local and catchment scale, where validation data allows for process-based comparisons between the model world and the real environment. The availability of a high number of observations in both space and time is of central importance for such a study, since LSMs include a complex network of process-dependencies. Only if some of these dependencies can be temporarily bound to observables in modeling experiments, interpretation of results is possible and therefore the following is needed at a range of sites:

- land-surface parameters to prescribe the state of vegetation and soil in LSMs
- long term and continuous meteorological time-series at various spatial scales

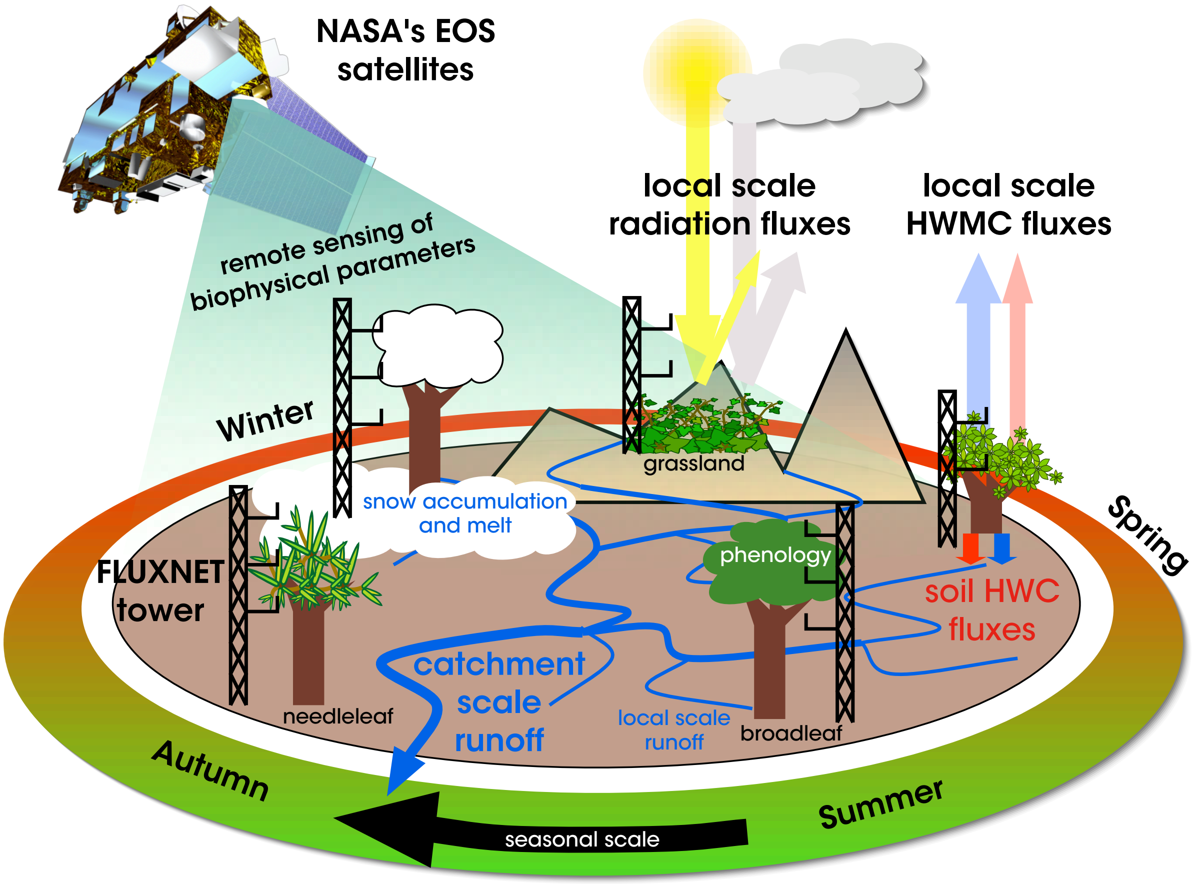

Fig. 1.2: Integrating satellite remote sensing, land surface modeling and ecosystem measurements

- validation data which can be directly related to LSM prognostic variables

To achieve the above outlined goal, this study largely follows the theoretical framework and ideas outlined by Running et al. (1999) and Turner et al. (2004), displayed in Figure 1.2, by integrating satellite remote sensing, land surface modeling, ecosystem observations and measurements of the boundary layer fluxes of heat, moisture and momentum. The three chapters in this study are therefore ordered in a logical sequence to meet the requirements for this framework:

1. Chapter 2 (Stöckli and Vidale, 2004) assesses the seasonal and interannual variations of vegetation phenology and photosynthetic activity over Europe by satellite remote sensing and creates a biophysical land-surface parameter dataset for use as vegetation parameters in LSMs. In contrast to fixed vegetation parameters (unrealistic, due to the known seasonal and interannual variability of vegetation phenology, as shown above), global-scale satellite remote sensing (e.g. by NASA's Earth Observing System EOS) provides continuous global fields of ecosystem measurements with a high spatial and temporal resolution (Running et al., 2004). These are directly linked to the land-surface carbon uptake, and as described above this carbon uptake is a primary driver for the land surface heat and water budgets. Satellite

remote sensing as a tool is therefore justified since it reduces degrees of freedom in LSM simulations by prescribing model phenological parameters and adding realism to simulations because it provides observed quantities of global extent.

2. Chapter 3 (Stöckli and Vidale, 2005) explores the processes that drive seasonal land-surface fluxes by use of satellite remote sensing, modeling and tower flux observations. Land surface parameters derived from satellite remote sensing (Chapter 2) are used in single-column modeling experiments. As shown above, the large intermodel-differences in land surface fluxes require to assess the underlying processes and to test the relevance of each process in the full range of climatic environments, so that their application will hold in a global experiment. This is achieved by using local-scale surface fluxes and ecosystem measurements from the long-term and global monitoring network FLUXNET (Baldocchi et al., 2001), providing continuous time-series of meteorological driver data for off-line and local scale LSM simulations. Soil and vegetation data (soil moisture, temperature, turbulent surface fluxes) then allow a direct comparison to model prognostic variables in a process-based analysis. Although these are local scale measurements, their global distribution makes them suitable for analysis of modeled land surface processes over a wide range of vegetation types and climatic environments.

3. Chapter 4 (Stöckli et al., in preparation) aims at evaluating scaling issues in the land surface water cycle at catchment scales by use of satellite remote sensing, modeling and observations, since local-scale model-tower intercomparisons alone offer no means to study the water cycle on larger scales. For this purpose, data from the catchment-scale initiative Rhone-AGG (Boone et al., 2004) is used in off-line modeling experiments, and satellite remote sensing provides area-integrated as well as spatially and temporally varying biophysical land-surface parameters at these larger scales. In comparison to local-scale experiments, validation data at catchment-scale is limited to runoff, but the use of snow depth and soil moisture measurements furthermore link observed processes to modeled ones. As in Chapter 3 validity of catchment-scale processes can be tested by choosing a range of catchments varying in both geography and climate. The influence of scaling on simulated soil hydrological processes in these different climatic environmments as well as the sensitivity of heat and water fluxes to such scaling procedures is tested in this chapter.

In the Appendix this study's enhancements to existing modeling technology are presented in the following order: the first part of the Appendix describes the derivation of biophysical land surface parameters from the EFAI-$NDVI$ dataset (Chapter 2). The second part (Vidale and Stöckli, 2005) describes a new solution scheme for the LSM SiB 2 (Sellers et al., 1996d), including a prognostic canopy-air-space storage capability for heat, water and carbon, which is used in Chapters 3 and 4. The third part of the Appendix describes both the vertical and the lateral soil moisture and runoff transfer schemes used in Chapter 4.

Chapter 2

European plant phenology and climate as seen in a 20 year AVHRR land-surface parameter dataset

European plant phenology and climate as seen in a 20 year AVHRR land-surface parameter dataset *

Reto Stöckli † and Pier Luigi Vidale ‡

ABSTRACT

Vegetation distribution and state have been measured since 1981 by the AVHRR (Advanced Very High Resolution Radiometer) instrument through satellite remote sensing. In this study a correction method is applied to the Pathfinder $NDVI$ (Normalized Difference Vegetation Index) data to create a continuous European vegetation phenology dataset of a 10 day temporal and 0.1° spatial resolution; additionally, land surface parameters for use in biosphere-atmosphere modeling are derived.

The analysis of time-series from this data set reveals, for the years 1982-2001, strong seasonal and interannual variability in European land surface vegetation state. Phenological metrics indicate a late and short growing season for the years 1985-1987, in addition to early and prolonged activity in the years 1989, 1990, 1994 and 1995. These variations are in close agreement with findings from phenological measurements at the surface; spring phenology is also shown to correlate particularly well with anomalies in winter temperature and winter NAO index. Nevertheless phenological metrics, which display considerable regional differences, could only be determined for vegetation with a seasonal behaviour.

Trends in the phenological phases reveal a general shift to earlier (-0.54 days/year) and prolonged (0.96 days/year) growing periods which are statistically significant, especially for central Europe.

*International Journal of Remote Sensing, 2004, Volume 25, Number 17, pages 3303-3330

†Reto Stöckli, Institute for Atmospheric and Climate Science, Winterthurerstrasse 190, 8057 Zürich, Switzerland. e-mail: stockli@env.ethz.ch, phone: +41 1 635 5209

‡Pier Luigi Vidale, Institute for Atmospheric and Climate Science, Winterthurerstrasse 190, 8057 Zürich, Switzerland. e-mail: pier-luigi.vidale@ethz.ch, phone: +41 1 635 5218

2.1 Introduction

Interactions between the land surface and the atmosphere include turbulent heat, moisture, momentum and carbon exchanges, which can largely determine the state of climate and its variations in the near-surface continental climate (Chen et al., 2001; Pielke Sr, 2001a). In addition, vegetation physiology and phenology are very sensitive to climate forcings through several feedback mechanisms at various time scales (Bounoua et al., 1999). It is well known, for instance, that plants assimilate carbon in the process of photosynthesis, while losing water through transpiration (Sellers et al., 1997a): the terrestrial water and carbon cycles are closely linked by these processes. Keeling et al. (1996) examine CO_2 records from the Mauna Loa station from 1964 to 1994 and find that amplitudes in the yearly CO_2 cycle (linked to vegetation activity) have increased by 20%. They propose to attribute those trends to increased assimilation by land vegetation, associated with anthropogenic global climate change.

The timing of phenological events is affected by naturally changing local environmental conditions as well as by biological factors like diseases, soil moisture, nutrients and age of the individual plants (Menzel, 2000). Many phenological phases used in biometeorology, such as leaf unfolding and leaf colouring, are primarily driven by local climatic conditions, like temperature and snow cover during winter and early spring. Ground-measured vegetation phenology has been studied since the 18th century (Defila and Clot, 2001; Menzel, 2000; Roetzer et al., 2000): data from International Phenological Gardens (IPG) from 1959-1996 and from wild plants in Switzerland, show high sensitivity of vegetation dynamics to interannual climate variations. These studies have recently been linked to the observed global warming. Phenological events in spring are known to be especially sensitive to climatic influences: in the IPG phenological records springs have advanced over 6.3 days and autumn has been delayed by 4.5 days since the early 1960's.

The variability of vegetation state and function motivates the creation of high-resolution vegetation parameters varying dynamically over space and time. These parameters can be used to model the complex soil-vegetation-atmosphere interactions but also to assess the long-term changes in land use and vegetation physiology over a large area. During the last two decades many efforts have been made to better integrate land surface processes in climate modeling: Sellers et al. (1997a) and more recently Pielke Sr (2001a) provide thorough reviews of land surface models used in climate research. These mathematical formulations have evolved during the last two decades from simple abiotic relationships, e.g. the bucket model (Manabe, 1969), to sophisticated biogeochemical models like SiB 2 (Sellers et al., 1996d) and LSM (Bonan, 1996), which include a treatment of leaf photosynthesis and CO_2 exchange. While it is possible to derive biophysical vegetation parameters for use in these models from existing land cover surveys, published in the form of maps (Matthews, 1983; DeFries et al., 1998; Loveland et al., 2000; Hansen et al., 2000), this approach accounts exclusively for spatial variability, neglecting temporal variability. The knowledge of temporal variability of vegetation function is, however, a key issue to meet the requirements of the United Nations Framework Convention on Climate Change (UNFCCC) and the Kyoto Protocol, in order to quantify the carbon pools and exchanges on local and on global scale.

The knowledge of vegetation phenology for entire ecosystems and on global scale has thus in past decades been limited, either in space or in time. In comparison to the ground-based global vegetation classifications by Matthews (1983) and Wilson and Henderson-Sellers (1985), satellite remote sensing now offers the possibility to estimate vegetation phenology on the global scale with a high temporal frequency. Since the 1980's multi-spectral satellite observations from the National Oceanic and Atmospheric Administration's (NOAA) Polar Orbiting Environmental Satellites (POES) provide daily global coverage datasets of visible and near-infrared surface reflectances. From those the Normalized Difference Vegetation Index ($NDVI$) can be derived as this has been shown by Justice et al. (1985), Tucker and Sellers (1986), Reed et al. (1994), Viovy and Saint (1994), Myneni et al. (1997), Champeaux et al. (2000), Los et al. (2001) and Zhou et al. (2001). The $NDVI$ exploits the spectral properties of green plant leaves and is an estimator for the radiation used within the photosynthesis process occuring in leaves. Asrar et al. (1985), Tucker and Sellers (1986), Sellers et al. (1996b) and Los (1998) showed that the temporal evolution of the Fraction of Photosynthetically Active Radiation absorbed by the green leaves ($FPAR$), the Leaf Area Index (LAI) and other biophysical vegetation parameters can be empirically estimated from $NDVI$ with the use of land cover type dependent vegetation constants. Sets of land surface parameters can be found on low resolution and global scale in the ISLSCP dataset collection (Sellers et al., 1996c) for the years 1987/1988, extended by Los et al. (2000) for the 9-year period 1982-1990.

Satellite sensor data can also provide a good means to verify trends of ground observed vegetation activity. Myneni et al. (1997) have investigated the 1981 to 1991 AVHRR $NDVI$ record from the GIMMS and the Pathfinder dataset for the northern hemisphere. They have detected an advance in the active growing season of 8±3 days and a delay in the declining phase of 4±2 days over this decade. Zhou et al. (2001) look at the northern hemisphere vegetation activity derived from AVHRR $NDVI$ and land surface temperature records during 1981 to 1998 and find an increase in mean $NDVI$ for Eurasia and north America.

Remote sensing of land surface properties is, however a complex and problematic task. Atmospheric absorption and scattering by gas molecules and aerosols, persistent cloud cover, viewing geometry effects, illumination conditions and technical difficulties limit the use of these satellite measurements. Much research has been accomplished in the last two decades in order to correct and calibrate multi-temporal $NDVI$ data (Tucker and Matson, 1985; Holben, 1986; Goward et al., 1991; Gutman and Ignatov, 1995; Cihlar et al., 1994; Sellers et al., 1996b; Los, 1998; Los et al., 2000).

In this study we use the highly processed NOAA/ NASA Pathfinder $NDVI$ dataset, which is already corrected for many of the problems mentioned above. From the Pathfinder $NDVI$ a continuous 20 year vegetation phenology dataset is extracted and biophysical land surface parameters covering the period from 1982-2001 are derived with high spatial and temporal resolution. We focus on Europe and study regional variability seen in vegetation dynamics. The methodology involves the use of a refined correction algorithm based on Los et al. (2000) to extract the vegetation phenology from satellite data. Long term surface observations in both phenology and climate over continental Europe make it possible to conduct meaningful statistical intercomparisons and this offers the opportunity to further validate the soundness and usefulness of these land surface products. Inter-annual variability and regional differences in phenology in particular, have not been analysed previously at this spatial and temporal scale over this region.

In Section 2.2 the methodology used to derive the set land surface parameters from the NASA/NOAA Pathfinder $NDVI$ is presented. An analysis of interannual and seasonal variation of these land surface parameters is presented in Section 2.3. The relationship between interannual climate annomalies and vegetation phenology are examined for a number of European sub-domains. A discussion of the results follows in Section 2.4.

2.2 Data and methodology

2.2.a Pathfinder $NDVI$

The $NDVI$ exploits the spectral properties of green plant leaves, which absorb incoming radiation in the visible part of the spectrum (AVHRR VIS channel: 0.62-0.7μm) and strongly reflect light in the near-infrared wavelengths (AVHRR NIR channel: 0.74-1.1μm). This ratio has low values ranging from -0.2 to +0.1 for snow, bare soil, glaciers, rocks and rises to around 0.2 to 0.8 for green vegetation. $NDVI$ is an estimator for the radiation used within the photosynthetic processes occuring in leaves.

For the derivation of the 1982-2001 biophysical surface parameters we used the NOAA/ NASA Pathfinder $NDVI$ dataset (James and Kalluri, 1994). The data are collected by the AVHRR (Advanced Very High Resolution Radiometer) instrument on board the NOAA POES (Polar Orbiting Environmental Satellite) platforms. These operational satellites are successively replaced at failure and are supposed to provide a continuous and consistent data record into the future. The Pathfinder $NDVI$ dataset is corrected for Rayleigh scattering by applying the radiative transfer model by Gordon et al. (1988). Ozone absorption in the signal is removed by the estimation of the atmospheric ozone column from daily TOMS (Total Ozone Mapping Spectrometer) measurements. Each satellite (NOAA 7, 9, 11 and 14 - only the afternoon overpass satellites were used by the Pathfinder project) flown during the period 1981-present has been subject to instrumental degradation during the operational period, which was accounted for by fitting a time dependent calibration algorithm Rao and Chen (1996) for each individual channel. The $NDVI$ is calculated from the AVHRR channel 1 visible (VIS) and channel 2 near-infrared (NIR) reflectances by taking the ratio:

$$NDVI = \frac{NIR - VIS}{NIR + VIS} \tag{2.1}$$

Within the Pathfinder $NDVI$ dataset these daily swath data are geolocated and gridded at 8km resolution and composited over 10 day periods with the maximum value composite (MVC) algorithm (Holben, 1986) to a global coverage. The dataset is not corrected for aerosols (for instants volcanic eruptions such as Mt. Pinatubo in June 1991 or smoke from forest fires), water vapor absorption and illumination and viewing geometry effects. Some of these disturbances are compensated in the $NDVI$ since it is basically a ratio between two spectral bands. Zhou et al. (2001) assess the effect of the solar zenith angle to $NDVI$ as weak, especially in seasonal and inter-annual terms. An average registration error of 6km was observed by Holben (1986) in the geolocated AVHRR data. Prior to any corrections, an overall absolute error in the $NDVI$ in the order of 0.1-0.2 must be considered (Los, 1998). The lack of a good pre-calibration in the AVHRR Pathfinder $NDVI$ dataset is problematic for the derivation of spatio-temporally consistent land surface parameters. For the generation of the 10 day composites the cloud mask is not used. Also, anomalously high data values ($NDVI > 0.8$) are found and pixels with high solar zenith angles are set to missing data values. Yearly time-series of the NOAA Pathfinder $NDVI$ for various areas and years are found in Figure 2.1 (thin solid lines) and show some of the inconsistencies. More sophisticated atmospheric correction schemes are used for the MODIS (MODerate resolution Imaging Spectroradiometer) data processing (see e.g. Vermote et al. (1997)).

The current in-operation POES afternoon satellite NOAA-14 is continuously drifting westwards, which leads to a later equatorial overpass. In Figure 2.2 time-series of $NDVI$ for the years 1981-2001 are shown. Over the Sahara desert (Figure 2.2(a)) the higher solar zenith and instrument angles leads to a decreasing $NDVI$ signal beginning in late 2000. For vegetated areas this effect is partly compensated as this can be seen in Figure 2.2(b), but the degradation of the satellite signal is problematic for our application, since northern Europe will have larger data dropouts during winter time. The NASA DAAC does not recommend to use the newest 2001 Pathfinder data for scientific purposes (http://daac.gsfc.nasa.gov/CAMPAIGN_DOCS/LAND_BIO/AVHRR_News.html) and has stopped to produce the dataset on a regular basis by September 2001. A new generation of sensors like MODIS (launched onboard the TERRA satellite in 1999 and onboard the AQUA satellite in 2002) can provide land surface data for this time period.

2.2.b Correction methodology

To create a consistent dataset of vegetation phenology, we analyse and correct yearly time-series of Pathfinder $NDVI$ over the European continent at a 10 day temporal and 0.1° spatial grid for the period from 1982 - 2001. Two steps are involved in the spatio-temporal interpolation process:

1. Replacement of processing artifacts and no-data values in the dataset by spatial interpolation (Section 2.2.c)
2. Adjustment of the $NDVI$ time-series by using a temporal interpolation procedure (Section 2.2.d)

The following three assumptions can be made when extracting time-series of the state of land surface vegetation from the error contaminated satellite remotely sensed $NDVI$:

- The vegetation phenology follows a repetitive seasonal cycle (Moulin et al., 1997) and $NDVI$ values vary smoothly with time (Sellers et al., 1996b).
- During the summer outliers in $NDVI$ time-series are the result of either cloud cover or atmospheric disturbances. These effects tend to decrease $NDVI$ values (Holben, 1986; Los, 1998).

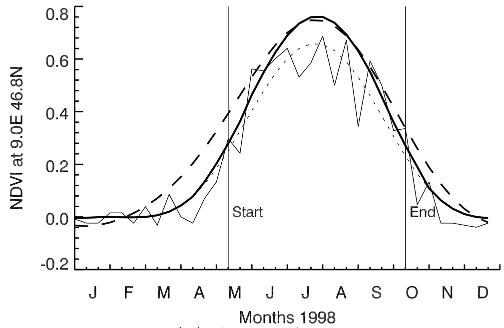

(a) Swiss Alps

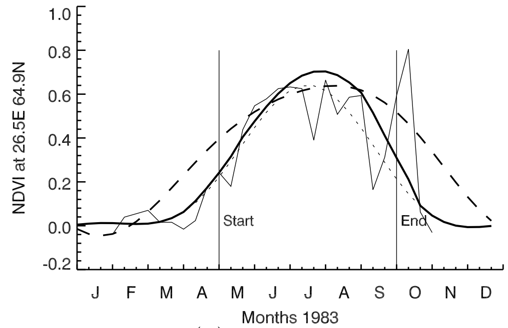

(b) Finland

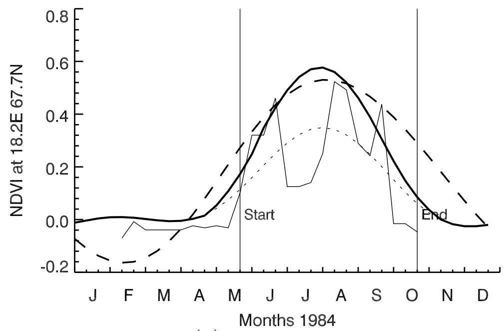

(c) Norway

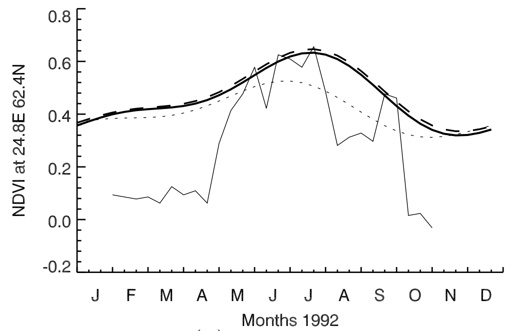

(d) Finland

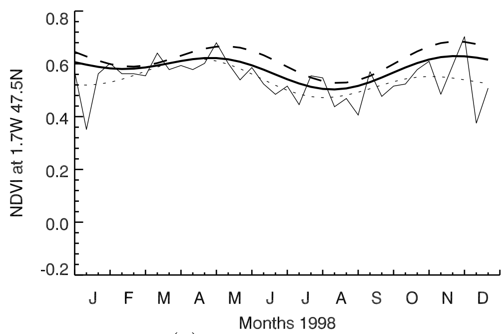

(e) NW France

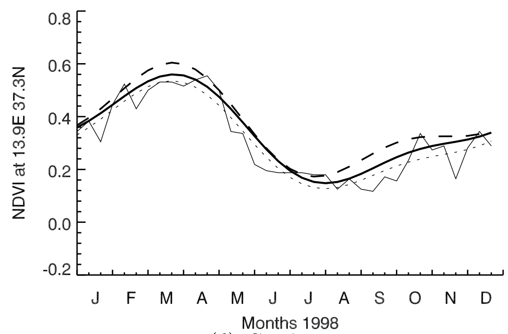

(f) Sicily

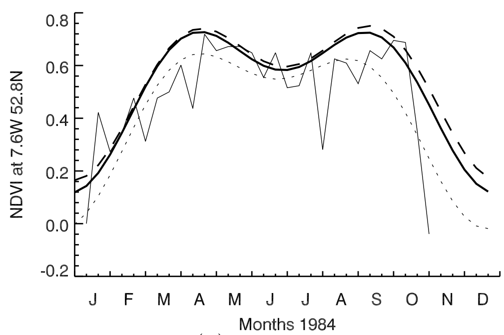

(g) Ireland

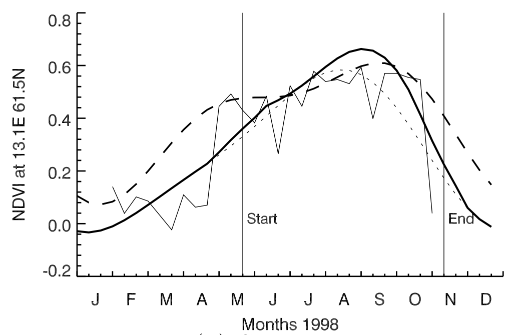

(h) Sweden

Fig. 2.1: Pathfinder $NDVI$ time-series(thin solid), Fourier adjusted with an unweighted scheme (dotted), weighted after Sellers et al. (1996b) (dashed) and with the EFAI-$NDVI$ method discussed in this paper (thick solid)

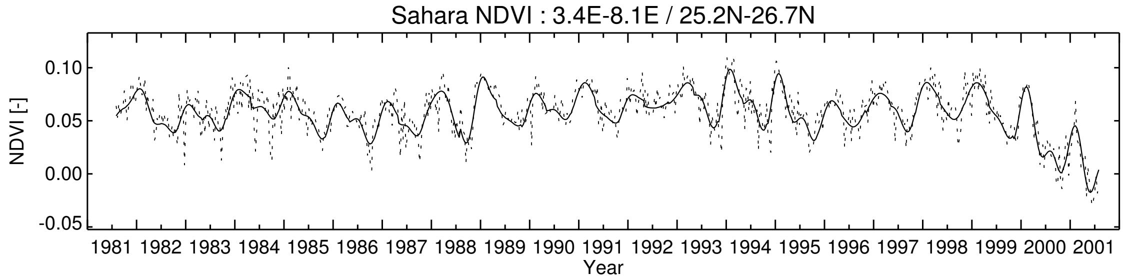

(a) Sahara

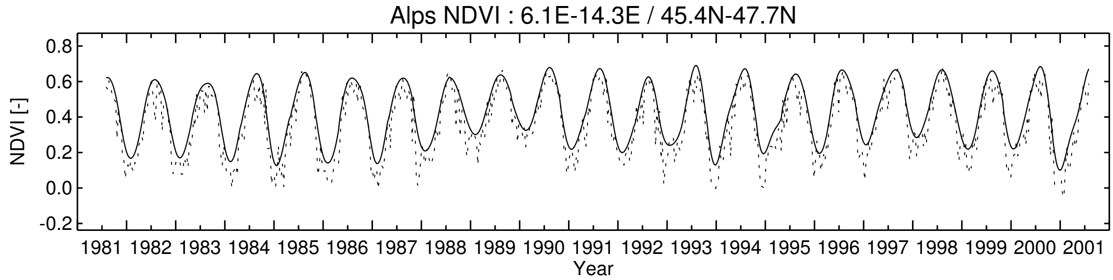

(b) Swiss Alps

Fig. 2.2: 20-year $NDVI$ time-series for one single grid point. The dashed line shows the original Pathfinder $NDVI$ where the solid line represents the corrected EFAI-$NDVI$ phenology time-series

- During the winter, snow under or temporarily on the canopy may impose a negative bias on the $NDVI$ signal, since snow has a high VIS reflectance and a low NIR reflectance.

These assumptions lead to the application of a Fourier adjustment algorithm described in Sellers et al. (1996b) and Los (1998). The 2nd. order Fourier series are able to represent the seasonal variability of vegetation phenology with a smooth analytical function and the original data can be weighted so that higher $NDVI$ values representing uncontaminated measurements receive higher weights than negative outliers (which are attributed to erroneous measurements). This technique was successfully applied to produce the FASIR-$NDVI$ published in the ISLSCP dataset collection (Sellers et al., 1996c) at a monthly temporal and 1° spatial scale. The following sections present the modifications brought to the Sellers et al. (1996b) and Los (1998) approach in order to create the new 0.1° and 10 day EFAI-$NDVI$ dataset.

2.2.c Spatial interpolation

In comparison to the ISLSCP FASIR-$NDVI$ the present dataset is of a much higher spatio-temporal resolution and therefore small area inconsistencies in the dataset are well visible. We have applied a spatial interpolation prior to extracting the yearly phenology curves from the $NDVI$ time-series. No-data values in high latitude biomes during winter are set to a minimum $NDVI$ value as it is a prerequisite for the correct functioning of the temporal interpolation described in Section 2.2.d. To remove the most predominant artifacts all $NDVI$ values above 0.8 are set to missing data. A second order Fourier series, f, is fitted to the yearly Pathfinder $NDVI$ time-series at each grid point. Anomalous $NDVI$ values are detected and flagged as missing if they were outside the boundary $(0.8f - 0.2) < NDVI < (1.2f + 0.2)$ of this idealised phenology curve f. Missing data are spatially interpolated for each 10 day interval according to the following technique, which is an inverse-distance weighted interpolation. For each missing grid point valid neighbors of the same land cover class within a radius r are sampled. The missing value is then replaced by an inverse distance weighted mean of these valid neighbours:

$$W_i = \frac{1}{\sqrt{x_i^2 + y_i^2}} \tag{2.2}$$

$$NDVI = \frac{\sum W_i N_i}{\sum W_i} \tag{2.3}$$

where W_i is the weight of a valid neighbour N_i, x_i the horizontal distance of neighbour N_i to the missing value, y_i the vertical distance of neighbour N_i to the missing value, and N_i the valid neighbouring $NDVI$, same land cover class as the missing $NDVI$ value. Missing data in high latitudes during winter time do occur in an extended area and cannot be interpolated by the above described method. They are flagged when missing data are found for successively five or more 10 day intervals during winter for an individual grid point. Using a land cover map (DeFries et al., 1998) these prolonged periods of missing data are replaced differently for deciduous and for evergreen vegetation. During winter deciduous vegetation is assumed to be in a dormant state and the canopy may be masked by snow cover. These grid points are assigned to a $NDVI$ value of -0.05. Boreal conifers found in Sweden, Finland and the former Soviet Union keep their needles during winter. They project out of the snow layer and these areas have a low albedo during winter (Betts and Ball, 1997). All $NDVI$ values for evergreen forests, which are lower than 0.25 are replaced by the mean of the four last valid $NDVI$ values in late autumn (mostly October values). The underlying assumption of this method holds when $NDVI$ for evergreen forests does not drop below the chosen threshold and if by the end of the vegetation period all deciduous plants have shed their leaves (Sellers et al., 1996b).

Spatial error detection and interpolation is applied to all of the 10 day Pathfinder datasets over the European domain ranging from August 1981 until July 2001.

2.2.d Temporal interpolation

The production of $NDVI$-derived biophysical parameters, used in LSMs to drive the yearly evolution of land surface vegetation, requires that for each grid point they are consistent over time and represent the actual area-averaged state of vegetation. According to the three assumptions presented at the beginning of this section the second order Fourier series are used to extract the seasonal varying phenology time-series from the spatially interpolated $NDVI$ dataset. The Fourier adjustment technique performs well, as described in Sellers et al. (1996b) and Los (1998). We evaluate the Fourier adjustment algorithm by first working with theoretical time-series of simulated yearly $NDVI$ curves including artificial data gaps. In Figure 2.3 we compare the use of 10 day intervals (36 yearly data values) to monthly time-steps. The use of 10 day intervals enhances the ability of the Fourier adjustment to reproduce the simulated phenological curve, even when 2 months of data are flagged as missing. In Figure 2.3(b) the reconstructed curve has a better fit to the original curve with R^2=0.994 for 10 day intervals than for a monthly dataset (Figure 2.3(a), R^2=0.922). Especially during the start and the end of the active growing period the temporal resolution seems to be an important factor.

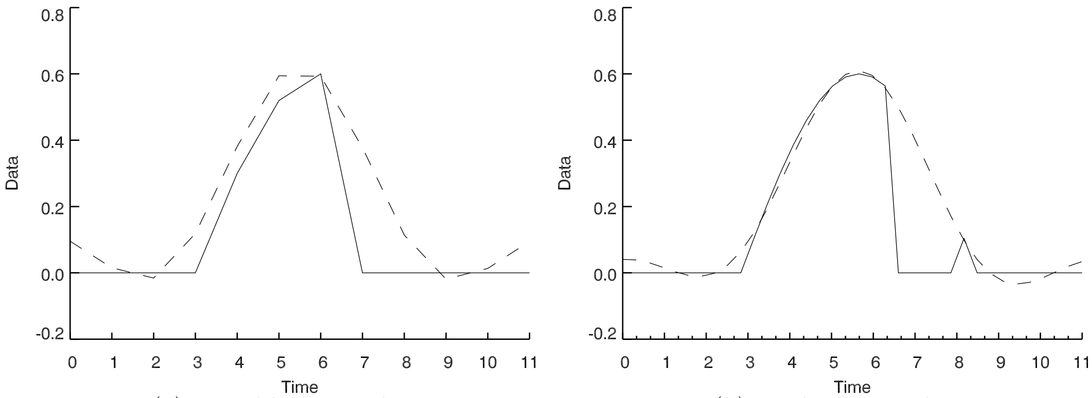

(a) monthly interval (b) 10 day interval

FIG. 2.3: Theoretical phenology time-series: a) 12 and b) 36 data values per year. The solid line represents the modeled $NDVI$ time-series with a 2 month long gap period where a discrete Fourier time-series (dashed) was fitted

Nevertheless, the original Fourier adjustment algorithm as first described by Sellers et al. (1996b) has several shortcomings when used with the 0.1° / 10 day Pathfinder $NDVI$. Biomes with a short growing season have a steep increase in photosynthetic activity in late spring due to leaf unfolding and snowmelt and are subject to a rapid decrease in $NDVI$ when they shed their leaves in autumn. Only a short period of greenness is observed for those biomes (high latitude deciduous forest and biomes in mountainous regions). Second order Fourier series are able to represent features of a half-year periodicity and cannot account for such fast processes. As a result, the state of vegetation can be overestimated by the Fourier adjustment at the beginning and at the end of the growing season and in some cases a second peak is simulated in late winter. The Fourier adjustment algorithm is developed for spatially and temporally subsampled data at the 1° x 1° level and works well with that configuration. The present dataset is at a much finer resolution and includes local-scale variability and short term features (e.g. leaf-out in spring) due to the used 10 day interval.

The ideas developed by Sellers et al. (1996b) and Los (1998) are revised for our purposes and only modifications to these algorithms presented here. For each grid point yearly $NDVI$ time-series are processed in the following way:

1. Each yearly time-series is tested for a summertime growing season. The temporal derivative of a fitted second order Fourier series is examined for each year at each pixel. A growing season is detected if the derivative of this modeled curve f exceeds the bounds $-0.03 < f' < 0.03$ (corresponding to an $NDVI$ increase/decrease of 0.03 per 10 days). The actual start/end dates of the growing season is then shifted

one 10 day period to the beginning/end of the year to be on the safe side. Only deciduous vegetation classes are tested for a growing season.

2. For vegetation with a continuous transition between the growing/non-growing period (e.g. evergreen biomes) we apply the weighted Fourier adjustment procedure proposed by Los (1998) with a slightly modified weighting function. This new weighting function is shown in Figure 2.4 and does prevent excessive weights for large positive anomalies in the time-series:

$$W = \begin{cases} \left(\frac{d-t}{-t}\right)^4 & t < d < 0 \\ \\ 4\sqrt{d} + 1 & d \geq 0 \end{cases} \tag{2.4}$$

   where $t = -0.1$, $d = NDVI - f$, $NDVI$ are the spatially corrected $NDVI$ values, f is 2nd order discrete Fourier series of $NDVI$ and W are the weights.

3. For vegetation with a dormant and an active state in the vegetation phenology the above weighted Fourier adjustment procedure is only applied to the growing season. The weighting scheme is modified as follows for the dormant period:

$$W = 1.0 \tag{2.5}$$

   The non-weighted Fourier series f is used during the dormant period and the weighted series during the growing season, thus both the weighted and the unweighted Fourier series are merged at the two phenological transition dates. This way the curve still inherits the seasonal periodicity of the growth cycle.

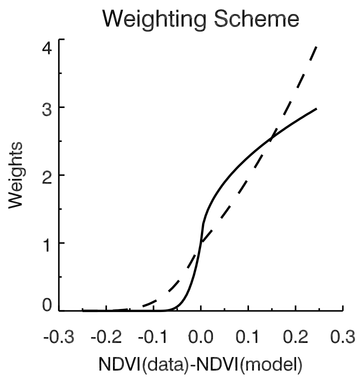

Fig. 2.4: Weighting scheme used for the weighted Fourier adjustment procedure: (dashed) weighting scheme by Sellers et al. (1996b) and (solid) weighting scheme applied in this study

The Pathfinder $NDVI$ dataset is processed by applying the steps 1-3 to the whole European domain, using data from August 1981 until July 2001. A yearly time-series over the Swiss Alps in Figure 2.1(a) (thick solid line) shows that the beginning and the end of the growing season are identified precisely due to the high temporal resolution and the modified weighting scheme. In Figure 2.1(b) an anomaly found at the end of the growing season in the original Pathfinder $NDVI$ is eliminated by the spatial interpolation. There is an advantage in using separate corrections for the growing and the non-growing season, which can be seen in Figure 2.1(c): second order Fourier series do not represent well growing-seasons shorter than half a year (dashed line) and merging the separate corrections at the phenological transition dates (thick solid line) catches the onset and the offset of the growing season. In Figure 2.1(d) a yearly time-series of an evergreen vegetation type mostly found in the northern European boreal zone is displayed and Figure 2.1(e) shows evergreen vegetation in the northwestern coast of France. A different seasonal behaviour with signs of dryness-related vegetation stresses is seen in Figure 2.1(f) for southern European vegetation. However, not all time-series have been processed correctly: in Figure 2.1(g) an unrealistic seasonal behaviour was created for a point in Ireland. Nevertheless the long and early growing season is a well known feature in Ireland, due to the influence of the NAD (north atlantic drift), and is represented well. In Figure 2.1(h) an example is displayed where the growing season was not determined correctly.

The resulting dataset has been named EFAI-$NDVI$ (European Fourier-Adjusted and Interpolated $NDVI$). It is a highly corrected dataset of European vegetation phenology covering the last two decades.

2.2.e Deriving biophysical Parameters from the EFAI-$NDVI$

Remotely sensed parameters like the EFAI-$NDVI$ are not directly applicable in LSMs. The parameters needed by modern LSMs usually consist of a number of vegetation type-dependent static look-up values (like root depth or canopy height) and time-dependent parameters which describe the phenological evolution of the plants. Static parameter look up tables by vegetation type can be found in the literature (Dickinson, 1984; Sellers et al., 1996d,b) and will have a spatial distribution when combined with vegetation type maps (Loveland et al., 2000; Hansen et al., 2000). The most commonly used time-varying parameters include LAI (Leaf Area Index), canopy greenness and z_0 (roughness length). More sophisticated models like SiB 2 make use of the $FPAR$ (Fraction of Photosynthetically Active Radiation absorbed by the green leaves of the canopy) parameter to scale leaf photosynthesis to the ecosystem level.

We derive a number of biophysical land surface parameters from the previously generated EFAI-$NDVI$ dataset. They include $FPAR$, LAI, z_0 and canopy greenness and are derived following the publication by Los (1998) by simple empirical relationships which have been verified and updated in various field observations (FIFE, OTTER, BOREAS and HAPEX-Sahel, see references in Los (1998) and Los et al. (2000)). The theoretical background to the derivation of these biophysical land surface parameters can be reviewed in Sellers et al. (1996b) and Los (1998) and the most basic relationships are presented in the appendix. Examples of these land surface parameters are shown in Figure 2.5 and Figure 2.6.

In Figure 2.5 a justification for the high temporal resolution of this dataset is found: The three maps show the LAI in the Alps region for the compositing periods of May 1-10

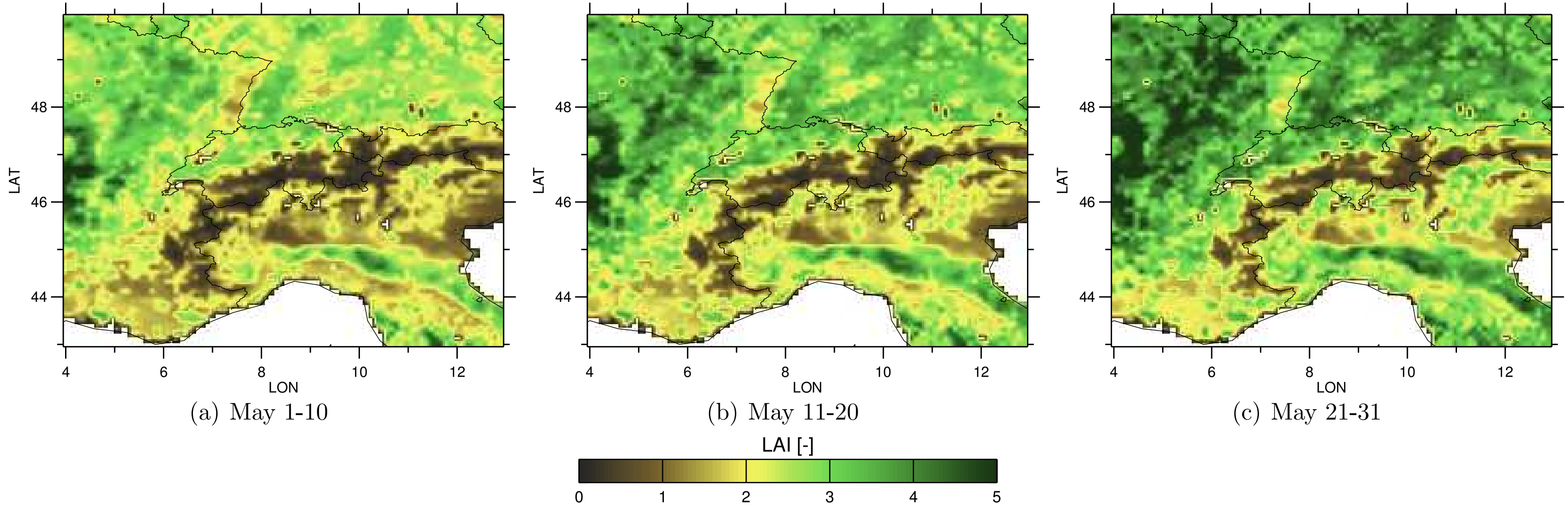

FIG. 2.5: Time-series of leaf area index showing the need for high temporal coverage: Alpine spring greening for 1982-2001 composites

(a), 11-20 (b) and 21-31 (c). During this month the a large increase in LAI is observed in southern Germany, eastern Austria but also in the alpine valleys of Switzerland. The use of monthly composites would mask many of these short term phenology changes. In Figure 2.6 the land surface parameters are illustrated for the time period of July 10-21. $FPAR$ has a very homogeneous pattern and shows high values over most of central, eastern and northern Europe during summer, where LAI exhibits a more spatially varying pattern, especially between tall forest vegetation and short groundcover in Scandinavia. A very dense vegetation with high LAI values is seen in most of eastern Europe. Roughness length has an exponential scaling with LAI and heavily depends on the canopy height. It clearly shows the distribution of short vegetation (low z_0 ranging from 5cm to 20 cm) and tall tree biomes (high z_0 between 1m and 3m).

2.3 Spatial and temporal variability of European vegetation related to climate

Spatial and temporal variability found in the land surface parameters is discussed in this section. We will mostly use the EFAI-$NDVI$ as the primary parameter and not the derived land surface parameters. The derived land surface parameters inherit the same seasonal and interannual variability, since they are first-order dependent on the EFAI-$NDVI$ and only second order on land cover (see Section 2.2). Statistics in this section are either calculated for the full Europe domain or for sub-domains. In Figure 2.7 the geographical extents of the chosen sub-domains are illustrated. This sub-domain system does not reflect any bio-geographical stratification found in literature but is a first step to isolate and analyse the data by regional domains, also in view of the intended future applications of this dataset. It includes a longitudinal gradient from maritime (UK&Ireland) to continental (Western Russia) and a latitudinal gradient from the Alps to Northern Europe. The Mediterranean (e.g. Spain) is not included since the analysis procedure in this section requires a large seasonal amplitude in the phenology. The Alps are analysed separately since this area is of special interest for our research in regional climate.

2.3.a Seasonal variability

Land surface vegetation is often classified into ecosystem types, the so called biomes. Each such biome represents a community of plants in a certain climatic zone and can also be characterized by its specific phenological evolution throughout the year. Phenological events within a biome may include flowering, leafing, dryness-periods, harvesting (for agriculture biomes) and leaf-fall. The timing of these events is dependent on internal plant physiological factors and external influences like plant diseases and local climate. In Figure 2.8 on the left side phenological curves derived from the EFAI-$NDVI$ and averaged by land cover class (SiB land cover classification, derived from the DeFries et al. (1998) land cover classification, see Table A.1) are shown. The distribution of $NDVI$ values are displayed for each land cover class on the right side.

Deciduous forest types (a,b and d) can clearly be distinguished from evergreen forest

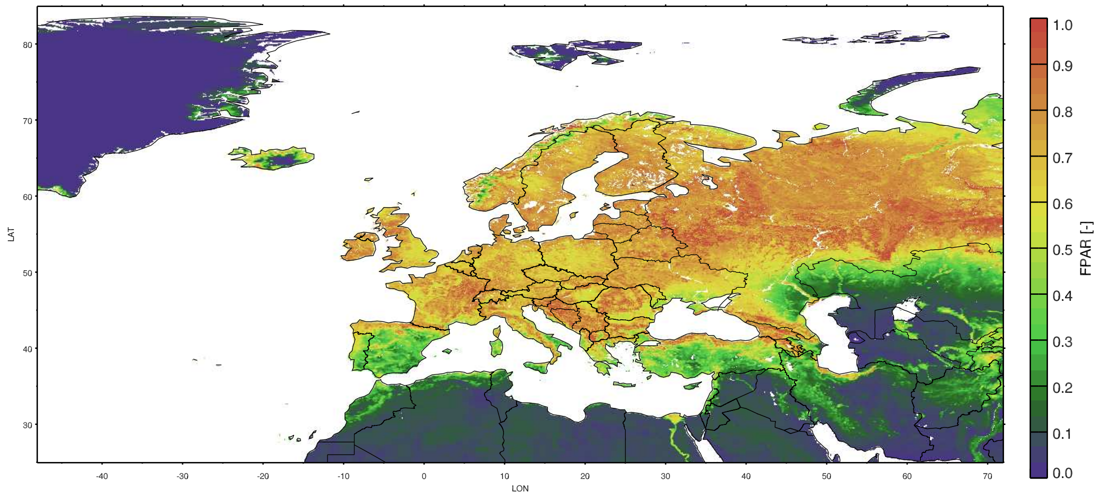

(a) $FPAR$

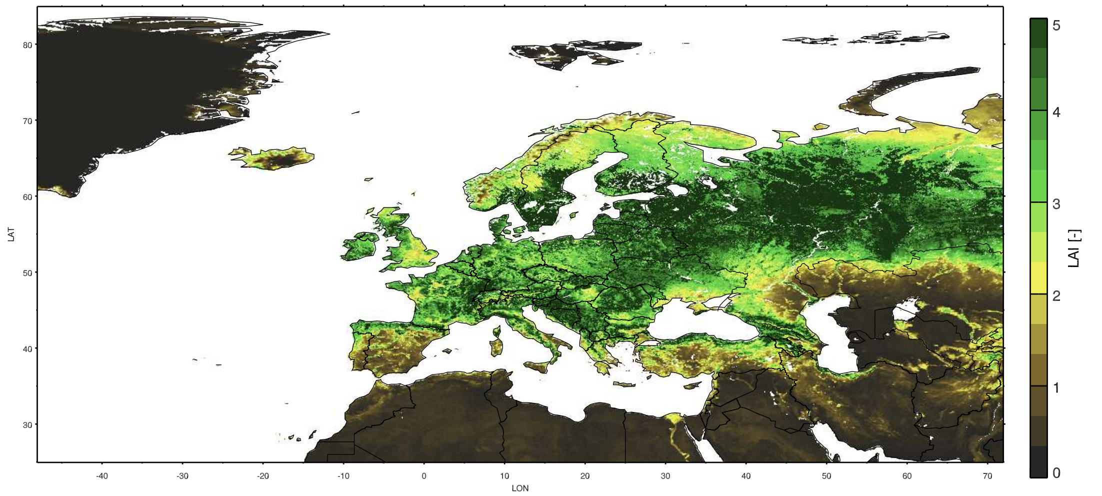

(b) LAI

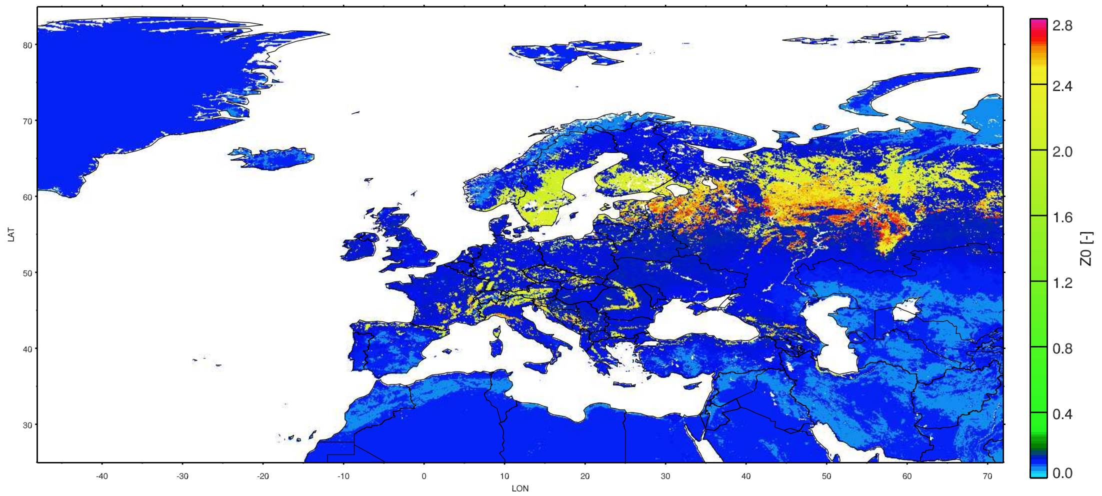

(c) z_0

FIG. 2.6: Maps of the derived land surface parameters covering the period from July 10 to 21 (average yearly climatology derived from the years 1982-2001)

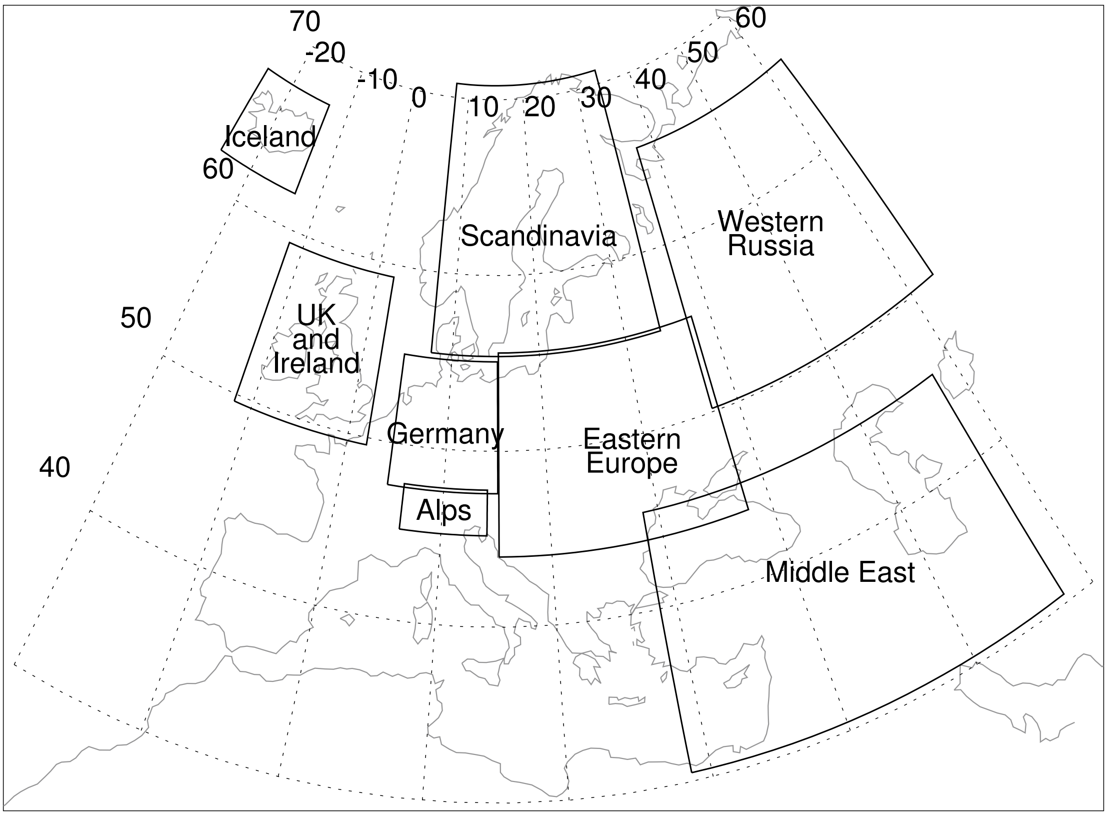

FIG. 2.7: The sub-domain extents which were used to derive anomalies and trends in the EFAI-$NDVI$ dataset

(c) which is mostly found in the boreal zone and in alpine areas. Tall tree biomes account for totally 10.1% of the examined land surface. The evergreen pine trees keep their needles in winter and the seasonal variation is due to the deciduous plants found in those forests. Mixed and deciduous forests (b) found in intermediate and high latitudes have a large seasonal variability, with low $NDVI$ values in winter and high values in summer - also visible in the $NDVI$ distribution diagrams (right column of Figure 2.8). The shrub and bare soil biome (e) - covering 13.8% of the area - is found in the Mediterranean and is subject to a dry climate which does not allow the growth of tall trees. This fact is well reflected in the phenological curve of this biome, where even a reduced greenness in summer due to possible drought conditions is visible. Tundra vegetation (f) is only present in 0.1% of the examined land surface area but the usually short vegetation period and low temperatures for this biome are reflected in the phenology curve, which does not reach high values even in July/August. The soil/desert landcover class (g) is not subject to much vegetation activity, as expected. A rapid and early increase in $NDVI$ is seen in the agriculture biome (h) with a gradual decrease after June. Agricultural land is in fact the biome with the largest area coverage found in Europe (24.9%)

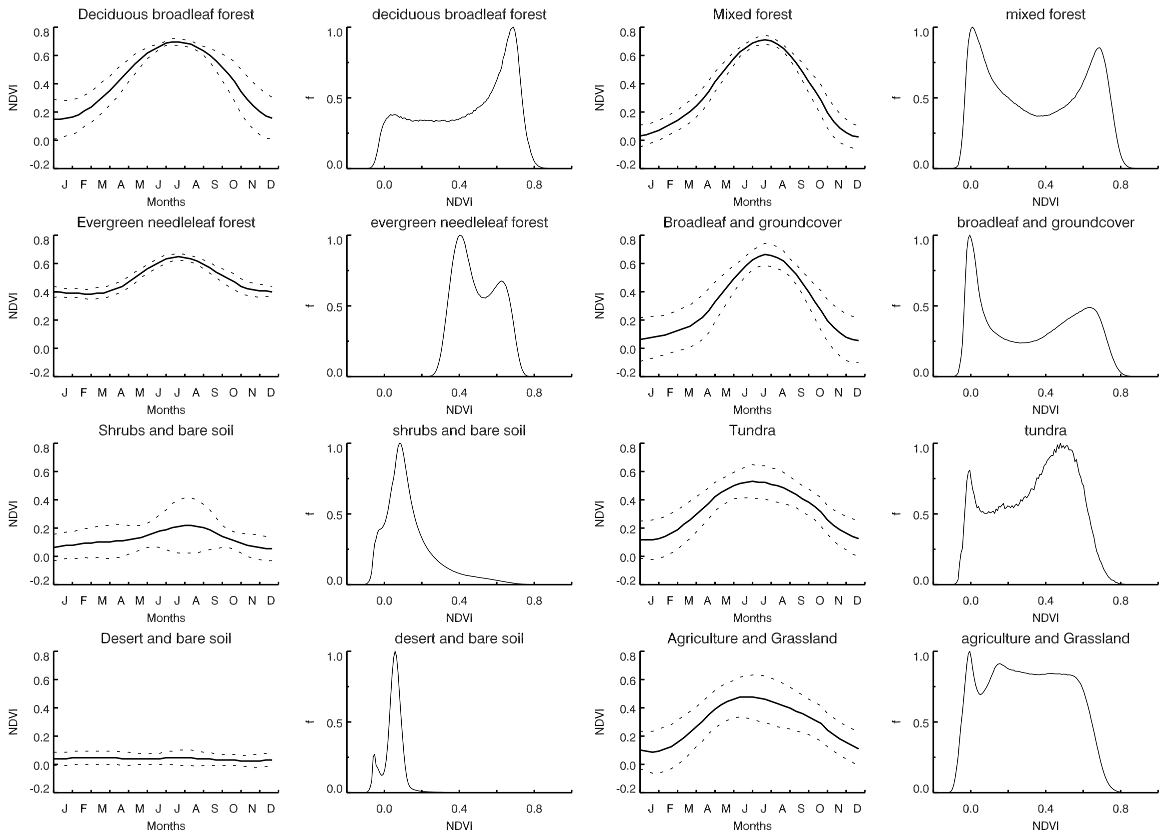

FIG. 2.8: Yearly phenology time-series averaged by land cover class and distributions of $NDVI$ values for these curves. The time-series (solid lines) are plotted with their standard deviation (dashed lines) for each land cover class

2.3.b Interannual variability

Remotely sensed data used in this study may not be able to fully describe the vegetation physiology of individual plants, because the data only reflects radiative properties of the canopy at a very coarse scale, but it is a good application to integrally measure the state of vegetation phenology at the ecosystem level. Used in this context, remotely sensed plant phenology is a very suitable proxy indicator of local and regional year-to-year climate variations. Yearly area averaged time-series of EFAI-$NDVI$ over the Alps are plotted in Figure 2.9.

This plot combines a representation of both the seasonal variability on the horizonal axis and of the interannual variability on the vertical axis (large temporal differences of up to a month in the onset and offset of the greening phase). To examine the interannual response of the satellite measured vegetation phenology to climate variability, yearly anomalies are calculated for three phenological metrics: spring date, growth period length and autumn date. These metrics (black dashed lines in Figure 2.9) do not necessarily relate to point measurements of flowering and leaf-fall, but they provide a statistical means to exploit the interannual signal within the presented land surface parameter dataset.

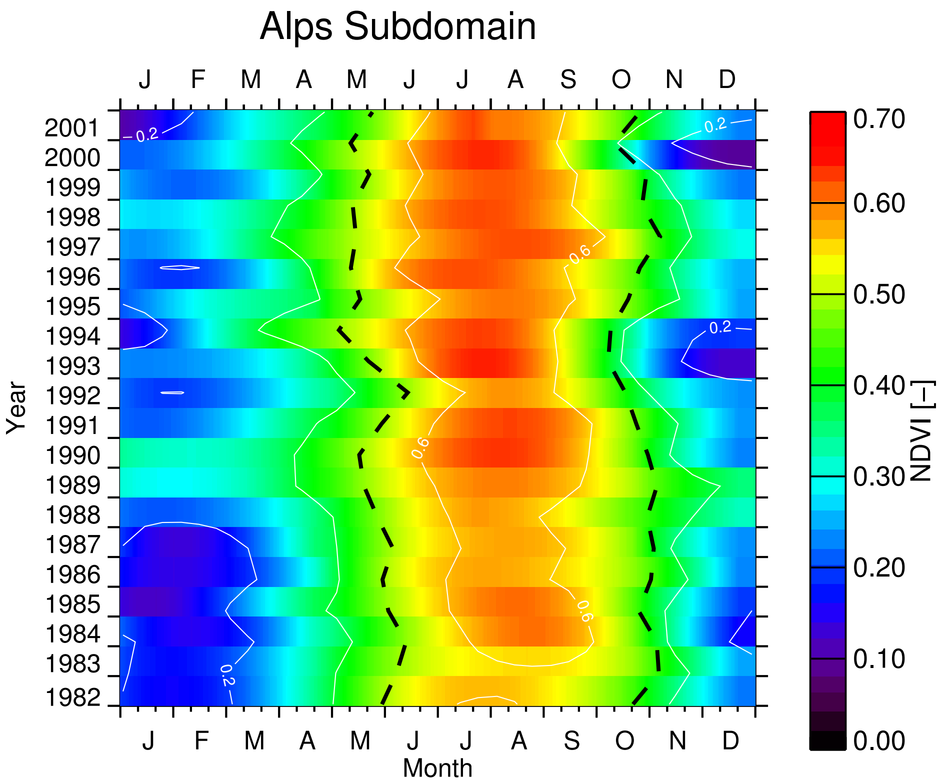

FIG. 2.9: Interannual and seasonal variability as observed in the 20 year period from 1982-2001 for the Alps sub-domain. The area-averaged start and end of the growing season is plotted as a black dashed line

For each grid point within the chosen sub-domains the phenological spring and autumn dates are determined by selecting the 10 day interval, where a certain threshold (here set to $0.4(NDVI_{max} - NDVI_{min}) + NDVI_{min}$) is crossed. In Figure 2.9 the mean start and the end of the growing season over the 20 years for the Alps sub-domain is drawn as a dashed black line.

Using the spring and autumn date the vegetation growth period length is determined by subtracting the spring date from the autumn date. For each sub-domain, all successfully determined phenological metrics are averaged to form a regional scale time-series of spring dates, autumn dates and growth period lengths for the years 1982-2001.

In Figure 2.10 the seasonal mean CRU temperature and precipitation anomalies and the North Atlantic Oscillation (NAO) indices are plotted together with the phenological spring date anomalies for the individual years. For each sub-domain the spring dates are compared to winter (JFMA) temperature/precipitation anomalies and to the winter NAO indices (DJFM). The NAO is a very relevant climatic index for Europe. Strong positive phases of the NAO tend to be associated with above-normal temperatures across Northern Europe and below-normal temperatures in Greenland and often across southern Europe and the Middle East. They are also associated with above-normal precipitation over northern Europe and Scandinavia and below-normal precipitation over southern

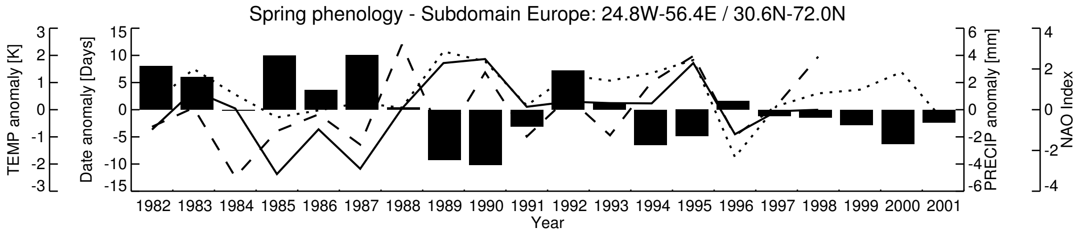

(a) Europe (full domain)

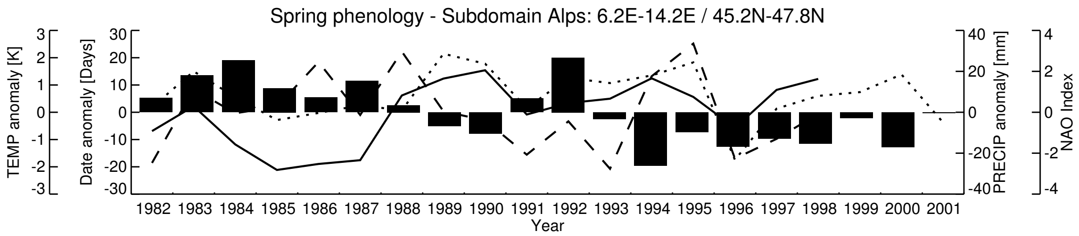

(b) Alps

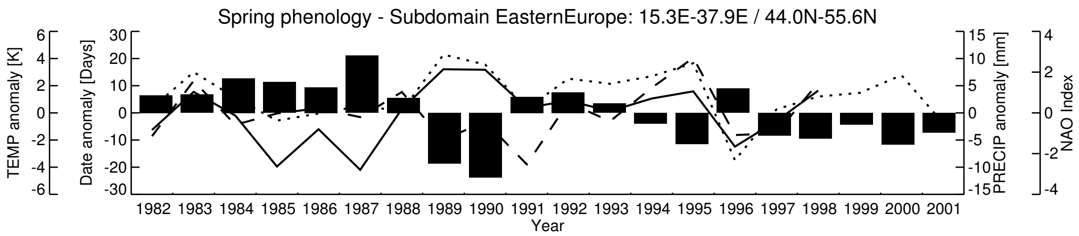

(c) Eastern Europe

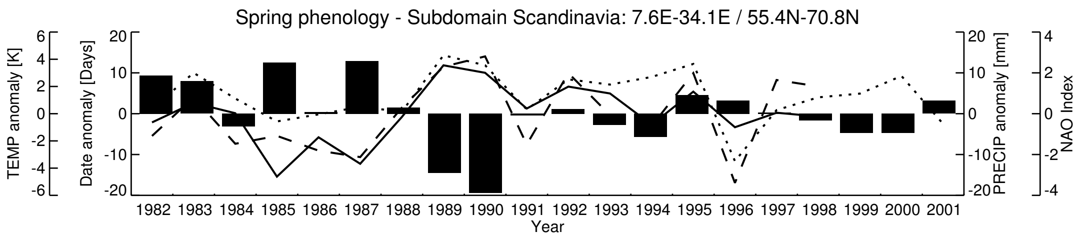

(d) Scandinavia

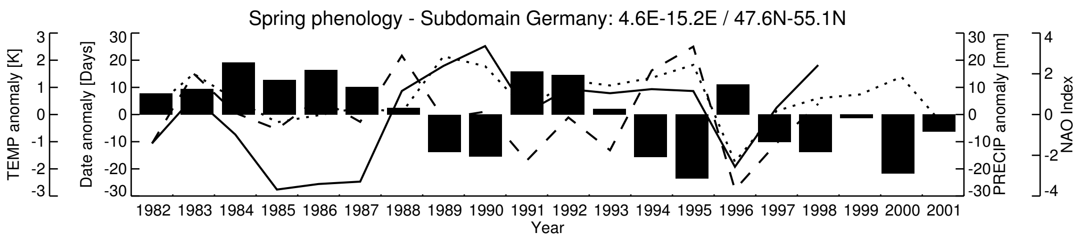

(e) Germany

FIG. 2.10: Yearly anomalies of spring dates (bars, negative values mean earlier springs) plotted with area averaged climate variables: CRU temperature (solid line, JFMA average) and CRU precipitation (dashed line, JFMA average) and the NAO index (dotted line, DJFM average)

and central Europe. Opposite patterns of temperature and precipitation anomalies are typically observed during strong negative phases of the NAO. The wintertime NAO, in particular, exhibits significant interannual and decadal variability (Hurrell, 1995).

The full European domain (Figure 2.10(a)) was subject to early springs in the years 1989 and 1990 as well as the years 1994 and 1995 and 2000. A positive winter NAO phase and warmer spring temperatures in 1989/1990 and in 1994/1995 are a possible indication of the continental scale climate influence on the observed greening pattern. The early 1980s were generally late years in phenological terms. Lower winter temperatures as well as a negative NAO index (normally leading to colder winters and springs and also to extended snow cover) can have caused delayed spring greenings of land surface vegetation during the period 1982-1987. In Figure 2.11 phenological anomalies are correlated with climatic anomalies. The top row of Figure 2.11 displays anomalies in spring phenology correlated to temperature, precipitation and NAO index anomalies. For Europe winter temperatures are negatively correlated with the timing of plant-growth in spring (Figure 2.11(a)). No significant correlation with precipitation is found (Figure 2.11(b)) but the winter NAO - a proxy for the general weather pattern over continental Europe - is weakly linked to spring phenological timing (Figure 2.11(c)). In elevated terrain and at high latitudes plant growth in spring is known to be temperature limited and - because of the high soil moisture availability - not much dependent on precipitation. Spring events such as needle flush and leaf unfolding are found in biometeorology to be very sensitive to spring and winter temperatures (Farquhar et al., 1980; Post and Stenseth, 1999; Menzel, 2000; Defila and Clot, 2001).

The Alps (Figure 2.10(b)) do not show anomalously early springs in the years 1989/1990 and 1995. Over this sub-domain we generally find late springs in the 1980s and early springs in the 1990s. Apart from effects on plant growth related to topography, the southern and eastern ridge of the Alps are known to be strongly influenced by mediterranean climate, which can lead to a significant difference in the plant phenology to the one observed in the northern ridge (Defila and Clot, 2001) and may also explain some of the difference between the Alps and the rest of Europe. In the second row of Figure 2.11 we correlate spring temperature anomalies with spring phenology for different sub-domains. The correlation of spring anomalies with the observed winter/spring temperatures for the Alps sub-domain (Figure 2.11(d)) is rather weak compared to e.g. eastern Europe(Figure 2.11(e)) and Scandinavia (Figure 2.11(f)).

Spring anomalies for eastern Europe are plotted in Figure 2.10(c) and show very large interannual variability. No strong decadal pattern (1980/1990s) like in the Alps is observed but rather the years 1989/1990, 1994/1995 and the most recent years 1997-2001 are exhibiting very early springs of up to 25 days earlier than the mean spring date. The negative correlation of eastern European spring phenology with temperature anomalies is also high, with a value of 0.789 (Figure 2.11(e)).

Phenology in the Scandinavian sub-domain (Figure 2.10(d)) has a temporal pattern similar to the full European domain. The growing season had an exceptionally early start in the years 1989/1990 and did not show reasonable difference from the mean in the years 1994-1998. Generally the decadal pattern of late springs in the 80s is also visible in

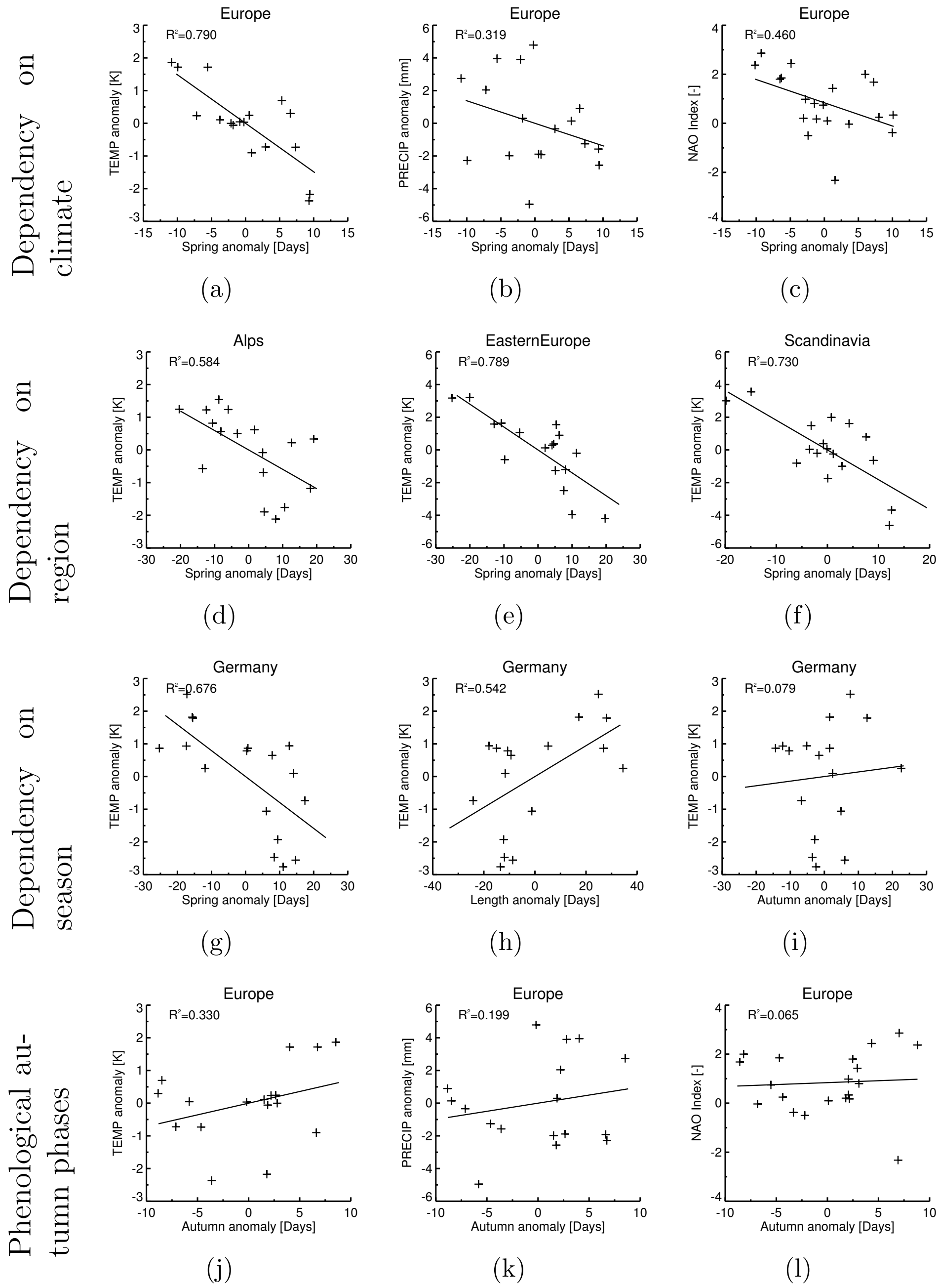

FIG. 2.11: Phenological metrics (spring date, autumn date and vegetation period length) are correlated to temperature, precipitation and the NAO index in different sub-domains

Scandinavia, but the same pattern is much more pronounced in western central Europe (Figure 2.10(e)). Early leaf-out in Scandinavia is strongly linked with positive temperature deviations in winter/spring over that area (Figure 2.11(f)).

Interannual variability of plant phenology is also observed on the ground in a sophisticated and long-term network of phenological gardens (IPG, international phenological gardens) around the globe. Menzel (2000) has collected and analysed observational data from the IPGs in Europe for the years 1959 - 1996. In this dataset the same years as observed in the EFAI-$NDVI$ show an early spring with more than a week difference compared to the 1976-1980 spring dates. The growing season was observed to be anomalously long throughout the period from 1989 until 1995, which was partly reproduced in this study. In our dataset the years 1989/1990 and 1994/1995 have early springs but years 1991-1993 show a rather nominal to late spring. It is well known in phenology research that the leaf-out in spring is easier to measure than the autumn date. In our dataset, autumn dates are likely to be affected by persistent cloud cover and data dropouts in winter. The third row of Figure 2.11 correlates phenological metrics in different seasons to temperature anomalies. The autumn phases do not correlate well with spring temperatures (Figure 2.11(i)). Also, summer temperature (11j), precipitation (11k) or NAO data (11l) anomalies are only correlating weakly with R^2=0.330, 0.199 and 0.065. These simple relationships cannot account for the complex soil-vegetation-atmosphere interactions during the summer months, especially for the long term soil-moisture memory related effects. For most sub-domains the growth period length has a positive (but weak) correlation with spring temperatures.

Since 1951, phenological data from wild grown plant species have been systematically collected in Switzerland. A number of plant species at different biogeographical locations are observed and phenological phases are recorded by lay observers and data is processed at MeteoSwiss. Defila and Clot (2001) have analysed the averaged time-series for spring and autumn events for Switzerland covering the years 1951-1995. Interannual variations of these observations show a good agreement with our phenology data. The overall picture of Switzerland indicates an exceptionally early spring in 1990 and 1994 (up to 20 days) and late growing seasons for the period 1985 to 1987. The metrics for the Alps and Germany (Figure 2.10(b and e)) show a similar temporal pattern, although the years 1989&1990 are somewhat less pronounced (4-7 days earlier spring) than in 1994 (20 days earlier).

2.3.c Multi-year Trends

Error sources in the remotely sensed $NDVI$ products may be a serious limitation to the detection of anthropogenic trends in land surface vegetation. The non-adequate calibration of the used Pathfinder $NDVI$ dataset described in Section 2.2 can lead to errors of the same order of magnitude as the observed trends in $NDVI$. Also, existing satellite measurements cover a relatively short time period. It is important to keep these limitations in mind while working with trend analysis of $NDVI$ time-series. Satellite remote sensing is nevertheless the only feasible means that we have to observe the long term biospheric activity with a large area coverage.

In our dataset we assume that trends are due to changes in canopy reflectance properties, thus only occuring in vegetated areas. Trends detected in deserted areas can be attributed to systematic instrumental drifts. The mean EFAI-$NDVI$ trend in a deserted region (Sahara 0.2°E-2.6°E / 29.3°N-31.1°N) is 0.21%/year. Mean $NDVI$ trends for vegetated areas are significantly higher and range from 0.9 to 1.5%/year, which supports the reliability of trends in vegetated areas.

We apply linear regression analysis to our $NDVI$ time-series and check for trends in spring date, growth period length, autumn date, minimum $NDVI$, maximum $NDVI$ and mean $NDVI$. Maps of Europe with spring and autumn date trends are shown in Figure 2.12. The results reveal evidence for long term changes in the European plant phenology. Central Europe seems to exhibit a general earlier appearance of plants in spring during the last 20 years, where northern Europe shows the opposite trend.

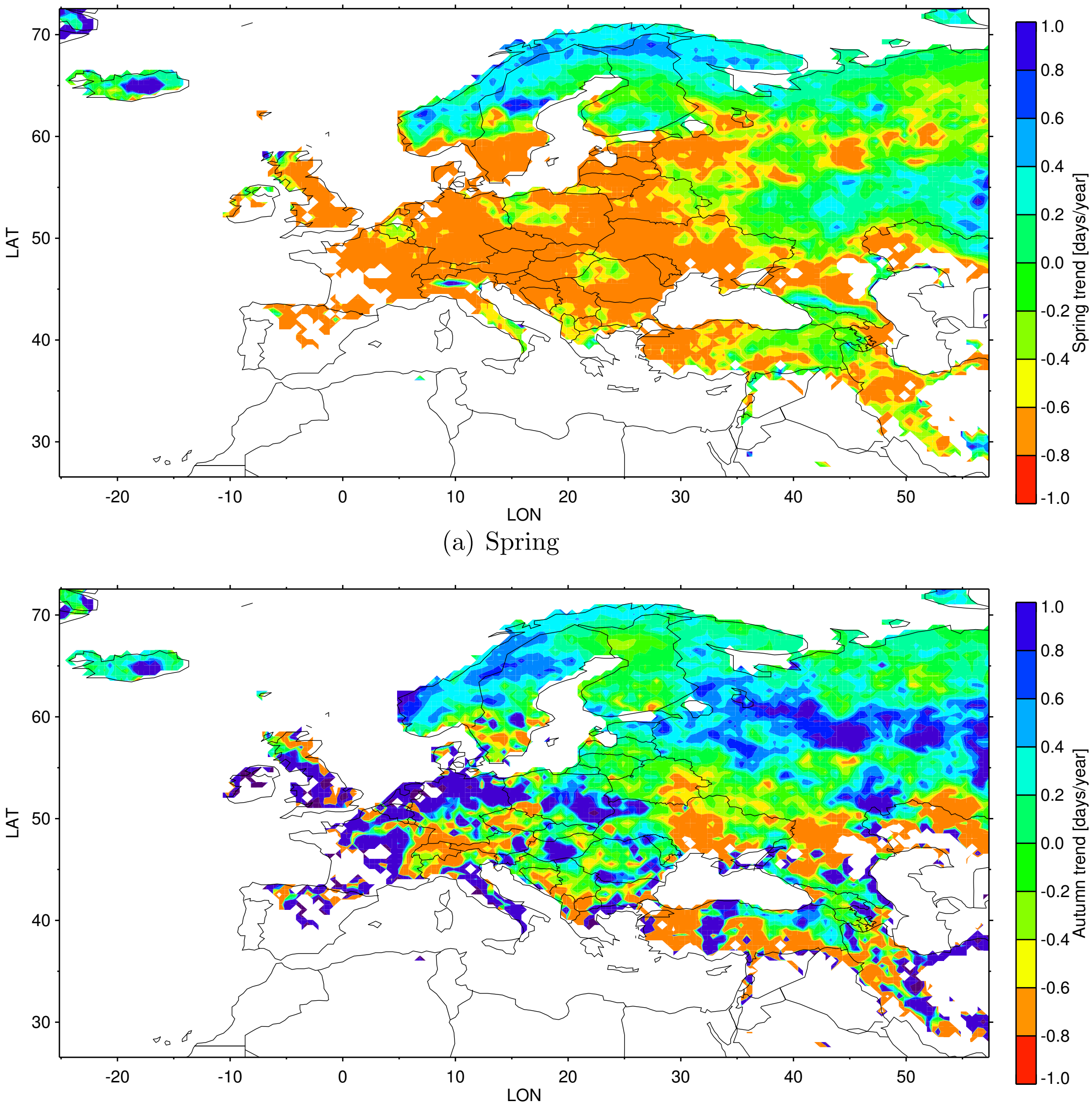

(a) Spring

(b) Autumn

FIG. 2.12: Multi-year trend maps

An average of the trends is calculated for the individual sub-domains in Europe. The trends of the phenological metrics are only calculated for grid points where a growth period was observed and phenological dates can actually be determined. In Table 2.1 spring, autumn and growing season length trends given and classified according to their F-test confidence values. The trend for the mean $NDVI$ values found in each region is indicated in the last column. Almost all trends are negative for spring dates and positive for autumn dates, thus a lengthening of the growing season is observed on a large area over the European continent. Certain areas like southern Germany and the Alps in particular are experiencing autumn phases occuring earlier (Figure 2.12(b)).

TABLE 2.1: Trends in European Phenology derived from the EFAI-$NDVI$ dataset

Region	Spring [days year^{-1}]	Autumn [days year^{-1}]	Length [days year^{-1}]	$NDVI$ [% year^{-1}]
Germany	-1.41[3]	-0.04[1]	1.38[2]	0.85
Alps	-1.53	-0.69[1]	0.84[1]	0.74
Scandinavia	-0.48[1]	0.44[1]	0.92[1]	0.82
Eastern Europe	-1.32[2]	0.30[1]	1.63[1]	1.12
Western Russia	-0.47[1]	0.61[1]	1.08[1]	0.79
UK & Ireland	-1.88[3]	0.51[1]	2.38[1]	0.84
Iceland	-0.44[1]	0.37[1]	0.81[1]	1.26
Middle East	-0.48[1]	0.49[1]	0.97[1]	0.72
Europe (full domain)	-0.54[1]	0.42[1]	0.96[2]	0.78

[1] significant at the 1% level
[2] significant at the 5% level
[3] significant at the 10% level

Previous $NDVI$ trend analysis like the one conducted by Myneni et al. (1997) only cover the period from 1981-1991. We have analysed trends within this period and have found that they are remarkably higher with a mean $NDVI$ trend of 2.26%/year during the 1980s and lower with 0.16%/year in the 1990s, resulting in a mean $NDVI$ trend of 0.78%/year for the whole period. Spring dates in this study show the same decadal variations, with a highly negative trend during the 1980s and almost no trends in the 1990s. The separate analysis of trends for the two decades suggests that the time-series is a product of long term regionally and globally changing vegetation phenology and periodic fluctuations. Both seem to be of the same order of magnitude.

2.4 Discussion and Conclusion

In this study we compare satellite derived phenology with ground observed phenological data and correlate interannual variations of spring phenology to winter/spring temperature precipitation and NAO index anomalies. The original satellite sensor data used for this study are known to be subject to a number of potential problems. We have presented a means to effectively derive a consistent time-series of vegetation phenology by post-processing the Pathfinder $NDVI$ with weighted second order Fourier series.

One common problem reported in the literature is the question of whether the sudden increase of $NDVI$ in spring at high latitudes coincides with snowmelt or is really the emergence of leaves (Reed et al., 1994). If the two events occur at significantly different times, then the beginning of the growing season derived from $NDVI$ may just catch snowmelt - what is definitely not desired. In land surface models this error will not necessarily transfer to excessive plant activity due to temperature limitations and the explicit simulation of snow cover, but this problem may affect greening season length estimates.

Another weakness of satellite radiometry in visible wavelengths are the extended data dropouts in high latitudes during winter. The correction method used here is able to recover a continuous dropout of around 2 months and assumptions are made to estimate $NDVI$ values for longer data dropouts. Sudden data dropouts in autumn may nevertheless limit the estimation of the growth period length in our phenological analysis. Apart from the uncertainity associated with remote sensing, the length of the growing period and the phenological autumn phases also cannot be simply linked to temperature and precipitation averages.

The onset of greening in spring varies for ±20 days relative to the mean date within this 20 year period. 1985-1987 generally had late springs and years 1989, 1990, 1994 and 1995 had early ones. Large year-to-year fluctuations in the atmospheric CO_2 signal have been observed by Keeling et al. (1996). Earlier starts of CO_2 uptake by northern hemisphere vegetation are observed in Point Barrow for the years 1981, 1990 and 1991 and are nominal for the years 1984-1986; in contrast, the Mauna Loa record shows very early springs in the years 1987 and 1991-1992. Due to long-term soil respiration processes a phase lag of two years between atmospheric CO_2 anomalies and vegetation-climate anomalies is proposed by Keeling et al. (1996), which makes our analysis consistent with their results.

The knowledge of these interactions has led to the assumption that global land use changes, anthropogenic emissions of greenhouse gases (CO_2, Methane) as well as the observed global warming are possibly enhancing large area biospheric activity. We find trends in the 20 year EFAI-$NDVI$ that generally agree with recent findings in plant phenology research. Linear trends of the averaged EFAI-$NDVI$ time-series vary from 0.72% to 1.12% per year depending on the region. These trends indicate an overall enhanced vegetation activity, mostly due to a prolongation of the growing season with earlier occuring springs for the whole Europe (-0.54 days/year). Regional differences are visible. The trends are more pronounced in Germany (-1.41 days/year) than they are in Scandinavia (-0.48 days/year) where we also find evidence for delayed springs. The quantitatively small trends which are extracted from the satellite measured vegetation phenology are, however approximately of the same order of magnitude as the expected errors in the dataset. Moreover, the methodology presented here cannot replace and, in fact, requires a good pre-calibration of satellite data, which is not available in the Pathfinder dataset. We believe that further research, longer $NDVI$ time-series, ground validation and especially an in-depth cross-calibration with new satellite sensors (MODIS instrument on board TERRA and AQUA), and long-term ground measurements of phenological data are needed to gain more confidence.

Developing this methodology was useful in order to prepare for the arrival of MODIS data. The dataset has shown to be useful at this resolution and does agree with known

European climatic zone characteristics in both space and time. Generally, the results increase our confidence in the usefulness of satellite sensor derived land surface parameters for land surface modeling. These parameters inherit seasonal and interannual dynamics seen in land surface vegetation over the last two decades. They are a good estimator for large scale plant photosynthesis and phenology but they cannot account for many of the factors that drive land surface processes (such as soil moisture availability, nutrients availability and vapor pressure deficit). Only the use of these land surface parameters in a land surface model which is coupled to a climate model (e.g. the CHRM regional climate model by Vidale et al. (2003)) will enable to study the full spectrum of the complex soil-vegetation processes and land-atmosphere feedbacks. An upcoming paper will explore the application of this dataset in regional climate modeling.

2.5 Acknowledgements

The funding for this study was provided by the National Centre of Competence in Research on climate variability, predictability, and climate risks (NCCR) funded by the Swiss National Science Foundation (NSF). The authors would like to first express their thanks for the support and suggestions of Prof. Christoph Schär. We would like to thank Sietse O. Los, Jim Collatz and Jim Tucker for discussions and data and would like to acknowledge ETH and Code 912/913 at Goddard Space Flight Center for being able to use their computing resources, which were essential for the successful completion of this project. Special thanks go to Scott Denning, Kevin Schaefer and Ian Baker from CSU for providing access to the mapper code used to process the derived biophysical land surface parameters.

The Land Pathfinder $NDVI$ data used in this study were produced through funding from the Earth Observing System Pathfinder Program of NASAs Mission to Planet Earth in cooperation with National Oceanic and Atmospheric Administration. The data were provided by the Earth Observing System Data and Information System (EOSDIS), Distributed Active Archive Center at Goddard Space Flight Center which archives, manages, and distributes this data set.

We highly encourage the use of the presented biophysical land surface parameters as a climatology (1982-2001) or as a 20 year time-series. This dataset is designed for and capable of enhancing existing LSMs with a boundary condition allowing to represent spatial and temporal dynamics of land surface vegetation. The parameter set is available from the authors upon request.

Chapter 3

Modeling diurnal to seasonal water and heat exchanges at European Fluxnet sites

Modeling diurnal to seasonal water and heat exchanges at European Fluxnet sites *

Reto Stöckli † and Pier Luigi Vidale ‡

ABSTRACT

The importance of linking measurements, modeling and remote sensing of land surface processes has been increasingly recognized in the past years since on the diurnal to seasonal time scale land surface - atmosphere feedbacks can play a substantial role in determining the state of the near-surface climate. The worldwide Fluxnet project provides long term measurements of land surface variables useful for process-based modeling studies over a wide range of climatic environments.

In this study data from six European Fluxnet sites distributed over three latitudinal zones are used to force three generations of LSMs (land surface models): the BUCKET, BATS 1E and SiB 2.5. Processes simulating the exchange of heat and water used in these models range from simple bare soil parameterizations to complex formulations of plant biochemistry and soil physics.

Results show that - dependent on the climatic environment - soil storage and plant biophysical processes can determine the yearly course of the land surface heat and water budgets, which need to be included in the modeling system. The Mediterranean sites require a long term soil water storage capability and a biophysical control of evapotranspiration. In northern Europe the seasonal soil temperature evolution can influence the winter energy partitioning and requires a long term soil heat storage scheme. Plant biochemistry and vegetation phenology can drive evapotranspiration where no atmospheric-related limiting environmental conditions are active.

*accepted for publication in Theoretical and Applied Climatology on 4. August 2004

†Reto Stöckli, Institute for Atmospheric and Climate Science, Winterthurerstrasse 190, 8057 Zürich, Switzerland. e-mail: stockli@env.ethz.ch, phone: +41 1 635 5209

‡Pier Luigi Vidale, Institute for Atmospheric and Climate Science, Winterthurerstrasse 190, 8057 Zürich, Switzerland. e-mail: pier-luigi.vidale@ethz.ch, phone: +41 1 635 5218

3.1 Introduction

The interactions between the land surface and the atmosphere have been studied in a manifold way in climate research during the past decades. As described in Running et al. (1999) integrated approaches using tower flux measurements, satellite remote sensing and numerical modeling can help to understand the dynamics of the biosphere and land surface processes on various spatial and temporal scales. This approach has been used in major campaigns (e.g. FIFE: Sellers et al. (1988), BOREAS: Sellers et al. (1997b), LBA: Avissar et al. (2002)). The exchange processes taking place at the land surface include short term feedbacks like vegetation transpiration controls over the bowen ratio (Chen et al., 2001); or radiation feedbacks through snow cover (Betts and Ball, 1997). On the seasonal time scale vegetation phenology (Bounoua et al., 2000; Buermann et al., 2001) and the soil moisture storage (Schär et al., 1999; Koster and Suarez, 2001) can play a role in the land surface hydrological cycle, especially through control of the boundary layer development and radiation-cloud-precipitation feedbacks. Soil heat storage and soil freezing in cold climates can play an important role in the land surface energy partitioning, as was found by McCaughey et al. (1997) and Viterbo et al. (1999). On the interannual or longer time scale feedbacks include processes like land use changes (Heck et al., 1999; Pielke Sr, 2001b) and nutrient cycling (Dickinson et al., 2002). Many of these processes have been successively included in Land Surface Models (LSMs), which have been used in long term climate simulations and in numerical weather forecasting (Chen et al., 2001).

As reviewed by Henderson-Sellers et al. (2003) the land surface climate predicted from recent AMIP II (Atmospheric Model Intercomparison Project) GCM simulations is still strongly dependent on the used LSM and its parameter set, despite advances in modeling during the last decades. Long-term land surface observations are mostly not available on global scale for GCM-type comparison studies and this uncertainty limits their interpretation. There is also a need to know how biospheric measurements from global observational networks (e.g. satellite phenology) can be linked to processes modeled by LSMs. Integrations of such observational data have the potential to provide guidance to understand what is happening in coupled land surface - atmosphere climate simulations.

Following Sellers et al. (1997a) three generations of LSMs can be differentiated in terms of their complexity: first generation "bucket" models; second generation "biophysical" models; and recent third generation "photosynthesis-conductance" models. While the bucket approach is still used in some climate and numerical weather prediction models (see e.g. in Gedney et al. (2000)), third generation models are already used in integrated ecosystem modeling (Cox et al. (2000) and Eastman et al. (2001)). Many LSMs in these three categories were also compared at the local scale, in off-line mode, by the PILPS (Project for the Intercomparison of Land-Surface Parameterization Schemes, Chen et al. (1997); Pitman and Henderson-Sellers (1998)) project and revealed a large spread among the models in terms of their heat and water fluxes, which helped to improve a number of LSMs. PILPS, however, aimed at comparing a large number of LSMs rather than at the analysis of individual schemes.

In comparison to PILPS, and following the categorization in Sellers et al. (1997a), this study uses three LSMs of increasing complexity (BUCKET by Manabe (1969), BATS 1E

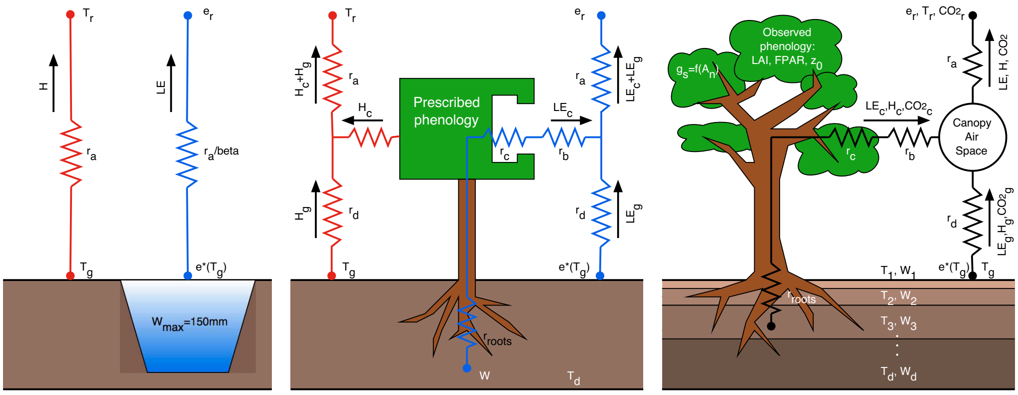

Fig. 3.1: Land Surface Model generations: BUCKET, BATS 1E and SiB 2.5

by Dickinson et al. (1993) and SiB 2.5 (Sellers et al., 1996d; Vidale and Stöckli, 2005)) shown in Figure 3.1 to evaluate the aforementioned research questions at six European Fluxnet sites, distributed over three latitudinal zones (Mediterranean, central Europe, northern Europe). Each latitudinal zone includes one deciduous and one evergreen forest site (Figure 3.2), so that the choice of these sites seeks to explore a substantial spread in climatic forcing and biomes. Fluxnet, a global network of micrometeorological measurement towers (Baldocchi et al., 2001), serves as an excellent driver and validatation data source for such a study since it provides multi-year and continuous data time-series in a standardized format. The analysis methodology of this study involves a comparison of the yearly course of modeled and measured soil temperature and soil moisture since these are prognostic variables in models and can control biophysical processes depending on climatic conditions. The insight into these processes then allows to compare and discuss resulting sensible and latent heat fluxes above the canopy, which are known to be largely LSM dependent.

The next section outlines the modeling methodology. In the results section modeled and observed soil temperature, moisture, heat and water fluxes are compared for the six Fluxnet sites. The discussion focuses on plant biophysical and soil storage processes and on finding important control mechanisms on surface fluxes in each climatic regime.

3.2 Methods

3.2.a Data

Driver and validation data were both obtained from the Fluxnet project. The project uses standardized instrumentation to measure micrometeorological variables, water, heat, momentum and CO_2 fluxes, soil temperatures and moisture. The turbulent fluxes are measured using the eddy-covariance technique (Moncrieff et al., 1997) which can be sensitive to extreme climatic conditions, low wind speeds and heterogeneous terrain (Baldocchi et al., 2001; Schmid et al., 2003). Energy balance closure at Fluxnet sites, calculated from net radiation and eddy covariance sensible and latent heat fluxes, was estimated to be in the order of 20% (Wilson et al., 2002). This uncertainty in the data seems large, but its

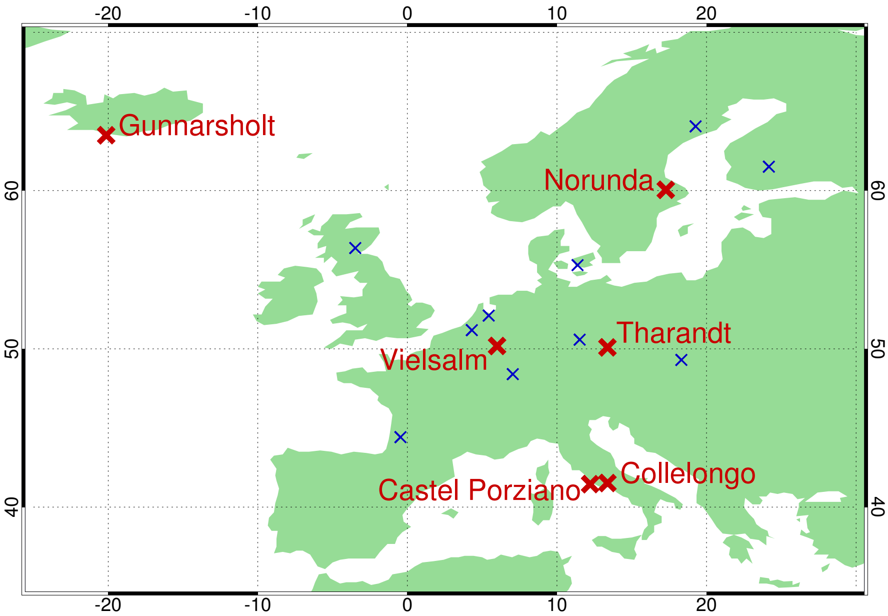

FIG. 3.2: Location of the European Fluxnet sites used in this study

usability in a model comparison study can be justified: Fluxnet is the only continuously available global data for integrative biospheric research and our analysis will primarily focus on the time signature of fluxes and only secondarily on their magnitude.

The following Fluxnet data were used to drive the LSMs: short wave downward radiation (R_g [Wm^{-2}]), long wave downward radiation (LW_d [Wm^{-2}]), wind speed (WS [ms^{-1}]), precipitation (PPT [mm]), surface pressure (P_s [Pa]), temperature (T_m [K]) and dew point temperature (T_d [K], or relative humidity RH [%]). Since data coverage of Fluxnet is around 65-75% (Baldocchi et al., 2001) the following gap-filling methodology was applied:

- short gaps (less than 6 hours) were filled with linear interpolation;
- longer gaps were filled with a 7-day running mean diurnal cycle of the missing variable;
- PPT gaps were not filled, except for the Italian station Collelongo, where precipitation was missing for the months January-July 1997. Precipitation values from a nearby reference station were used there.

LW_d is not distributed through the Fluxnet archive for the chosen measurement sites. It had to be parameterized using the radiation balance formulation:

$$LW_d = R_n - R_g + R_r + \epsilon\sigma T_s^4 \tag{3.1}$$

where R_n is the net radiation [Wm^{-2}], R_r is the reflected radiation [Wm^{-2}], ϵ is the land surface emissivity [-] (set to 1), σ is the stefan bolzman constant [Wm^{-2}K^{-4}] and T_s is the surface radiative temperature [K]. The latter was not available in the Fluxnet dataset but in a dense forest it will be close to the canopy temperature. A rough approximation was used by setting it to the mean of the soil surface and reference temperature, which should hold in the mean of the diurnal cycle, as illustrated in Holtslag and Ek (1996). Using a radiative transfer scheme and a boundary layer parameterization to resolve T_s on the diurnal time scale was not feasible because these approaches are also dependent on LW_d. An uncertainty of $\pm$1K in the used approximation results in an uncertainty in the order of 10Wm^{-2} in the derived radiation.

For cases where not all of the radiation components were available LW_d was derived empirically, by using the clear-sky LW_d formulation developed by Idso (1981). This formulation can however underestimate LW_d during cloudy days:

$$LW_d = \left(0.7 + 59.9 \cdot 10^{-6} q_m \exp \frac{1500}{T_m}\right) \sigma T_m^4 \tag{3.2}$$

where q_m is the water vapour pressure at reference height $[Pa]$. Gap filled surface fluxes corrected by Falge et al. (2001) are used in the results section. The yearly energy balance from observations at the Fluxnet stations is calculated as: $R_n = H + LE - G$ where LE, H and G are the latent, sensible and ground heat fluxes [Wm^{-2}]. The yearly runoff R [mm] in observations is calculated as the residual of the water fluxes: $R = PPT - LE/L_v$ where L_v is the latent heat of vaporization [Jkg^{-1}]. Soil temperature data at 30cm depth and soil moisture data from TDR measurements were also used. The measurement depths of the latter data have been reported as follows: Collelongo 0-88cm, Castel Porziano 40-70cm, Vielsalm 45cm, Tharandt 40-70cm, Gunnarsholt 45cm, Norunda 40-70cm.

3.2.b Models

BUCKET (Manabe, 1969) is a first generation model. It offers no biophysical control on water and heat fluxes except for a so called "bucket" which is able to hold precipitated water. The evaporation from this bucket is limited by the β factor [-] and has a linear dependence on soil moisture W [-] (relative to saturation):

$$\beta = f(W) \tag{3.3}$$

BUCKET requires few parameters (such as surface albedo or bucket size). The model used here is a modification of BATS 1E (Dickinson et al., 1993), including its thermal soil scheme, since the diurnal closure of the energy balance requires a ground heat flux. Any vegetation-related processes are turned off by setting the fractional vegetation cover to 0. The bucket-type evaporation is calculated by multiplying bare soil evaporation from a bucket with 150mm water holding capacity with the β factor.

BATS 1E (Dickinson et al., 1993) is a biophysical model and it includes a bulk canopy layer that controls the water flux from the root zone to the atmosphere by regulating the stomatal conductance g_s [ms^{-1}], limited by environmental factors dependent on temperature T [K], soil moisture W [mm], water vapour pressure deficit (VPD) δe [Pa] and radiation PAR [Wm^{-2}]:

$$g_s = f(PAR, \delta e, T, W) \text{ and } g_c = g_s \cdot LAI \tag{3.4}$$

Canopy-scale fluxes are calculated by a linearly scaling with LAI (Leaf Area Index [m^{2}m^{-2}]. LAI and other parameters depend on vegetation and soil type and are derived from look-up tables. Soil water is stored in a three layer soil (top, root, and deep soil)

TABLE 3.1: Model vegetation and soil boundary conditions

Site	lat [°N]	lon [°W]	ref. height [m]	vegetation type	soil type
Collelongo	41.9	13.6	32	deciduous broadleaf	sandy loam
Castel Porziano	41.7	12.4	18	evergreen needleleaf	loamy sand
Vielsalm	50.3	6.1	40	deciduous broadleaf	loam
Tharandt	50.9	13.6	42	evergreen needleleaf	silt loam
Gunnarsholt	63.8	-20.2	2.5	deciduous shrub	sand
Norunda	60.1	17.5	100	evergreen needleleaf	loamy sand

and soil heat is stored in a simple two-layer force-restore scheme.

SiB 2.5 (Sellers et al., 1996d; Vidale and Stöckli, 2005) is a so-called photosynthesis-conductance model where plant transpiration is directly linked to net assimilation A_n [mol m^{-2} s^{-1}] by the Ball-Berry equation:

$$g_s = f(A_n) \text{ and } g_c = \int_{z_1}^{z_2} f(V_{max0}, PAR) f(pCO_2, \delta e, T, W) \Pi dz \qquad (3.5)$$

Canopy-scale fluxes are calculated by expressing photosynthesis A_n as a canopy-integrated (from the canopy bottom z_1 to the canopy top z_2 [m]) function of radiation, nutrients (V_{max0} [mol m^{-2} s^{-1}]), CO_2 pressure pCO_2 [Pa], δe, W and T. The PAR-use parameter Π [-] describes the extinction of light (and therefore nutrients and photosynthesis rate) through the canopy and is a function of $FPAR$ (Fraction of Photosynthetically Active Radiation available to plants), which controls both the phenological and biochemical activity. This framework requires less empirical parameters since $FPAR$ can be derived from spectral vegetation indices by satellite remote sensing. Water is stored in a three layer soil and a multi-layer thermal soil after Bonan (1996) and a new solution core including a prognostic canopy air space (CAS) as presented in this issue by (Vidale and Stöckli, 2005) is used. The latter process allows for storage of heat, water and CO_2 in the air volume within the canopy.

3.2.c Experimental set-up

The LSMs used in this study are forced at reference height (tower measurement height, Table 3.1) and with 30' time-steps for an entire year (1997, except for Tharandt where 1998 offered a more continuous time series). The methodology did not involve any tuning of parameters to match measurements (similar to Baker et al. (2003)) since it should reflect the use of LSMs coupled to distributed atmospheric models, where no such point-based tuning is possible.

All models were set up with the same initial soil thermal and hydrological conditions. Soil moisture layers were initialized at 50% of saturation. The soil surface temperature T_g was initialized with the first record of T_m and the deepest soil layer T_d was initialized with the yearly mean T_m. Any in-between thermal layers were linearly interpolated. Spin-up time for equilibrium was set to 5 years (after 2-3 years most sites did not show interannual change). The hydrological soil was divided into a 10cm surface layer, a 90cm root layer and a 3m deep soil layer (except the bucket soil, which used a 150mm soil water store).

The SiB 2.5 multi-layer soil heat scheme was divided into 6, 12, 24, 48, 100, 200cm discrete layers.

Soil type and land cover class were the only prescribed parameters (Table 3.1) and were chosen according to Fluxnet site specifications and matched to the classes used by the LSMs. The models then created biophysical soil and vegetation parameters from the model specific look-up tables. In addition, SiB 2.5 vegetation parameters were derived by time varying satellite remote sensing NDVI (Normalized Difference Vegetation Index) as described in (Stöckli and Vidale, 2004).

3.3 Results

3.3.a Soil moisture

Soil moisture measurements are generally difficult to compare with modeled values since soil properties vary by orders of magnitude on small spatial scales and they largely determine the scaling between volumetric water contents (measured) and absolute water contents (modeled). The analysis in this sub-section will focus on timing signatures and amplitude differences rather than on absolute soil moisture values.

In Figure 3.3 the seasonal course of root soil moisture is plotted for the six Fluxnet sites. The soil moisture curves for the two Mediterranean sites show a large seasonal cycle, with a substantial depression during summer while at the other sites a shallower soil moisture cycle is observed. The measured soil moisture in Collelongo drops from around 60% in May to 20% in August and in Castel Porziano from 50% in February to less than 20% in August. For Collelongo SiB 2.5 is able to reproduce the winter values of this large seasonal cycle, but does not drop to the observed summer values. The soil moisture simulated by BATS 1E remains at a lower level and has an even shallower seasonal cycle. BUCKET, having no biophysical control on water transfer, runs out of water already in June and only begins to recharge the soil in October. SiB 2.5 and BUCKET recharge the soil moisture store to almost full saturation, but not BATS 1E. BUCKET also shows a heavy summer dryness in CastelPorziano. BATS 1E soil moisture performs well at this evergreen forest while SiB 2.5 does not show such a pronounced soil moisture depression like observed. Its winter soil moisture is again comparable to observations.

The two central European sites have a shallow seasonal soil moisture cycle and soil moisture does not drop below critical values during summer. Again, the two models BATS 1E and SiB 2.5 are very similar and match observed soil moisture curves well for Vielsalm. Like in Collelongo BATS 1E exhibits a shallower cycle than SiB 2.5, which matches both the magnitude and timing of summer and winter values very closely. Both models overestimate the observed soil moisture by almost 20% at Tharandt, but the seasonal course of the soil moisture cycle is well represented. BUCKET shows a high soil moisture variability over the whole year, but summer precipitation is able to sustain the high evaporation needs of this simple model, so that the bucket never runs out of water like at the two Mediterranean sites.

The two northern European sites differ in their soil moisture cycle. A few soil moisture measurements are available for Gunnarsholt and BATS 1E and SiB 2.5 predict a shallow course in soil moisture at a high level while soil moisture in BUCKET constantly stays at a low level. The evergreen forest at Norunda shows a larger seasonal soil moisture cycle of similar magnitude (around 40%) like observed in the Mediterranean, but the soil

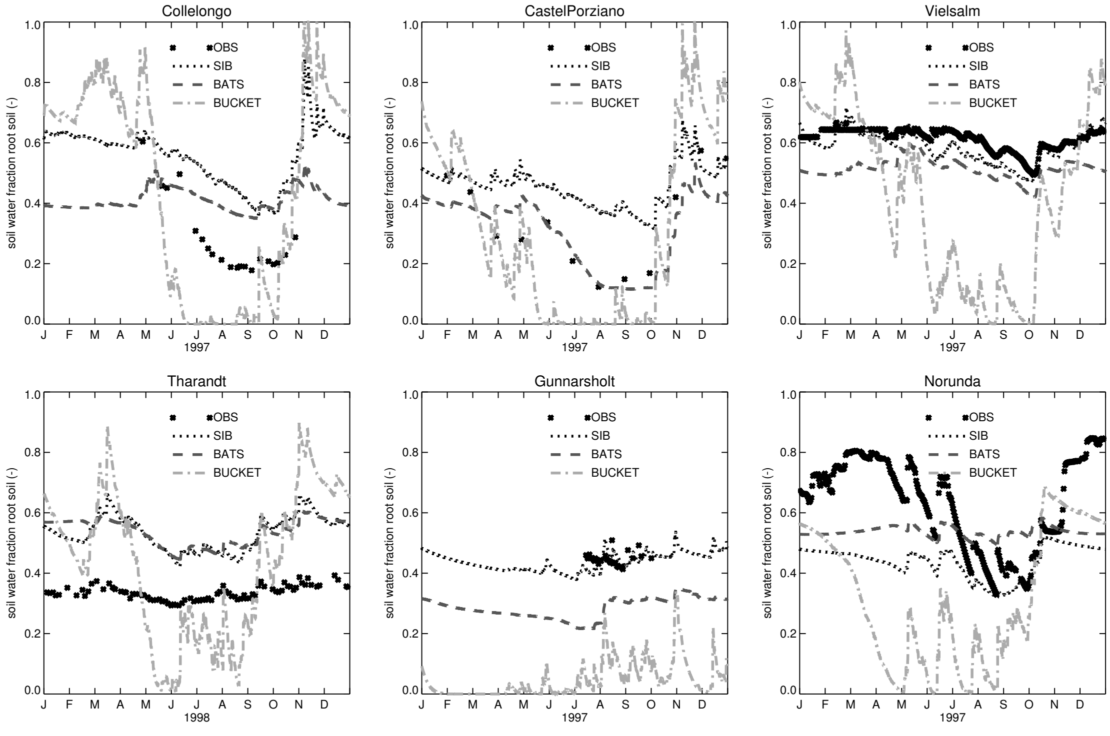

FIG. 3.3: Observed and modeled yearly root soil moisture

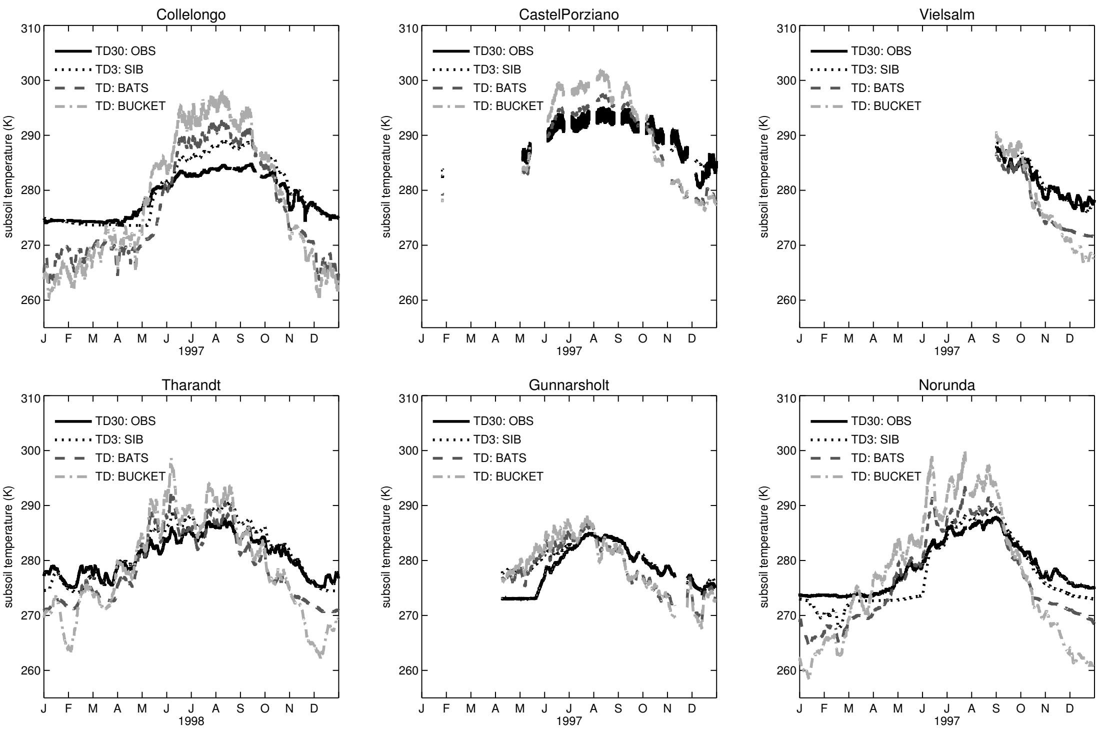

FIG. 3.4: Observed and modeled yearly soil temperature at 30cm

moisture there does not drop to a critical level during summer. Observed spring values are almost at saturation - possibly due to snowmelt. Summer values modeled by both BATS 1E and SiB 2.5 are in the same range as observations, but spring and winter values are lower than observed. This result may be explained due to an inaccurate snow depth initialization in the steady-state simulation using a 5 year spin-up period with the same yearly forcing data.

Summarizing these results, the two models using a biophysical control on evapotranspiration (BATS 1E and SiB 2.5) generally show a shallower seasonal soil moisture course which matches better with observations. Especially at the two Mediterranean sites BUCKET simulates a soil moisture depression which is not in accordance with observations.

3.3.b Soil temperature

Figure 3.4 shows observed and simulated soil temperatures at 30cm depth. Soil temperature at this depth does not have much diurnal variation but can help to explain the seasonal course of the surface heat balance. The general picture over all sites reveals that soil temperatures are well simulated by SiB 2.5 during the summer period but overestimated by BATS 1E and BUCKET. During winter SiB 2.5 again shows a good agreement with observations but BATS 1E and BUCKET underestimate soil temperatures during this season. At Collelongo soil temperature stays at the freezing point during this period in SiB 2.5 but responds instantaneously to short term changes in atmospheric forcing in the other two models. Snow depth is not shown in the figures but BATS 1E and BUCKET have a 150mm (120mm, respectively) thick snow layer between January-June (10-50mm in SiB 2.5) at this site. At Collelongo in particular all models overestimate summer soil temperatures by 5K (SiB 2.5) or more (>10K in BUCKET). The Mediterranean site Castel Porziano shows a reasonably good agreement between all models and observations during all periods. At this site soil temperature has a shallow seasonal course and always stays above the freezing point. In Vielsalm and Tharandt (in Vielsalm observations are limited to the September-October 1997) modeled summer soil temperatures are in good agreement with observations but only SiB 2.5 is able to reproduce the winter values which are above freezing in the observations.

BATS 1E and BUCKET underestimate the deep soil temperature by around 8K at Gunnarsholt between September and December. BATS 1E performs better at Norunda: there only BUCKET largely underestimates winter soil temperatures by about 10K.

The most prominent feature of SiB 2.5, with a multilayer diffusive soil heat transfer scheme, is that it is able to reproduce the seasonal course of the soil temperature at 30cm much better than the force-restore soil heat scheme used in BATS 1E and BUCKET.

3.3.c Heat and water fluxes

The differences in seasonal-scale soil moisture and temperature evolution shown in the previous two sub-sections can potentially control turbulent heat and water fluxes and the latter are analyzed in this section. Table 3.2 shows that the models simulate higher yearly mean LE than observed for Collelongo, the BUCKET being closest to observation and SiB 2.5 having the most evapotranspiration. H is underestimated by all models. Runoff compares well between models but is lower than derived from observations. In Figs. 3.5

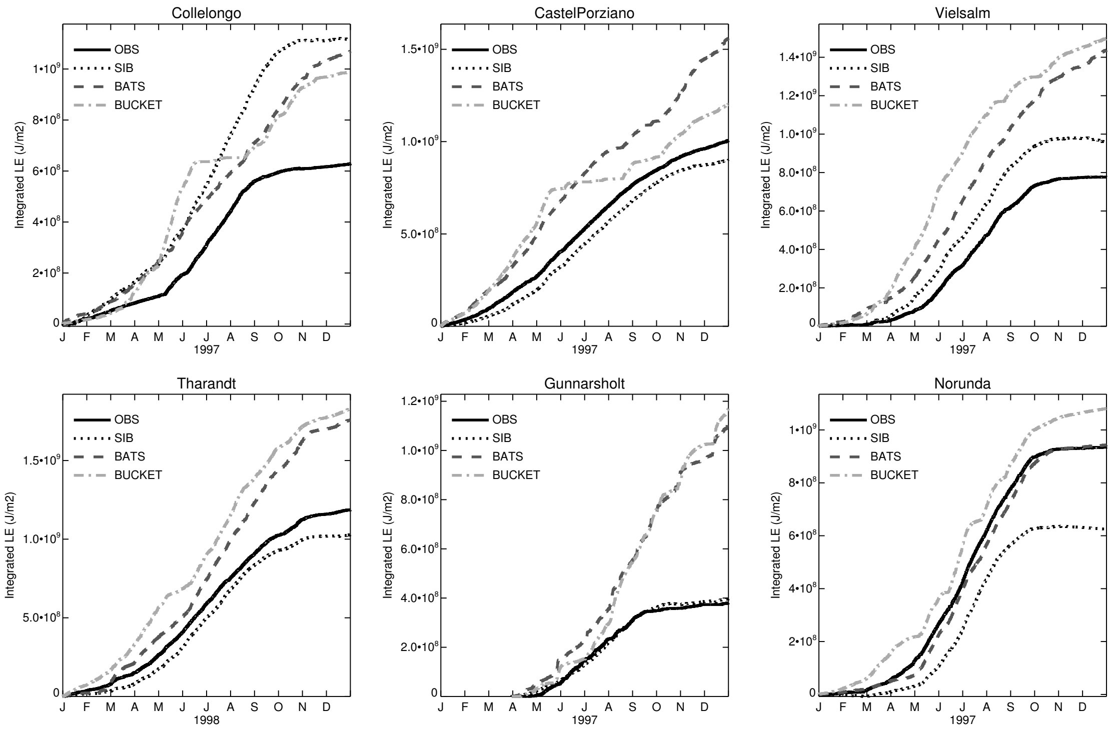

Fig. 3.5: Observed and modeled yearly integrated LE fluxes

and 3.6 the integrated LE and H fluxes are plotted. The plots allow to focus on the time signature of seasonal-scale fluxes rather than on absolute values (which is important due to a poor closure in the observed energy balance discussed in the methods section). The figures show that the seasonal course of LE and H at Collelongo is best represented by SiB 2.5, even though the integrated LE is much larger than observed. For this deciduous forest BATS 1E has no seasonal variation in its LE flux (large slope during the whole season) and BUCKET overestimates LE in spring and autumn and ceases evaporation during the whole summer (curve flattens during these months). Despite the inter-model differences in the seasonal course of LE the total yearly LE flux is very similar for all models. The timing of the diurnal course of LE and H during July (Figs. 3.7 and 3.8) matches best for SiB 2.5, followed by BATS 1E and BUCKET, the latter two underestimating the magnitude of LE during summer. Both models however show excessive LE and a depressed H during the other seasons.

In Castel Porziano the yearly mean LE flux has a substantial spread between models as can be seen from Table 3.2: the most complex model, SiB 2.5, comes closest to observations, underestimating evapotranspiration flux by 10.7%, where both BATS 1E and BUCKET overestimate LE by 54.9% and 19.4%, respectively. It can be seen from Figure 3.6 that a good performance of the yearly LE flux in SiB 2.5 also results in a good match of the yearly H flux while the overestimation of LE in BATS 1E results in underestimated H. BUCKET shows a similar summer LE anomaly like in Collelongo. Runoff is simulated well by SiB 2.5 and largely underestimated by BATS 1E and BUCKET.

The two central European sites Vielsalm and Tharandt are in the same latitudinal zone and the climatic conditions at both sites are comparable. SiB 2.5 shows a very

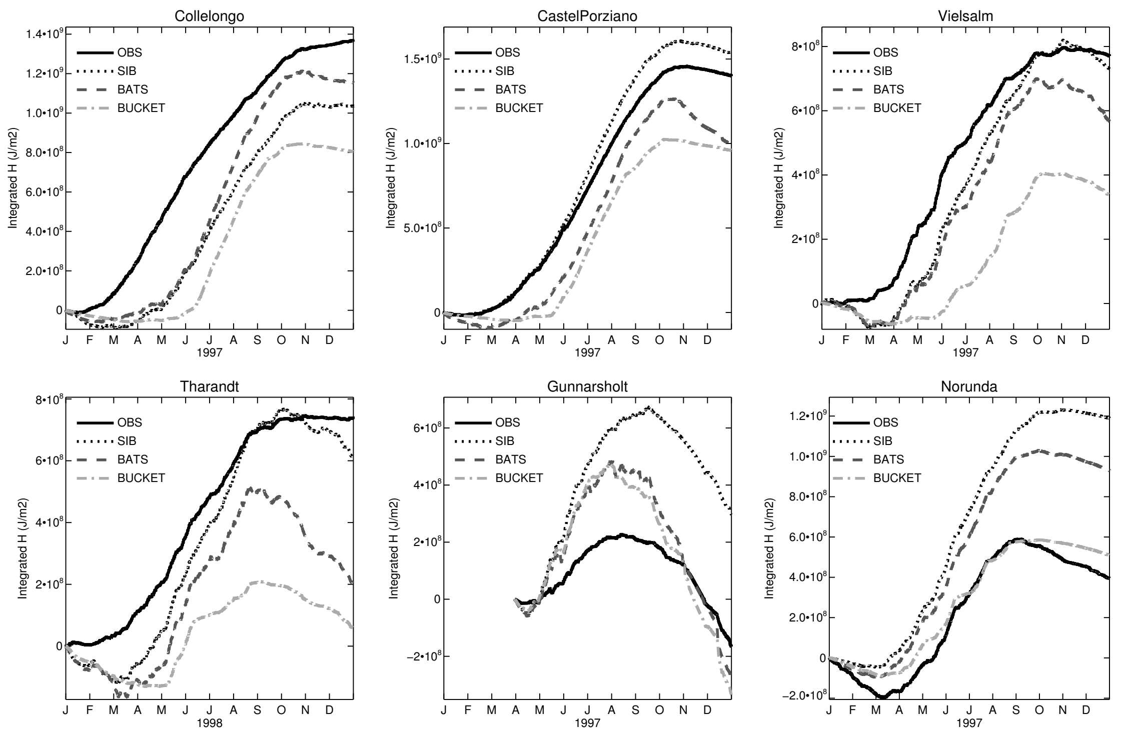

FIG. 3.6: Observed and modeled yearly integrated H fluxes

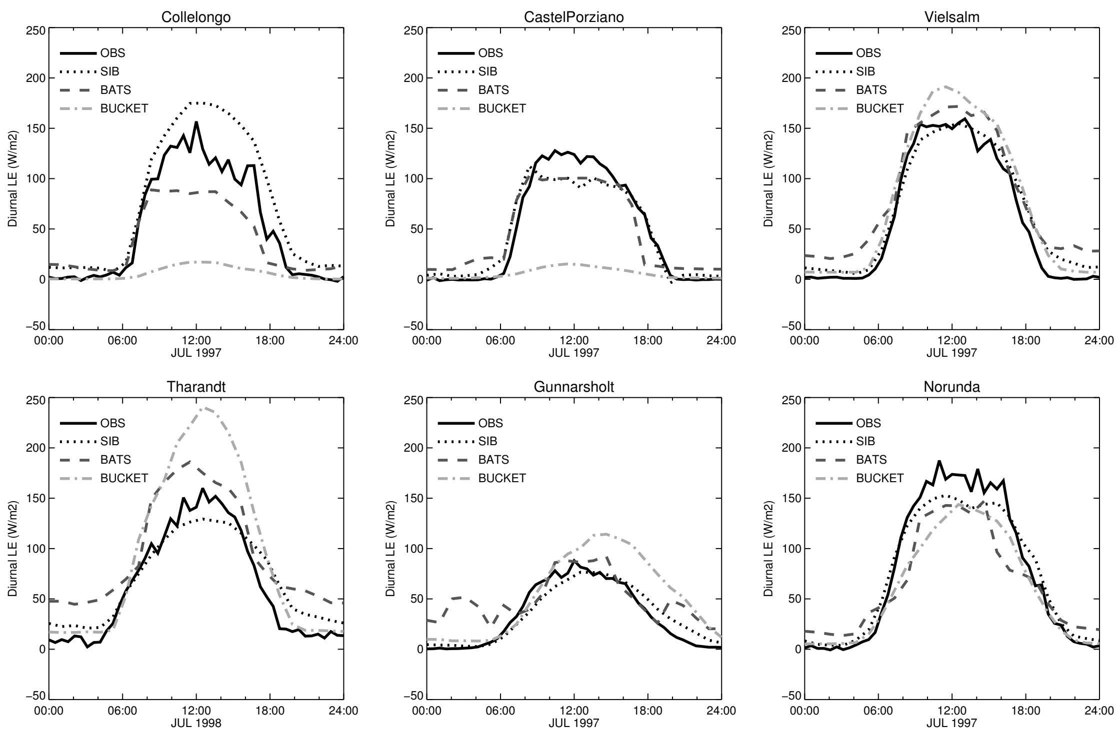

FIG. 3.7: Observed and modeled diurnal LE fluxes (July)

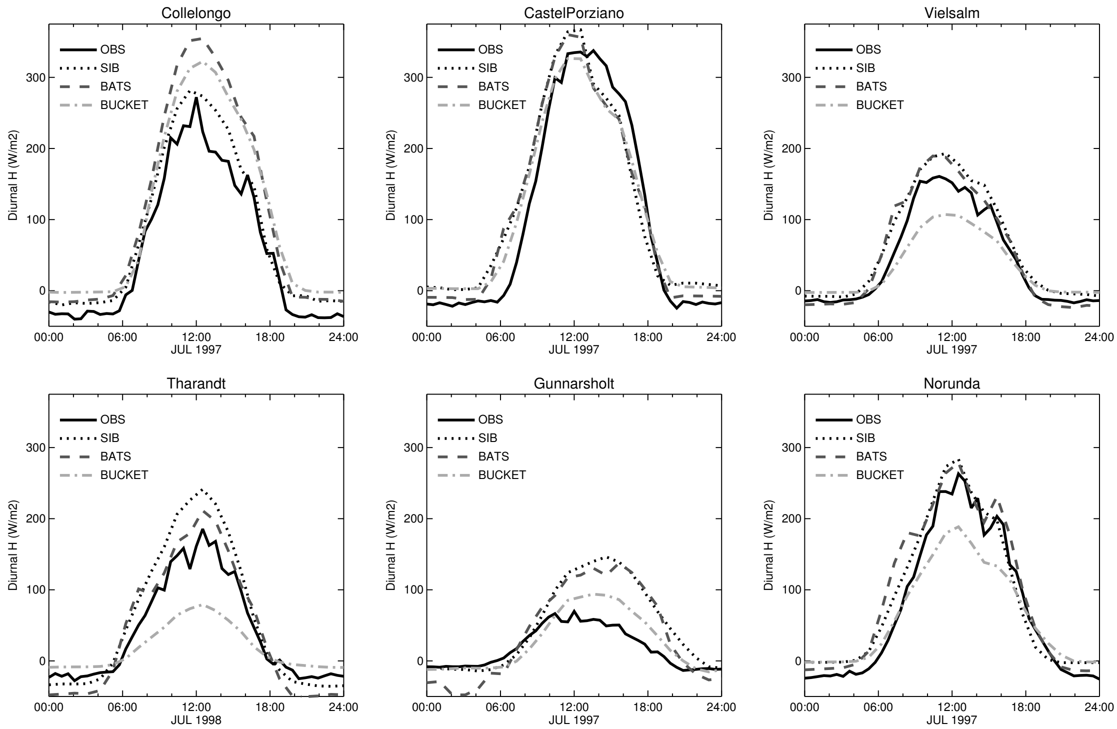

FIG. 3.8: Observed and modeled diurnal H fluxes (July)

good agreement to observations in yearly mean H and LE fluxes and also comes close to the observed evaporative fraction for the two sites. Both BUCKET and BATS 1E overestimate the yearly course of LE fluxes and underestimate H fluxes as this is shown in Figs. 3.5 and 3.6. At the evergreen forest at Tharandt BUCKET uses almost all available energy for evaporation resulting in an evaporative fraction close to unity. In Figure 3.7 it can also be seen that BATS 1E shows a displaced diurnal LE flux, even during night, which can explain its excessive yearly LE flux. Both, the timing and magnitude of the diurnal course of LE and H can be reproduced best with SiB 2.5. Runoff (Table 3.2) matches better with observations for the deciduous forest in Vielsalm than at the evergreen site; runoff is especially underestimated in BATS 1E and BUCKET for the evergreen forest.

Table 3.2 shows that Gunnarsholt receives the least net radiation of the six sites and observations show a negative mean sensible heat flux there. Both BATS 1E and BUCKET overestimate LE flux by a factor of 2.5, at the cost of only having little runoff. Again, the two models seem to use the available radiation for putting moisture into the atmosphere (Figure 3.5) while SiB 2.5 is able to almost exactly reproduce the relatively small latent heat flux associated with the short growing season of this northern European deciduous plantation. A good representation of the LE flux in SiB 2.5 also gives a good match in runoff, but it overestimates the H flux - especially during summer. Similar results are seen for the evergreen site Norunda. The modeled H fluxes for Norunda are larger than observed. BATS 1E matches very well in LE fluxes and in runoff while SiB 2.5 underestimates LE and overestimates runoff. On the diurnal scale all models perform well at Norunda but show a poorer performance in Gunnarsholt. Especially BATS 1E

TABLE 3.2: Mean net radiation (R_n), latent (LE), sensible (H) & ground heat (G), energy balance (BAL), runoff (R), evaporative fraction ($EF = \frac{LE}{H+LE}$) by site and model

	R_n [Wm^{-2}]	H [Wm^{-2}]	LE [Wm^{-2}] ([mm])	G [Wm^{-2}]	BAL [Wm^{-2}]	R [mm]	EF [-]
Collelongo (Deciduous, precipitation 1997: 981mm)							
OBS	83.5	43.3	19.9 (249)	-0.1	20.3	732	0.315
SiB	66.5	32.8	35.5 (444)	-1.8	0.0	557	0.520
BATS	71.3	36.6	33.9 (424)	1.8	-1.0	573	0.481
BUCKET	58.7	25.5	31.3 (392)	1.6	0.2	599	0.551
Castel Porziano (Evergreen, precipitation 1997: 399mm)							
OBS	112.0	44.4	31.9 (399)	0.6	35.1	399	0.418
SiB	77.0	48.6	28.5 (357)	-0.1	0.0	323	0.370
BATS	80.2	31.3	49.4 (618)	-0.4	-0.1	57	0.612
BUCKET	68.1	30.4	38.1 (477)	-0.5	0.1	199	0.556
Vielsalm (Deciduous, precipitation 1997: 770mm)							
OBS	71.7	24.4	24.6 (308)	0.2	22.4	462	0.502
SiB	54.2	23.1	30.3 (379)	0.6	0.0	392	0.567
BATS	61.6	18.0	45.6 (471)	-1.1	-0.8	211	0.717
BUCKET	56.2	10.7	47.5 (594)	-1.9	-0.1	180	0.816
Tharandt (Evergreen, precipitation 1998: 793mm)							
OBS	61.2	23.4	37.6 (471)	-0.2	0.4	322	0.617
SiB	52.0	19.5	32.6 (408)	-0.1	0.0	387	0.626
BATS	59.0	6.4	55.8 (698)	-2.6	-0.6	95	0.896
BUCKET	57.5	1.9	58.0 (726)	-2.4	-0.1	78	0.969
Gunnarsholt (Deciduous, precipitation APR-DEC 1997: 471mm)							
OBS	47.1	-6.1	18.1 (227)	0.9	34.2	320	1.770[1]
SiB	33.7	15.8	17.9 (224)	0.0	0.0	303	1.437[1]
BATS	37.6	-10.6	50.4 (631)	-1.2	-0.6	8	2.761[1]
BUCKET	36.9	-14.0	53.8 (673)	-3.2	0.2	0	2.420[1]
Norunda (Evergreen, precipitation 1997: 431mm)							
OBS	59.7	12.7	29.6 (370)	0.0	17.4	61	0.700
SiB	57.9	38.4	19.8 (248)	-0.3	0.0	222	0.340
BATS	56.8	30.1	29.9 (374)	-2.9	-0.2	60	0.499
BUCKET	47.1	16.4	34.3 (429)	-3.4	-0.2	6	0.677

[1] Values >1 because of negative sensible heat fluxes.

cannot reproduce well the nighttime fluxes at Gunnarsholt and BUCKET overestimates the magnitude of the daytime LE flux.

3.4 Discussion

3.4.a Mediterranean

A large inter-model variability of LE for the two Mediterranean sites Collelongo and Castel Porziano is seen on the diurnal and the seasonal time scale (Figure 3.5 and 3.7).

All three models come to roughly the same yearly total LE in Collelongo but during the growing season they each largely present their own solution as this was shown in the results section. Collelongo receives around 83.5Wm^{-2} of mean net radiation (Castel Porziano: 112Wm^{-2}), and observations indicate that only 31.5% of this energy is transferred into latent heat (Castel Porziano: 41.8%). This fraction is much higher at central European sites (50.2% at Vielsalm and 61.7% at Tharandt). Such a high energy availability at the two Mediterranean sites results in a high atmospheric demand and requires a biophysical limitatation of the water transfer between the biosphere and the atmosphere and a sufficent soil water storage capacity to sustain this water flux during dry periods. BUCKET with no such regulation mechanism highly overestimates LE in spring and autumn, running out of water during summer, which is shown in the yearly soil moisture curves (Figure 3.3). This model then overestimates soil temperatures in summer by around 10K and has an exaggerated H flux (day and night) because it has no evaporative cooling during this period. In Castel Porziano BUCKET LE shows a similar seasonal course but there the difference between the biophysical model BATS 1E and the photosynthesis-conductance model SiB 2.5 is large. At this site precipitation in 1997 was 399mm and much lower than at Collelongo (981mm). The observed soil moisture curve therefore shows very low values during summer in Castel Porziano and BUCKET is strongly soil moisture limited during this period (but not BATS1E and SiB 2.5, BATS 1E is however close to the wilting point) due to its lacking biophysical control on water transfer. The difference between the BATS 1E and SiB 2.5 LE fluxes can be explained with eq. 3.4 and 3.5. Evapotranspiration in both models are limited by T, δe, W and PAR and but at high atmospheric demands plant biochemistry in SiB 2.5 can also limit LE, which is the the large difference between the two models. The photosynthesis process is driven by the availability of nutrients, light and the ability of the plant to use the photosynthesis products and since this process is not included in BATS 1E it highly overestimates the yearly integrated LE flux while observations and SiB 2.5 show an upper limit of around $1 \cdot 10^9$ Jm^{-2}. The exaggerated LE of BATS 1E results in a larger soil moisture depression during summer, which is, however, better in accordance with observations. On the other side LE and H fluxes of SiB 2.5 at this site better compare with observations, which may put in question the observed soil moisture at this site. As already suggested the representativeness of absolute soil moisture values is not straight forward, considering the spatial heterogeneity of this variable.

3.4.b Central Europe

At the two central European sites observed soil temperature is mostly above freezing and soil water has a very shallow seasonal course at a high mean level as shown in Figs. 3.3 and 3.4, therefore neither of these variables are largely controlling biophysical processes over the seasonal course. Rainfall totals to 770mm in Vielsalm and 793mm in Tharandt and does not show much seasonal variability. Yearly Heat and Water fluxes are best simulated by SiB 2.5 and the other two models overestimate LE and underestimate H for both sites resulting in an excessive evaporative fraction (Table 3.2) in these models. Due to the balanced environmental conditions at Vielsalm and Tharandt water fluxes of BUCKET (eq. 3.3) and BATS 1E (eq. 3.4) are only constrained by the diurnal course of PAR but not so much by W, T and δe. In this case, the SiB 2.5 transpiration still obeys to the maximum photosynthesis rate which is especially sensitive to nutrients (V_{max0}) and PAR

(eq. 3.5). SiB 2.5 distributes these quantities through the vertical extent of the canopy by the use of an extinction function dependent on $FPAR$ which obeys the seasonal course of phenology (also see Sellers et al. (1997a)). The latter is especially important for the deciduous forest Vielsalm. Figure 3.5 shows that the seasonal course of LE is very well reproduced by SiB 2.5 (leveling to around $1 \cdot 10^9$ Jm^{-2} in the yearly total, also in Tharandt) but not by the other two models (which show a low seasonality in their LE course). Their excessive LE fluxes result in depressed seasonal-scale H fluxes, also visible on the diurnal time scale in Figs. 3.7 and 3.8 for the BUCKET model. Furthermore H fluxes in BATS 1E are negative during stable conditions (night, morning, evening) and its diurnal LE course starts earlier than the one of SiB 2.5. As was shown in Vidale and Stöckli (2005) (this issue) the CAS storage capability in SiB 2.5 can support the storage of heat and water during times of low turbulence. At night this storage prevents excessive cooling of the surface layer and during transition times between stable and unstable surface layer stratifications it delays the start of turbulent fluxes, which is well demonstrated in the diurnal course of LE (Figure 3.7) and H (Figure 3.8) at Vielsalm and Tharandt.

3.4.c Northern Europe

At the northern European sites a low amount of R_n is available for land surface processes during a short time period. At the Icelandic site Gunnarsholt BUCKET and BATS 1E almost completely use it for LE and even show a negative H flux in the mean (Table 3.2). Soil moisture is not limiting BUCKET evaporation at this site (Figure 3.3) and the relatively mild air temperature in south-western Iceland is not controlling biophysical processes in BATS 1E. Due to a short growing season and the low amount of available energy only about half of the integrated LE is observed at this site compared to the others. Therefore plant biochemistry is not operating at its full capacity which means that SiB 2.5 photosynthesis limitation cannot explain why a more sound energy partitioning is seen in this particular model. Unlike for the other sites, where inter-model differences show up during summer, the main difference in the integrated LE fluxes are seen only after August. A large divergence between BATS 1E / BUCKET and SiB 2.5 is observed also in the H flux. The reason for this inter-model difference can be found by analyzing their thermal soil scheme. BUCKET and BATS 1E use a simple force-restore scheme (extending to around 1m depth) and show a negative bias of up to 5-15K in soil temperatures after August compared to observations, which transfer into negative sensible heat fluxes (since H is largely driven by radiation and the soil surface temperature) and exaggerated LE fluxes (since LE is mostly driven by radiation at this site). Only a diffusive 4m deep thermal soil scheme used in SiB 2.5 is able to reproduce the soil temperatures correctly, resulting in a higher H flux. Radiation is limiting at Gunnarsholt outside the growing season and then the soil heat flux becomes an important driver for the partitioning between LE and H since LE is not driven by plant biophysics anymore. Soil temperatures simulated with the force-restore scheme also are underestimated at the other sites but there solar radiation and plant biophysics drive the surface energy balance during most of the year as this was shown in the previous two sub-sections. At Norunda for example, a longer growing period and a higher mean net radiation results in a 2.5 times higher LE than at Gunnarsholt. There all models show skill in representing the seasonal course of LE flux (BATS 1E being closest to observations) since the seasonal course of LE is mostly driven by PAR and T (winter) but not to a large extent by the other factors in eqs. 3.3 - 3.5.

3.5 Conclusion

In this study, three land surface models of different complexity were applied at six European Fluxnet sites. Processes of soil moisture and heat storage and their biophysical interaction with seasonal-scale land surface fluxes were analyzed. The focus was not in obtaining the best local scale modeling results but to understand how land surface processes simulated by todays LSMs drive the hydrological cycle on the seasonal time scale dependent on the climatic environment.

Results show that a latitudinal gradient in net radiation translates to a latitudinal gradient of the evaporative fraction, being lowest in the Mediterranean and highest in northern Europe. Extreme environmental conditions on the seasonal time scale, either dryness or coldness, require long term storage processes like soil heat and soil moisture storage to be part of the modeling system. Dry summer conditions in the Mediterranean require a biophysical (stomatal-) control of the water flux and also a storage capability for water in the root soil to hold this water for a prolonged period. Both processes are not present in the BUCKET model and it shows a poor performance in the Mediterranean. Modeling the land surface in northern Europe requires a soil heat scheme of monthly to seasonal storage capacity. BATS 1E and BUCKET, using a simple force-restore soil heat scheme, largely overestimated LE after the end of the growing season where not plant biophysics, but the surface heat balance drives surface fluxes. In central Europe the seasonal course of LE and H can be controlled by plant biochemistry and the timing and phase of vegetation phenology. In this case, the biophysical approach used in BATS 1E overestimates LE fluxes and underestimates H fluxes on the seasonal time scale, which is not the case for the photosynthesis-conductance model SiB 2.5.

Despite the difficulties encountered in parts of the driver data (the authors suggest that LW_d becomes part of the Fluxnet dataset), it was demonstrated that the integration of Fluxnet site measurements and land surface modeling is helpful in revealing and exploring missing processes of the hydrological cycle which could be relevant for coupled climate simulations. Runoff is a critical component of this cycle and largely varied by scheme. Therefore our future focus will be in using a similar modeling set-up to explore the catchment-scale soil moisture - runoff interaction, a scale where measurements of runoff are available and reliable.

3.6 Acknowledgements

The funding for this study was provided by the National Centre of Competence in Research on climate variability, predictability, and climate risks (NCCR) funded by the Swiss National Science Foundation (NSF). The support of the ETH institute of Climate and Atmospheric Science and of Prof. Christoph Schär is gratefully acknowledged. We would like to thank to Richard Olson and Eva Falge for distributing the Fluxnet/Euroflux data and coordinating the Fluxnet project. Additional soil moisture and temperature data for this study was provided by Giorgio Matteucci (Collelongo site, JRC, Italy), Giampiero

Tirone (Castel Porziano site, Unitus, Italy), Bernard Heinesch (Vielsalm site, FUSAGx, Belgium), Christian Bernhofer (Tharandt site, TU Dresden, Germany), Anders Lindroth and Harry Lankreijer (Norunda site, LU, Sweden), and Jon Gudmundsson (Gunnarsholt site, Agr. Res. Institute, Iceland). Thanks to Scott Denning (CSU) for the permission to use SiB2 and Mapper and to Jim Tucker, Jim Collatz and Sietse Los (NASA/GSFC) for their support on satellite remote sensing and land surface modeling.

Chapter 4

Sensitivity of the diurnal and seasonal course of modeled runoff to three different land surface model soil moisture parameterizations

Sensitivity of the diurnal and seasonal course of modeled runoff to three different land surface model soil moisture parameterizations *

Reto Stöckli †, Pier Luigi Vidale ‡, Aaron Boone §, Martin Hirschi ¶ and Christoph Schär ‖

ABSTRACT

Land surface models (LSMs) used in climate modeling include detailed above-ground biophysics but usually lack a good representation of soil hydrological processes. While evapotranspiration can be modeled and measured at a wide range of scales, runoff is a local scale process linked to topography and can only be measured at the catchment-scale. Both processes are closely linked through soil moisture, which is treated as a subgrid-scale process in climate modeling. To explore this connection, catchment-scale LSM simulations are performed with the use of three different soil moisture parameterizations over the Rhone catchment for the years 1986-1988. Results show that the use of a multilayer soil in comparison to the widely used 3-layer soil allows a better reproduction of the seasonal dynamics of runoff. Including lateral soil moisture flow significantly enhances monthly runoff performance and provides an effective means to recover from the dry soil moisture conditions at the end of summer. Snowmelt runoff in the Alpine part of the catchment is sensitive to resolution and none of the used parameterizations can account for this process. Runoff in the temperate part of the Rhone performs well at larger scales without using lateral soil moisture flow. Overall, accuracy in timing and magnitude of simulated runoff is substantially increased by the use of lateral soil moisture flow, especially at the daily time-scale. However evapotranspiration is not sensitive to the different parameterizations of soil moisture processes in the Rhone catchment.

*in preparation for submission to Journal of Hydrometeorology

†Reto Stöckli, Institute for Atmospheric and Climate Science, Winterthurerstrasse 190, 8057 Zürich, Switzerland. e-mail: stockli@env.ethz.ch, phone: +41 1 635 5209

‡Pier Luigi Vidale, Institute for Atmospheric and Climate Science, Winterthurerstrasse 190, 8057 Zürich, Switzerland. e-mail: pier-luigi.vidale@ethz.ch, phone: +41 1 635 5218

§Aaron Boone, Centres d'Etudes Spatiales de la Biosphère, 18 avenue Edouard Belin, Room 214, 31401 Toulouse, France, e-mail: aaron.boone@free.fr

¶Martin Hirschi, Institute for Atmospheric and Climate Science, Winterthurerstrasse 190, 8057 Zürich, Switzerland. e-mail: martin.hirschi@env.ethz.ch, phone: +41 1 635 5242

‖Christoph Schär, Institute for Atmospheric and Climate Science, Winterthurerstrasse 190, 8057 Zürich, Switzerland. e-mail: christoph.schaer@env.ethz.ch, phone: +41 1 635 5199

4.1 Introduction

The overall aim of climate modeling is to study the climate system by use of realistic numerical representations of the individual earth system components. Land surface hydrological processes are considered to be very important (e.g. Dickinson (2001)) and improving their treatment in climate models is recognized as a priority (Intergovernmental Panel on Climate Change, 2001). While current land surface models (LSMs) include physically based formulations of plant physiological processes (Sellers et al., 1997a; Pitman, 2003), soil moisture and runoff are usually poorly represented. However, as suggested by Koster and Milly (1997) and Ducharne et al. (1998) the land surface water balance is controlled as much by evapotranspiration as it is by runoff.

The importance of correctly representing soil moisture and runoff processes in climate models has been shown in a number of studies (e.g. Gedney and Cox (2003), Gedney et al. (2000), Ducharne et al. (1998), Douville (2003) or Arora and Boer (2002)). Soil moisture is considered as an initial value problem for numerical weather forecasting (Pielke Sr et al., 1999; Douville, 2004). Soil moisture - atmosphere feedbacks are important in semi-arid and temperate climates (Schär et al., 1999) and land-use changes in such areas can modify the regional water cycle (Heck et al., 2001). Lettenmaier (2001), Chen et al. (2001), Noilhan et al. (1997) and Pielke Sr (2001a) provide evidence that the integration of soil hydrology and vegetation biophysics and biochemistry in climate models helps to understand land surface processes and allows a better modeling of the climate system.

Most LSMs used in climate modeling simulate radiation, heat and water exchanges directly at the RCM (regional climate models, typically 0.5° grid spacing) or GCM (general circulation models, 1° or larger grid spacing) spatial scale. The scaling problem of above-ground biophysical processes is generally accounted for by defining effective soil and vegetation parameters (Noilhan et al., 1997) or by the use of subgrid-tiling (mosaic approach, Avissar and Pielke (1989), Koster and Suarez (1992)). Soil moisture and runoff processes are more difficult to measure and to model because of their fine-scale spatial and temporal variability (Western et al., 2002; Liang and Xie, 2001). LSMs generally assume that local scale runoff occurs due to the following processes:

1. Infiltration excess runoff (Horton runoff) is produced when rainfall intensity exceeds the infiltration capacity of the soil. This type of surface runoff is largely driven by heavy convective rainfall, which is a subgrid-scale process in climate modeling. Sellers et al. (1996d) and Noilhan et al. (1997) propose a statistical distribution of rainfall intensity to account for this scaling problem.

2. Saturation excess runoff (Dunne runoff) is a second type of surface runoff and occurs when rain falls onto a completely saturated soil and therefore depends on the existing soil moisture content.

3. Drainage runoff (interflow) occurs where soil moisture exceeds field capacity and is a slow process compared to the previous two surface runoff mechanisms. Water has to infiltrate into the soil first and generates a delayed response in the catchment runoff after a rainfall event (occurs faster on slopes).

4. Groundwater flow (or baseflow) is a lateral redistribution of soil water in the saturated zone and may lead to runoff into a stream bed. Flow velocity in the soil decreases sharply with dryer soil conditions and with increasing depth, so that this process is of importance when the following conditions exist: (a) high soil moisture and (b) topography. Groundwater flow has characteristic maximum velocities of 0.1-10 [m day^{-1}], which is slow compared to surface runoff, but it may determine the seasonal-scale soil moisture conditions, which then, in the case of a rainfall event, drive saturation excess (2) and drainage runoff (3).

While (1)-(3) are part of most LSMs, (4) is not widely used since it is a subgrid-scale process. Stieglitz et al. (1997), Koster et al. (2000a), Ducharne et al. (2000), Walko et al. (2000), Gedney and Cox (2003) and Yang and Niu (2003) use statistical relationships between topography and soil moisture to solve this scaling problem. The framework is based on the general hypothesis in hydrology that topography is the main driving force for drainage runoff and water table changes. Similar to the mosaic approach, which is used to account for above-ground land cover heterogeneity (Avissar and Pielke, 1989), large-scale atmospheric grids are divided into subgrid patches, each having its own soil moisture balance and ground water level, depending on subgrid-scale lateral water fluxes between the patches.

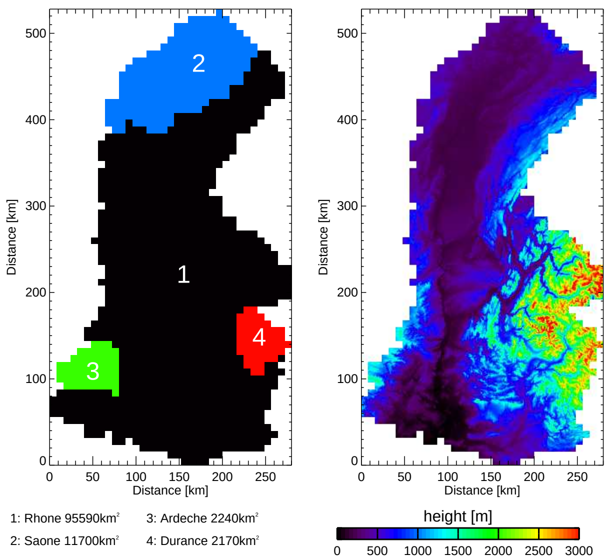

Fig. 4.1: The Rhone (1, including 2, 3 and 4) basin with the Saone (2), Ardeche (3) and Durance (4) sub-catchments (left) and the 1km topography (derived from the USGS GTOPO30 dataset)

Several model inter-comparisons have been aiming at exploring these processes, including PILPS 2(c) (Wood et al., 1998; Lohmann et al., 1998; Liang et al., 1998) and PILPS 2(e) (Bowling et al., 2003a; Nijssen et al., 2003; Bowling et al., 2003b). The Rhone-AGG experiment by Boone et al. (2004) showed that todays LSMs simulate very different runoff and soil moisture, but that subgrid-scale soil moisture improves runoff. Idealized (Walko et al., 2000), offline (Niu and Yang, 2003) and GCM experiments (Gedney and Cox,

2003) employing subgrid-scale soil moisture improves modeled global soil moisture and runoff fields, but many questions remain in terms of process-scaling and heterogeneity of soil parameters. Facing these uncertainties, this study focuses on the question whether catchment hydrology can be internalized in a physically based LSM, in comparison to parameterized runoff schemes used in hydrological science. It is furthermore important to know whether such an approach holds at the large scales used in climate research, and if subgrid-scale soil moisture parameterizations allow to better simulate runoff, which is sensitive to the high spatial and temporal dynamics of soil moisture and topography as reviewed above. When such parameterizations are useful, it is necessary to explore in what climatic regime they are effective and how they influence the land surface water cycle.

To answer these questions a LSM, SiB 2.5 (Simple Biosphere model version 2.5, (Sellers et al., 1996d; Vidale and Stöckli, 2005), schematic displayed in the left part of Figure 4.2), is applied off-line at catchment-scale. Similar to Baker et al. (2003) the models large-scale parameter sets are used without any tuning. Experiments are performed at different spatial scales (8km, 0.5° and 1°) testing sensitivity of the land surface hydrological cycle to the parameterization of the vertical soil parameterization (number of layers) and the horizontal resolution of soil processes (grid- or subgrid-scale lateral water flow). The model is forced off-line in the Rhone catchment (Figure 4.1) with the use of the high resolution observational database of the Rhone-AGG (Rhone Aggregation) initiative (Boone et al., 2004). Rhone-AGG is part of the GEWEX (Global Energy and Water cycle EXperiment), and aims at intercomparing LSMs for a regional scale scale river basin over the Rhone catchment, providing data from a dense observation network. The Rhone catchment consists of a wide range of climatic zones ranging from Mediterranean (Ardeche) to high altitude Alpine (Durance) and temperate climates (Saone) and the continuous and multi-year validation data provide a unique possibility for process-based analysis of model results. This close interaction between land surface modeling and observational initiatives at catchment-scale can help to better understand the land surface hydrological cycle on seasonal to interannual time-scales, which is justified, concerning the above listed uncertainties in this field. Findings from this study will finally be helpful for modeling runoff - soil moisture interactions in coupled climate simulations.

In the next section the model, the validation dataset and the experimental set-up are described. The results are presented separately for monthly and daily time-scales and compared to observed runoff. Modeled snow water equivalent is compared to observed snow depths and the terrestrial water storage is used as an integrative validation source to explore the land surface hydrology of the Rhone catchment.

4.2 Methods

4.2.a Model description

The third generation land surface model SiB 2 (Simple Biosphere model version 2 by Sellers et al. (1996d)) is used in this study with a new solution core including a prognostic canopy-air-space (afterwards named SiB 2.5, see Vidale and Stöckli (2005), see Figure 4.2, left). SiB 2.5 has been successfully used over a wide range of spatial and temporal scales off-line by Baker et al. (2003) and Stöckli and Vidale (2005) and coupled by Denning et al. (2003) .

The Sellers et al. (1996d) 3-layer vertical soil moisture transfer scheme is used, but in addition a new multilayer soil moisture transfer scheme after Bonan (1996) using a vertical root distribution by Zeng (2001) and an exponential decay of saturated hydraulic conductivity with depth is implemented. Both schemes create infiltration excess and saturation excess runoff from the top soil layer and drainage runoff from their deepest soil layer. The use of both schemes side-by-side allows a testing of sensitivity of the hydrological cycle to the complexity of the vertical soil moisture parameterization.

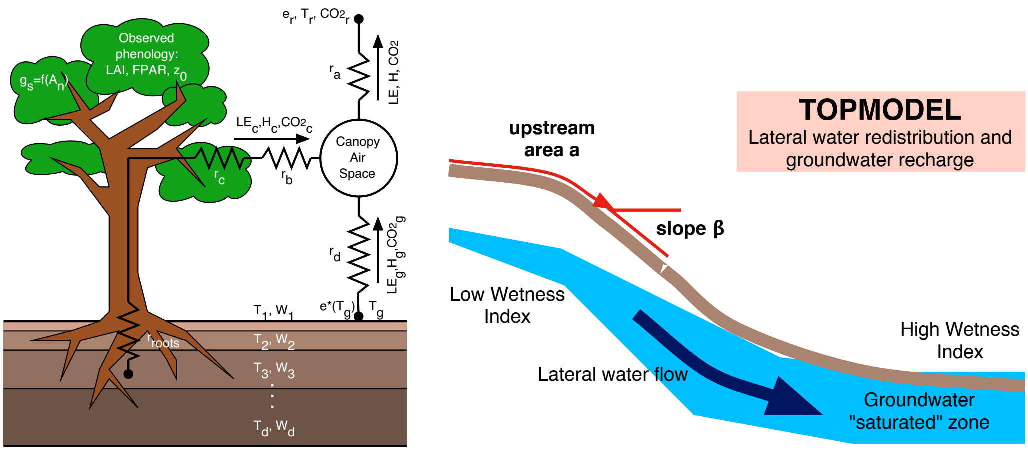

FIG. 4.2: SiB 2.5 Land Surface Scheme (vertical water fluxes) and the Topmodel approach (lateral water fluxes)

The subgrid-scale soil moisture parameterization coupled to the multilayer SiB 2.5 soil is based on Topmodel by Beven and Kirkby (1979), which is a simple but physically-based hydrological model, and allows for horizontal water transfer below the ground water table. Using a schematic description, terrain slope $\tan\beta$ [-] generates a lateral water flux q [m^2s^{-1}] depending on the height of the steady-state water table z_w^∞ [m], which is sustained by the lateral inflow from recharging climatological precipitation R [ms^{-1}] supplied by the the upstream catchment area per unit topography contour length a [m],

$$q = aR = \frac{K_s(0)}{f} e^{f z_w^\infty} \tan\beta, \qquad (4.1)$$

where $K_s(0)$ is the saturated hydraulic conductivity [ms^{-1}] at the surface and f is the e-folding depth [m^{-1}] of K_s. This formulation creates a steady-state water table, because hydraulic conductivity decreases with depth. More generally, a rise (lowering) of the water table out of its equilibrium state creates a deviation of the lateral water flux from (to) this area. Topmodel (Figure 4.2, right), as used in this study, relates the water table to local scale topography by use of a time-invariant Wetness Index W (W has units of ln(m) but in Topmodel its use is restricted to $W - \overline{W}$, which renders it dimensionless)

$$W = \ln\left(\frac{a}{\tan\beta}\right), \tag{4.2}$$

where W describes the long-term tendency of an area to gain or lose water in the saturated soil. Lowland areas have high W and their water table is close to the surface. These areas often saturate and can generate saturation excess runoff. Areas with significant topography generally have low W values but large slopes (β) and therefore show a faster lateral groundwater flow and interflow. As a result, soil moisture and runoff change according to topography, which has a very fine-scale variability in mountainous areas. The Topmodel approach, adapted for use in climate research by Koster et al. (2000a), Walko et al. (2000) and Gedney and Cox (2003), uses a discrete number N of subgrid patches p, each being assigned with a unique W_p value, reflecting the statistical distribution of subgrid-scale topography, and covering a fractional patch area A_p [-]. W_p distributions for the Rhone, Saone, Ardeche and Durance basins are shown in Figure 4.3. Each subgrid patch generates its own water table according to its patch-scale topography

$$z_p^\infty = \overline{z} + \frac{1}{f}(W_p - \overline{W}) \quad \text{where} \quad \overline{z} = \sum_{p=1}^{N} z_p A_p, \tag{4.3}$$

where z_p is the instantaneous patch water table and $\overline{z}$ is the instantaneous water table averaged over all patches. Rainfall, snowmelt and evapotranspiration then drive groundwater flow between these patches. Grid-scale drainage runoff occurs from sufficiently saturated soil layers in every patch and depends on patch slope angle. The full implementation of this scheme is found in Walko et al. (2000).

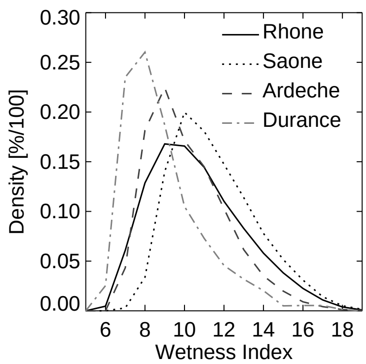

FIG. 4.3: Wetness Index distributions for the Rhone catchment and the Saone, Ardeche and Durance sub-catchments

4.2.b Driver dataset

SiB 2.5 is forced at reference level (30m) with down-welling radiation (shortwave/longwave), wind, temperature, relative humidity, rainfall and surface pressure provided at an 8km spatial grid and at a 3h interval for the Rhone catchment spanning the years 1985-1989 provided by the Rhone-AGG initiative (Boone et al., 2004). The SiB 2.5 snowfall parameterization was used (even though Rhone-AGG provides frozen/liquid precipitation). The Hansen et al. (2000) UMD (University of Maryland) land cover map and the FAO (1995) Digital Soil Map of the World were used to derive spatially distributed vegetation and soil parameters according to the standard SiB 2.5 vegetation and soil look-up tables. The AVHRR based 1982-2001 EFAI-NDVI dataset (Stöckli and Vidale, 2004) was used to derive time-dependent vegetation parameters.

4.2.c Validation dataset

Model results have been validated using observed monthly runoff from the Rhone (size: 95590km^2, mean altitude: 685m), Saone (11700km^2, 330m), Ardeche (2240km^2, 677m) and Durance (2170km^2, 2149m), and daily runoff from the Ain (1251km^2, 728m) and Ognon (2129km^2, 332m) sub-catchments are provided by the Rhone-AGG initiative. Snow depths are evaluated in an independent analysis provided by A. Boone. 24 snow measurement sites (Boone et al., 2004) are compared to modeled snow water equivalent (SWE) of nearest grid cells by use of a snow density (model constant) of 250kg m^{-3}. A key variable of the land surface in the mid-latitude is the seasonal soil water depletion that occurs during the summer season. As there are no large-scale observations of soil moisture available, we resort to an indirect validation using diagnosed values of total terrestrial water storage (TWS), which represents the sum of all storage terms (soil moisture, groundwater, snow, lakes). The methodology combines atmospheric water vapor convergence estimates from the ERA-40 reanalysis and conventional river runoff data from the gauge Beaucaire (France). It provides estimates of catchment-averaged monthly TWS changes. The methodology has been developed and successfully validated using data from Illinois (Seneviratne et al., 2004), and is currently applied to a large number of mid-latitude catchments. The current application stretches the method to its limits, due to the comparatively small area and complex topography of the Rhone catchment, and a slow drift in the data is removed by requiring the proper long-term balance (zero storage changes in the longterm mean).

4.2.d Experimental set-up

3-year model integrations were performed for the years 1986-1988. The experiments explore the sensitivity of the hydrological cycle to the vertical and horizontal parameterization of soil moisture and runoff, as shown in Table 4.1. Each parameterization is applied at different scales: in the RCM and GCM experiments, the original Rhone-AGG forcing data were area-averaged from the 8km scale to 0.5° and 1° so that these experiments reflect the model's use at standard climate modeling resolutions. The multilayer+Topmodel simulations have only been applied at the RCM and GCM scale, since these are the scales where the use of subgrid-scale soil moisture is expected to have the most impact.

The model soil was initialized at full saturation and 285K with no surface snow on 1. August 1985, and experiment spin-up was 1.5 years (August 1985 - December 1986, then restarting in January 1986). Soil layers in the 3-layer experiments were set up with the following depths: 0.02m, 1-1.5m (depending on vegetation type), 2.5-3.0m (depending on vegetation type). Soil layers in the Multilayer experiments were set up as follows:

Table 4.1: Experimental matrix

Parameterization	8 km (8KM)	0.5° (RCM)	1° (GCM)
3 Layer	3L-8KM	3L-RCM	3L-GCM
Multilayer	ML-8KM	ML-RCM	ML-GCM
Multilayer + Topmodel		MLTOP-RCM	MLTOP-GCM

0.1m top soil with a scaling factor of 1.25 for successive layers: this creates a total soil depth of 3.3m in the 10 layer soil. A deeper 5.4m 12 layer soil and 10 subgrid patches were used for the Topmodel simulations to allow a ground water table diagnosis. The wetness indices for these subgrid patches were derived from the 1km USGS GTOPO30 topography dataset. As described above, SiB 2.5 was used with its large-scale standard parameter sets, and the exponential decay parameter for soil hydraulic conductivity, f, was set to $0.5\mathrm{m}^{-1}$. There was no parameter-tuning involved in the experiments (similar to e.g. Baker et al. (2003)), reflecting the model's use in large-scale coupled simulations where no local-scale tuning can be performed.

4.3 Results

4.3.a Monthly runoff and surface fluxes

Rhone catchment

Figure 4.4 displays a comparison between monthly simulated and observed Rhone runoff, plotted over the three years 1986-1988. Monthly precipitation is shown as vertical bars. The seasonal variability in the runoff curve is large, peaking in spring (due to snowmelt from the Alps and spring precipitation) and in autumn (due to increased precipitation in October). Winter and especially the summer show less runoff. There is substantial interannual variability: 1986 had a lot of spring runoff and not much fall runoff. 1987 shows a weaker seasonality but 1988 shows both, substantial spring and fall runoff.

All soil moisture schemes used in the experiments show skill in reproducing the monthly observed runoff. Table 4.2 lists the R^2 values and ratios of modeled/observed runoff for the curves displayed in Figure 4.4. The general picture indicates a substantial increase in correlation from the 3-layer soil scheme (3L) to the multilayer soil scheme (ML), which will be discussed later. The 3-layer soil scheme fails to represent the large seasonal variability, having less snowmelt runoff and overestimated summer baseflow. The modeled/observed runoff ratio matches well with the other experiments.

The use of the aggregated 0.5° and 1° forcing data has a minor effect on the performance of the monthly runoff but at these resolutions the use of Topmodel (MLTOP) creates the most realistic runoff. Furthermore the simulations using Topmodel show skill in simulating the timing and magnitude of spring runoff, which also results in a much more realistic summer baseflow (is underestimated by the ML and overestimated by the 3L experiments). Timing of autumn runoff matches well in the ML and MLTOP experiments,

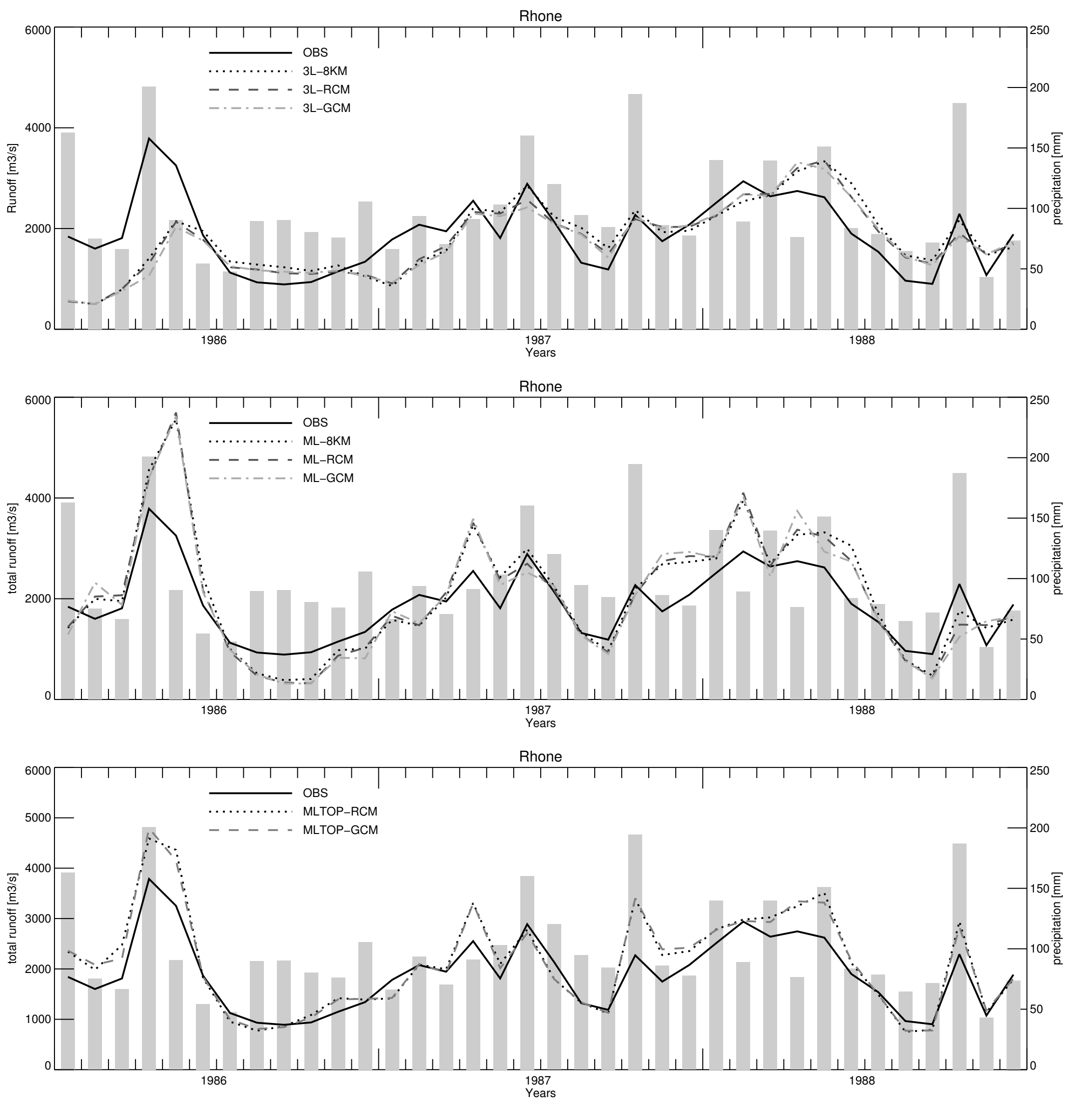

FIG. 4.4: Monthly runoff over the Rhone catchment for January 1986 – December 1988 using the 3-layer (3L), multilayer (ML) and multilayer-Topmodel (MLTOP) soil hydrological parameterizations, forced at different spatial resolutions (8KM, RCM, GCM); monthly precipitation is plotted as gray bars.

but the latter overestimates its magnitude.

TABLE 4.2: Runoff coefficients for the whole Rhone catchment: R^2 (ratio modeled/observed), 1986-1988.

Experiment	8KM	RCM	GCM
3L	0.55 (0.95)	0.57 (0.93)	0.52 (0.91)
ML	0.91 (1.10)	0.89 (1.09)	0.87 (1.07)
MLTOP	-	0.95 (1.12)	0.95 (1.12)

Saone sub-catchment

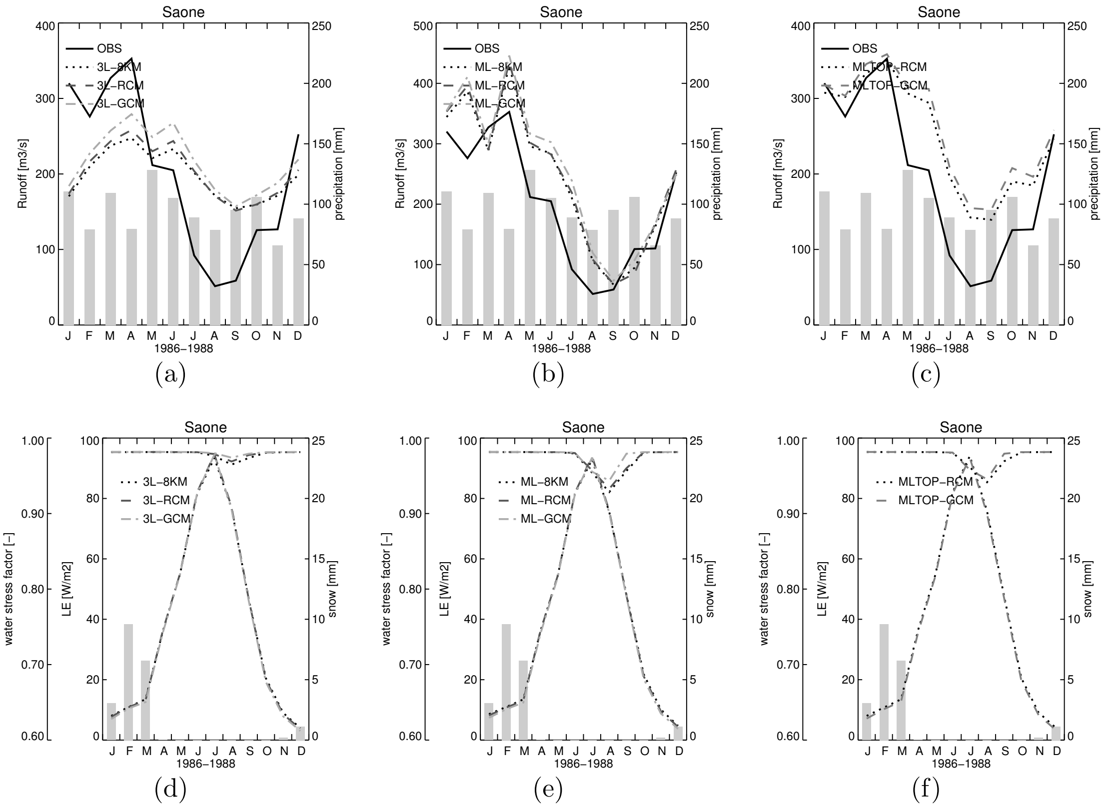

FIG. 4.5: Top: mean monthly runoff (curves) and precipitation (bars); bottom: LE (curves, from bottom), soil water stress factor (curves, from top) and SWE (bars) for the Saone sub-catchment (1986-1988).

Saone runoff shows a similar behavior like the one from the whole catchment since it forms a significant part of the Rhone. As displayed in Table 4.3, the 3-layer scheme achieves the worst match and the use of a multilayer and Topmodel soil moisture parameterization significantly enhances the performance of the monthly runoff, but the runoff ratio (modeled/observed) increases by the use of the latter two parameterizations (which will be discussed later). Runoff skill is furthermore not very scale-dependent for Saone. Figure 4.5 (a)-(c) displays the monthly precipitation and Saone runoff, using the three different soil moisture parameterizations: the seasonal course is well reproduced in all parameterizations except in the 3-layer scheme. The Topmodel experiments (MLTOP-RCM and MLTOP-GCM) perform better in winter but overestimate summer runoff, which can explain their high runoff ratios. They nevertheless have the highest correlation coefficients even at GCM-gridscale, as shown in Table 4.3.

LE fluxes in Figure 4.5 (d)-(f) are neither sensitive to the use of subgrid-scale soil moisture nor to scaling. The water stress factor is a SiB 2.5 model diagnostic and drops to 0 when soil moisture is below wilting point. It is close to 1 for unstressed vegetation. This diagnostic, displayed in Figure 4.5 (d)-(f), shows that soil moisture is not limiting evapotranspiration anytime, so the potential feedback between runoff, soil moisture and plant physiology is low in the Saone. Snow (snow water equivalent [mm], bars in Figure 4.5 (d)-(f)) is not a dominant process here either since its highest catchment-average value is around 10mm in February. As Table 4.3 shows, yearly mean and seasonal surface fluxes for the different parameterizations are all within ±1Wm^2.

Table 4.3: Runoff coefficients R^2, ratio modeled/observed, and seasonal mean LE fluxes for the Saone sub-catchment (1986-1988)

Experiment	runoff [-]		LE [Wm^{-2}]				
	R^2	ratio	DJF	MAM	JJA	SON	YEAR
3L-8KM	0.43	0.99	7.65	34.82	83.88	25.37	37.93
3L-RCM	0.44	1.01	7.41	34.84	84.65	25.02	37.98
3L-GCM	0.44	1.08	6.84	34.32	84.23	24.39	37.45
ML-8KM	0.82	1.22	8.10	34.66	83.31	26.69	38.19
ML-RCM	0.80	1.24	7.78	34.55	83.89	26.21	38.11
ML-GCM	0.77	1.29	7.12	33.89	83.40	25.54	37.49
MLTOP-RCM	0.91	1.25	7.63	34.96	83.99	25.73	38.08
MLTOP-GCM	0.90	1.30	6.91	34.31	83.32	24.94	37.37

Ardeche sub-catchment

Table 4.4: Runoff coefficients R^2, ratio modeled/observed, and seasonal mean LE fluxes for the Ardeche sub-catchment (1986-1988)

Experiment	runoff [-]		LE [Wm^{-2}]				
	R^2	ratio	DJF	MAM	JJA	SON	YEAR
3L-8KM	0.95	0.99	12.61	34.11	82.29	31.07	40.02
3L-RCM	0.91	0.89	12.03	35.18	84.29	31.50	40.75
3L-GCM	0.76	0.59	14.01	41.69	86.82	33.64	44.04
ML-8KM	0.98	1.02	13.10	35.99	84.64	33.26	41.75
ML-RCM	0.94	0.90	12.45	36.75	85.97	33.02	42.05
ML-GCM	0.81	0.64	14.94	45.10	96.74	37.89	48.67
MLTOP-RCM	0.97	0.88	12.09	36.42	84.64	32.07	41.31
MLTOP-GCM	0.98	0.64	14.51	44.70	94.99	36.81	47.75

Ardeche runoff shows a large seasonality, almost ceasing during summer and peaking in spring and autumn. This is a result of the sub-catchments semi-arid climate during summer and of the mainly convective rainfall (Figure 4.6, (a)-(c)). In comparison to the Saone, a smaller improvement in runoff R^2 and almost no change in simulated to observed runoff ratio results from the use of a multilayer or multilayer-Topmodel parameterization (Table 4.4). Figure 4.6 (a)-(c) however shows that a more realistic runoff is simulated in

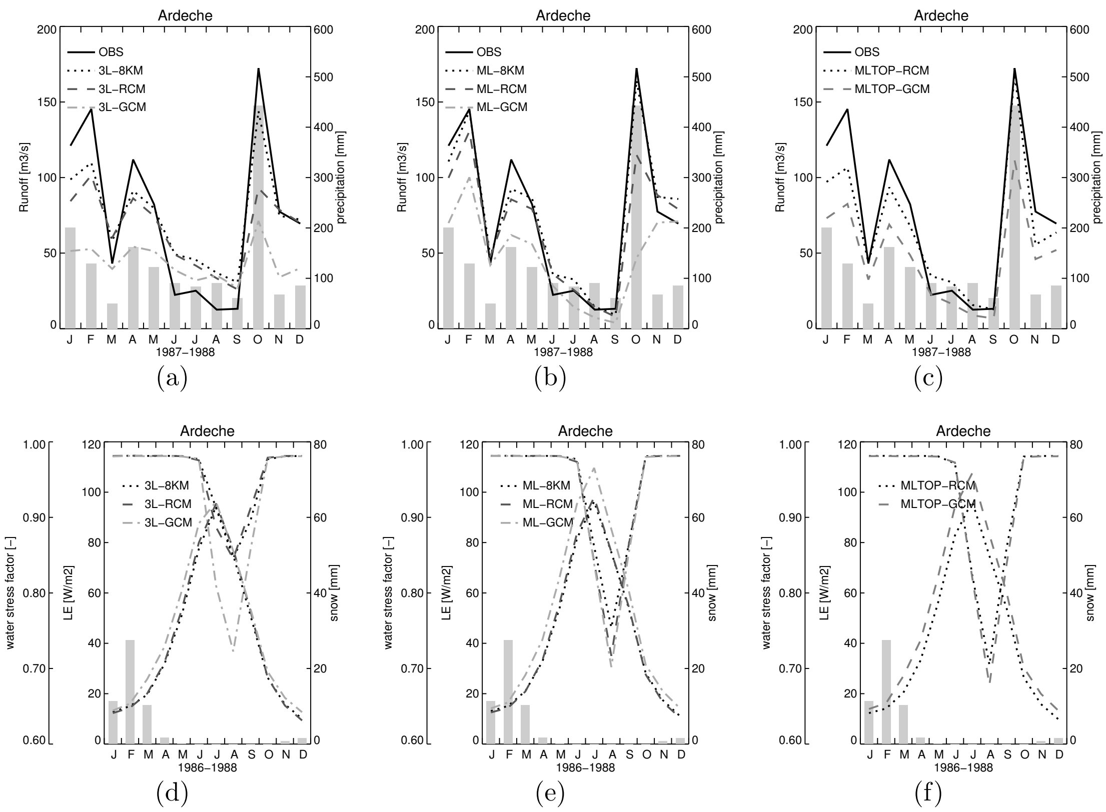

FIG. 4.6: Top: mean monthly runoff (curves) and precipitation (bars); bottom: LE (curves, from bottom), soil water stress factor (curves, from top) and SWE (bars) for the Ardeche sub-catchment (1986-1988).

summer and autumn by the use of these parameterizations. Especially the autumn runoff from convective precipitation matches well in timing and magnitude for the MLTOP simulation at the RCM grid scale, compared to the 3L and ML simulations at the same scale. A substantial decrease in R^2 and runoff ratio occurs when going from the RCM to the GCM resolution but the use of Topmodel (MLTOP-RCM and MLTOP-GCM) partially reverses this trend.

Mean surface fluxes in the Ardeche sub-catchment are sensitive to resolution as is shown in Table 4.4. Generally, higher LE fluxes (by as much as 15%) are observed in the low-resolution simulations. As suggested by Boone et al. (2004) this may largely be a result of the non-linear dependence of biophysical processes to the area-averaged meteorological driver data (mainly precipitation). The seasonal course of LE (Figure 4.6 (d)-(f) and Table 4.4) shows differences between the soil-moisture parameterizations (± 1 Wm^{-2}), but they are small compared to the differences due to upscaling (± 4 Wm^{-2}). The soil water stress factor, however, shows an interesting behavior: The ML and the MLTOP formulation are able to recharge the soil faster in autumn, even though their summer soil water stresses are more pronounced than in the 3L simulations.

Durance sub-catchment

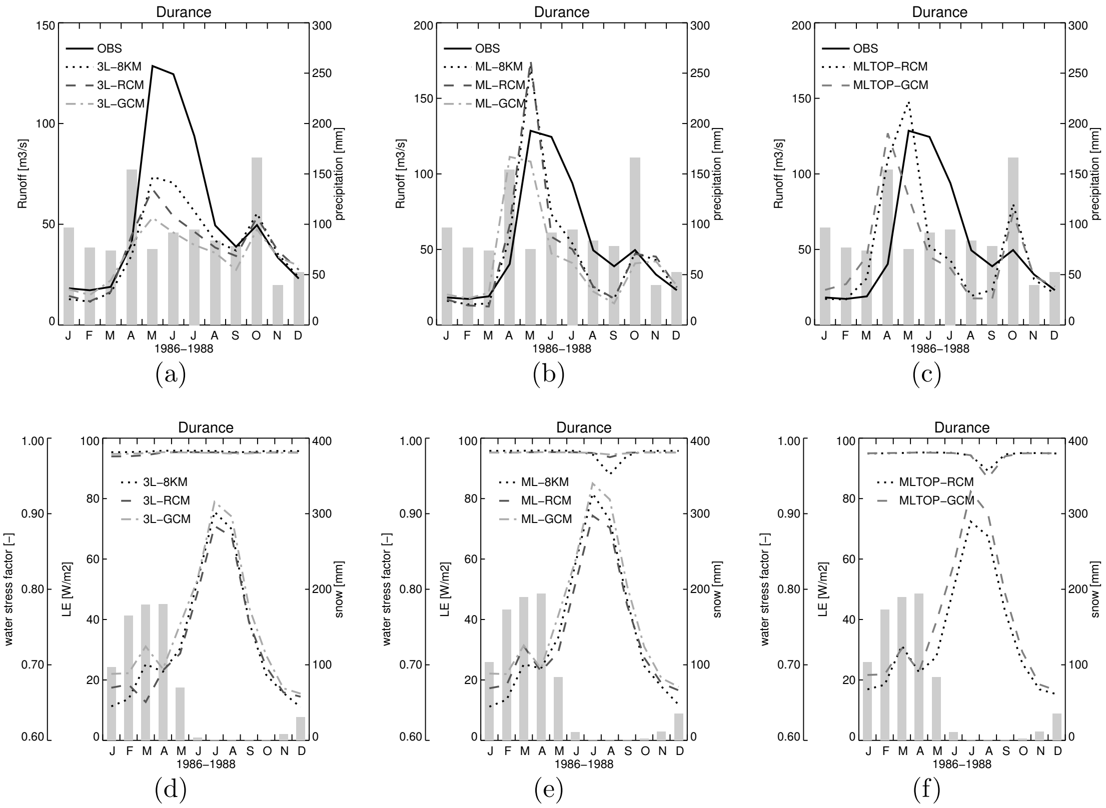

FIG. 4.7: Top: mean monthly runoff (curves) and precipitation (bars); bottom: LE (curves, from bottom), soil water stress factor (curves, from top) and SWE (bars) for the Durance sub-catchment (1986-1988).

The seasonal course of runoff is characterized by a large peak in late spring from Alpine snowmelt as shown in Figure 4.7 (a)-(c), which slowly decreases in summer. Simulated runoff on the monthly time-scale performs better with the ML scheme than with the 3L scheme as shown in Table 4.5. Figure 4.7 (a)-(c) however shows that the 3L scheme is correct in the timing of the snowmelt runoff but underestimates its magnitude. The ML scheme matches the start of snowmelt runoff but overestimates its magnitude, resulting in a depressed summer runoff. As a result of upscaling in the 3L and ML experiments runoff performance gradually decreases similar to the other two sub-catchments.

Including Topmodel results in a similar picture. The runoff skill decreases with lower resolutions. In difference to the 3L and ML experiments, MLTOP shows an early start of the snowmelt runoff and overestimates autumn runoff. The reasons for this result will be explored in the next sections with the help of snow depth measurements. As shown in Figure 4.7 (d)-(f) this catchment has a large SWE during winter (around 200mm in February) but no soil moisture stress is simulated during summer.

TABLE 4.5: Runoff coefficients R^2, ratio modeled/observed, and seasonal mean LE fluxes for the Durance sub-catchment (1986-1988)

Experiment	runoff [-]		LE [Wm^{-2}]				
	R^2	ratio	DJF	MAM	JJA	SON	YEAR
3L-8KM	0.74	0.74	11.96	26.11	66.01	25.61	32.42
3L-RCM	0.58	0.70	16.80	21.53	62.35	26.48	31.79
3L-GCM	0.48	0.64	19.90	31.03	68.65	29.84	37.36
ML-8KM	0.84	0.87	12.13	27.68	71.04	29.69	35.13
ML-RCM	0.78	0.87	17.36	27.73	65.50	30.37	35.24
ML-GCM	0.58	0.81	20.59	32.15	74.77	34.27	40.44
MLTOP-RCM	0.67	0.92	16.85	27.16	63.38	28.33	33.93
MLTOP-GCM	0.37	0.88	20.00	30.79	71.78	32.12	38.67

4.3.b Daily runoff from the Ognon and Ain sub-catchments

Analysis of daily runoff offers further insight into its formation process. In Figure 4.8 observed daily runoff from the Ain sub-catchment is plotted together with modeled values for the year 1986: using a 3-layer soil moisture scheme (a), multilayer soil moisture (b) and multilayer-Topmodel subgrid-scale soil moisture (c). The corresponding R^2 and simulated to observed runoff ratio values for the two sub-catchments Ain and Ognon are displayed in Table 4.6. As seen in the plots, 3L matches the timing of the runoff peaks better than ML, but ML has more skill at reproducing the magnitude of the runoff peaks. Runoff is generally delayed in ML and 3L produces more instantaneous surface excess runoff (spikes in the plot). Runoff ratios are generally lower for the 3L experiments than for ML and MLTOP, which is consistent with the monthly analyses presented before. Lower resolutions (RCM, GCM) have a negative effect on the daily runoff performance in all experiments at both sub-catchments. Also, the R^2 values on the daily time-scale are lower than in the monthly analysis, except when Topmodel is applied. In the MLTOP simulations the R^2 values range between 0.6 and 0.9 where they range between 0.0 and 0.7 for 3L or ML. Plot (c) of Figure 4.8 shows that Topmodel simulations match both the time signature and magnitude of the runoff well.

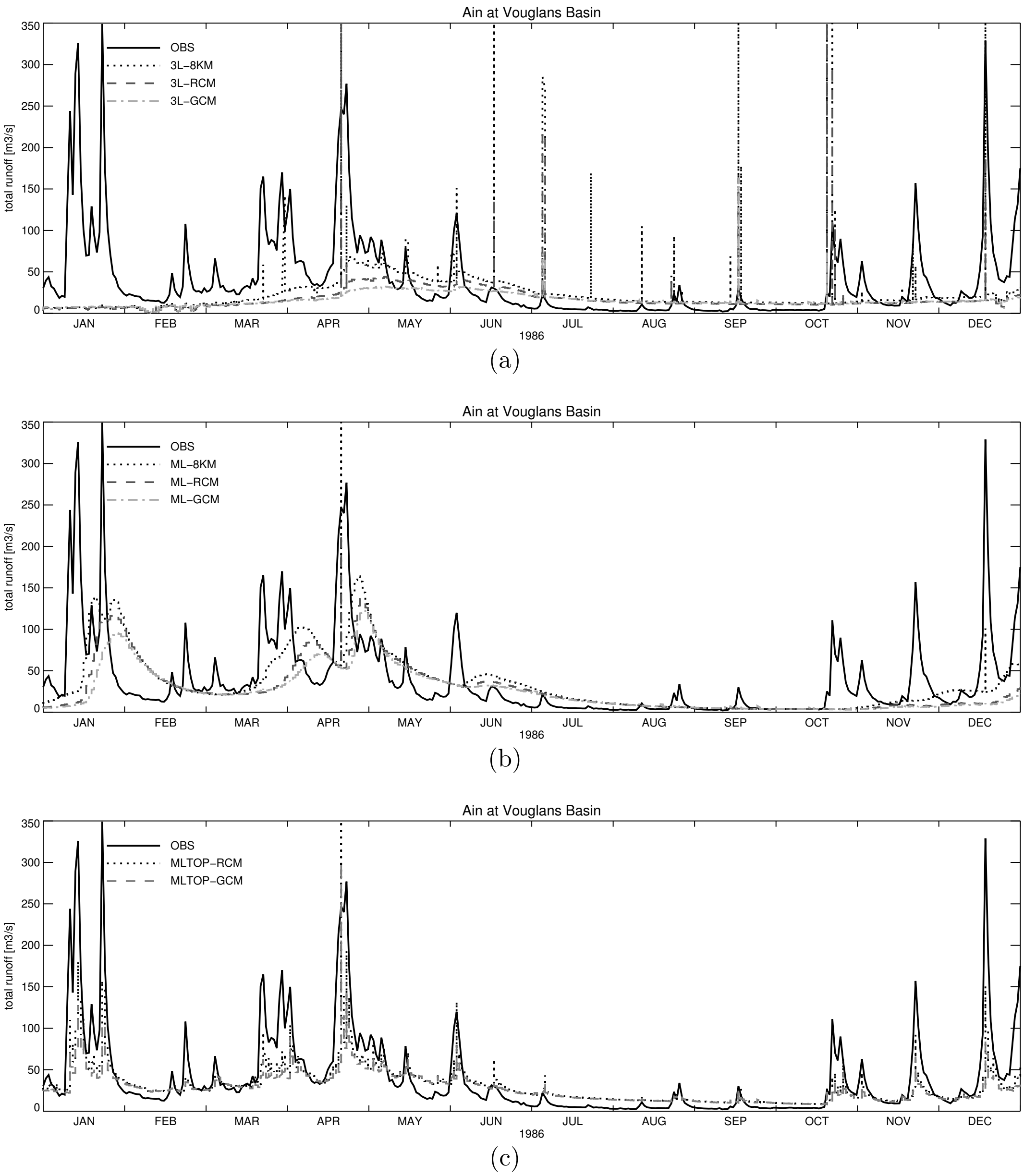

FIG. 4.8: Observed and modeled daily runoff of the Ain sub-catchment: Impact of using a 3-layer (a), multilayer (b) or multilayer-Topmodel (c) soil hydrological parameterization (1986)

TABLE 4.6: Daily runoff coefficients R^2 and ratio modeled/observed for the Ain and Ognon sub-catchments

Experiment	R^2 [-]			ratio [-]		
	1986	1987	1988	1986	1987	1988
			Ain			
3L-8KM	0.13	0.32	0.48	0.57	0.98	0.97
3L-RCM	0.04	0.28	0.46	0.43	0.80	0.82
3L-GCM	0.02	0.21	0.41	0.39	0.66	0.71
ML-8KM	0.39	0.06	0.26	0.88	1.04	0.97
ML-RCM	0.29	0.01	0.20	0.70	0.87	0.81
ML-GCM	0.25	0.03	0.13	0.63	0.74	0.69
MLTOP-RCM	0.68	0.61	0.70	0.78	0.80	0.82
MLTOP-GCM	0.64	0.58	0.63	0.69	0.69	0.71
			Ognon			
3L-8KM	0.37	0.44	0.67	0.70	1.22	1.35
3L-RCM	0.24	0.47	0.68	0.71	1.31	1.37
3L-GCM	0.19	0.51	0.68	0.82	1.38	1.40
ML-8KM	0.55	0.38	0.55	1.23	1.44	1.32
ML-RCM	0.47	0.35	0.49	1.25	1.44	1.35
ML-GCM	0. 41	0.27	0.41	1.27	1.48	1.39
MLTOP-RCM	0.85	0.88	0.88	1.29	1.38	1.37
MLTOP-GCM	0.84	0.87	0.88	1.32	1.40	1.42

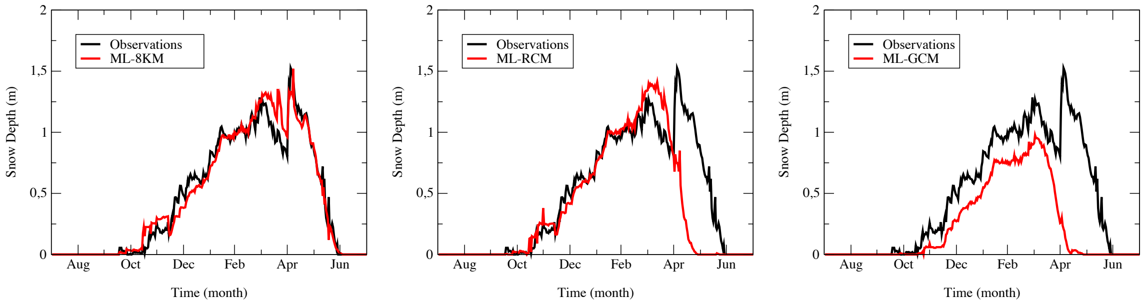

(a) (b) (c)

FIG. 4.9: Snow depth comparison for 24 snow observation sites using a multilayer soil driven at 8KM, RCM and GCM scales (1986-1988)

4.3.c Snow depth comparisons

Results are displayed in Figure 4.9 and statistics of model performances are given in Table 4.7. They show that snow accumulation and melt is heavily scale dependent. The 8KM scale perform best (R^2=0.72), followed by the RCM (R^2=0.42) and GCM (R^2=0.47) scales. The 8KM scale matches very well in timing and magnitude and also shows no bias (mean difference between modeled and measured snow) while the bias grows negatively at the GCM scale. As shown in Figure 4.9 the RCM scale snow accumulation is comparable with the one at the 8KM scale but the snow melt is early by around 1.5 months while at the GCM scale snow accumulation is delayed as well. Snow accumulation and melt does not differ between parameterizations (not shown) but only by the used scale of the driver data which makes the previously presented results of the Durance sub-catchment simpler to interpret: in the 3L, ML and MLTOP experiments, the spring runoff peak stops early at the RCM, but especially at the GCM grid scale.

TABLE 4.7: Model snow depth performance (1986-1988)

Model	RMSD [m]	R^2	bias [m]
ML-8KM	0.34	0.73	0.00
ML-RCM	0.55	0.42	0.03
ML-GCM	0.51	0.47	-0.24

4.3.d Terrestrial water storage analysis

In Figure 4.10 (a) terrestrial water storage (TWS, by (Seneviratne et al., 2004; Hirschi et al., 2006)) changes are compared to ERA-40 derived TWS changes for the Rhone catchment (only the experiments at RCM scale are evaluated in this section). TWS is

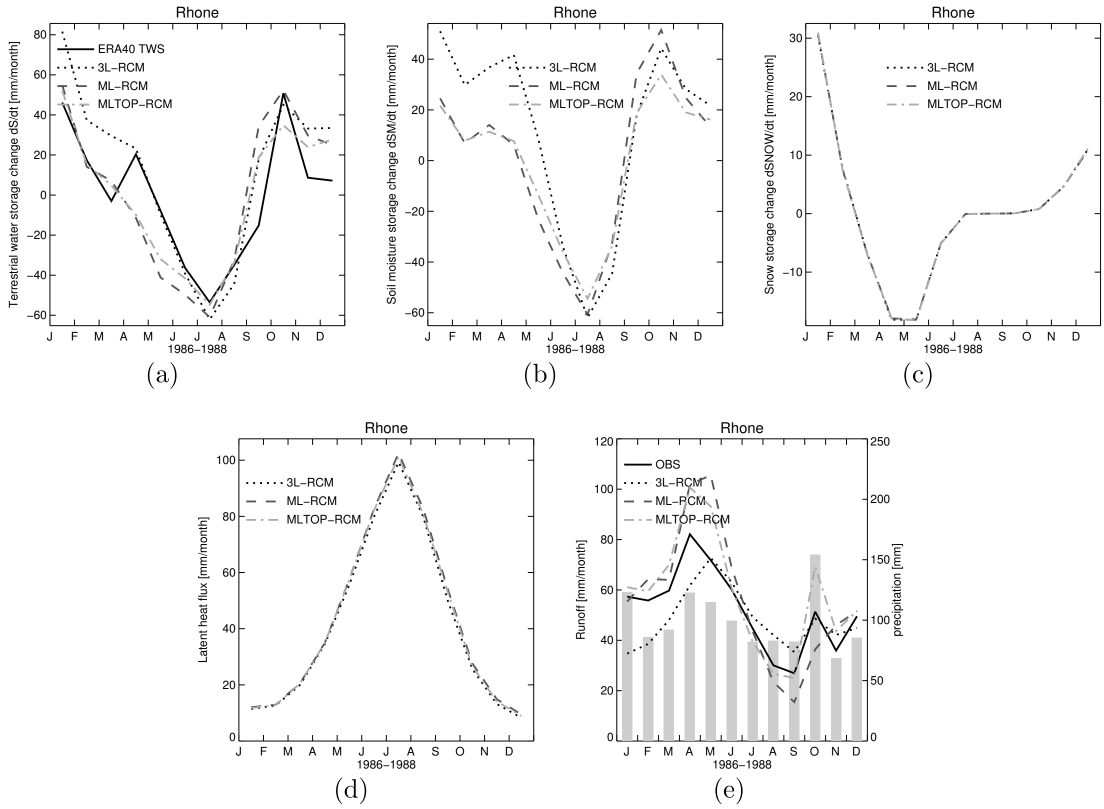

FIG. 4.10: Terrestrial water fluxes and storage components of the Rhone water cycle using a 3-layer, multilayer and a multilayer-Topmodel soil hydrological parameterization: terrestrial water storage change (a), soil moisture storage change (b), snow storage change (c), *LE* flux (d) and runoff and precipitation (e) for 1986-1988

an integrative parameter and allows monitoring the land water cycle on a seasonal to interannual time-scale and helps to further evaluate some of the previous results:

- The 3-layer soil scheme shows a delay in the TWS signal (a) in spring which means that water is accumulated in the soil or as snow for too long in spring, resulting in a delayed runoff (e) with a depressed magnitude.
- All schemes receive the same integrative amount of rainfall (e, bar plot) and it can be seen from plot (c) that snow accumulation and melt are not scheme dependent but rather resolution dependent (reinforces results in the previous sub-section).
- TWS (a) and soil moisture storage (b) differences between the 3-layer and the multilayer scheme are of similar magnitude, which indicates an excessive soil water memory in the 3-layer scheme (In contrast: the bucket model has too little soil moisture memory, see Stöckli and Vidale (2005)).
- Sensitivity of the *LE* fluxes to the used soil moisture parameterizations are small at the catchment scale (d).

- Simulations using Topmodel have a shallower TWS (a) and soil moisture cycle (b) suggesting that soil moisture can be recycled at the catchment-scale by groundwater flow. This finding is discussed in the next section.

4.4 Discussion

The results which were presented separately by sub-catchment will be discussed integratively and linked to evapotranspiration and runoff processes in this section.

The results show that the number of soil layers influences the timing and magnitude of runoff. In Figure 4.12 (a)-(b) the temporal evolution of soil moisture, averaged over the whole Rhone catchment for 1988, is plotted for the 3-layer and the multilayer scheme and helps to explain the differences we see in runoff: the deep soil water in the 3L soil shows much less variability than in the ML soil, but the root zone water shows a higher depression in 3L. Water in the 1.5 m deep root zone (3L) is used for evapotranspiration, and is not available for drainage runoff anymore, since due to the exponential decay of K with decreasing soil moisture, as shown in Figure 4.11, water flux ceases rapidly below field capacity. Therefore evapotranspiration can actively drive runoff. Transpiration on the other hand, is only limited at very low soil moisture levels as shown in Figure 4.11. In ML the root zone is defined through a vertical distribution of root abundance and evapotranspiration only has a limited access to soil water below a certain depth. This results in a faster vertical soil moisture transfer and in a more even distribution of root zone soil moisture. A solid justification for this process is provided by the TWS analysis displayed in Figure 4.10, where 3L shows a higher seasonal magnitude in both, TWS change and soil moisture storage change, compared to the other schemes. The importance of correctly modeling this soil moisture memory in land surface schemes is also proposed e.g. by Koster and Suarez (2001).

Daily runoff plotted in Figure 4.8 supports these findings: although 3L produces a realistic timing in runoff, the high soil storage capacity of the root layer unrealistically decreases the magnitude of runoff. In ML runoff is delayed due to the time needed for infiltration but its magnitude better matches observations. The explanation for this is that vertical root distribution in ML helps to better balance the competing processes of transpiration and drainage after a rainfall event. Water above field capacity drains fast but it can also be transpired by plants. Considering that the majority of plant roots are allocated within the first 0.5m below the surface, much of the drainable water can be removed unrealistically by transpiration in a soil scheme using a 1.5m deep root zone, and drainage ceases rapidly with lower soil moisture values, as already found in the monthly analysis.

During the dry season lateral soil water transfer and runoff ceases like is shown for the Ardeche in Figure 4.6 and all schemes show a substantial decrease in root water availability. Although evapotranspiration is similar for all schemes, the soil moisture limitation factor plotted in Figure 4.6 (d)-(f) shows a high potential for summer droughts in this region. With the end of the dry season the lateral soil moisture transfer could have a feedback on evapotranspiration since the soil moisture recharges fastest in the simula-

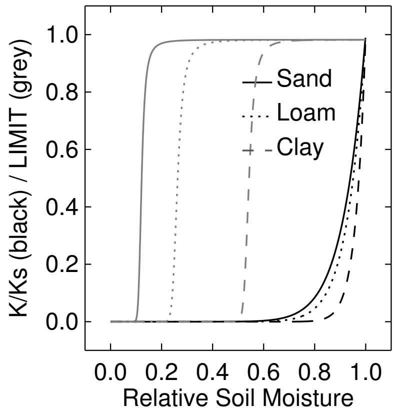

FIG. 4.11: Non-linear dependency of the hydraulic conductivity (black) and the evapotranspiration limitation (grey) on the soil moisture content relative to saturation

tions using Topmodel, despite the fact that the magnitude of its soil moisture limitation is largest. Since the only difference between ML and MLTOP is the subgrid-scale lateral water flux, it has to be the underlying process for this result. After autumn rainfall starts the ground water table is recharged and water is not immediately lost to grid-scale runoff, when Topmodel is used. This process offers an effective means to recover from catchment-scale drought conditions and its validity is supported by the TWS analysis, where Topmodel shows the least magnitude in the seasonal TWS change. This process is of special importance in semi-arid areas with a dry season, where the ground water table follows a substantial seasonal cycle. Subgrid-scale soil water redistribution is a monthly- to seasonal-scale process and can fill the gap between the root soil moisture memory (in the order of 1 month) and the the characteristic time-scale for ground water (in the order of months-years). Only a small part of the Rhone vegetation tends to be soil moisture stressed during summer, so these findings would have to be further explored in a more arid climate. The modeled to observed runoff ratios in the MLTOP simulations deviate more from unity than in the other experiments. Since all the used parameterizations conserve water, this indicates that long-term soil water storage processes play a role in this particular scheme and that 3-year long simulations using such a scheme are not capturing the full temporal scale of these processes.

Daily runoff displayed in Figure 4.8 matches well with observations in both timing and magnitude when Topmodel is used: a rising water table in lowland areas, recharged by lateral water fluxes from higher elevated areas, creates a slow increase in baseflow. Furthermore a fast runoff response is simulated by the use of subgrid-scale topography. If the interplay between topography and the water table is represented in an LSM, a realistic runoff simulation can be achieved even on the daily time scale. Figure 4.12 (c,d) shows the dynamics of the water table in the Durance sub-catchment for the year 1988 when Topmodel is used. The water table is below 3m for high altitude patches with large slopes (c: lowest W), but almost permanently saturated soils (d: highest W) exist in lowland areas.

Snow depth was shown to be sensitive to scaling, which helps to explain Durance runoff. MLTOP creates worse results than ML. Runoff occurs earlier in MLTOP than in ML, but the timing of snow melt is similar early for both experiments (Figure 4.10 (c)). The delay of ML runoff discussed above is enhanced for frozen soils where the hydraulic conductivity is low, and compensates for the early snow-melt in the RCM and the GCM simulations. In Topmodel snow-melt saturates the soil column and creates an instantaneous topography driven runoff in mountainous areas. Snow cover is sensitive to scaling, but snow cover largely drives the seasonal course of runoff in mountainous areas. The solution to this problem would be the use of a subgrid-scale snow parameterization in addition to the use of subgrid-scale soil moisture. As presented in Boone et al. (2004), the one scheme using such an altitude dependent parameterization of snow showed the least impact of scaling on simulated snow depth.

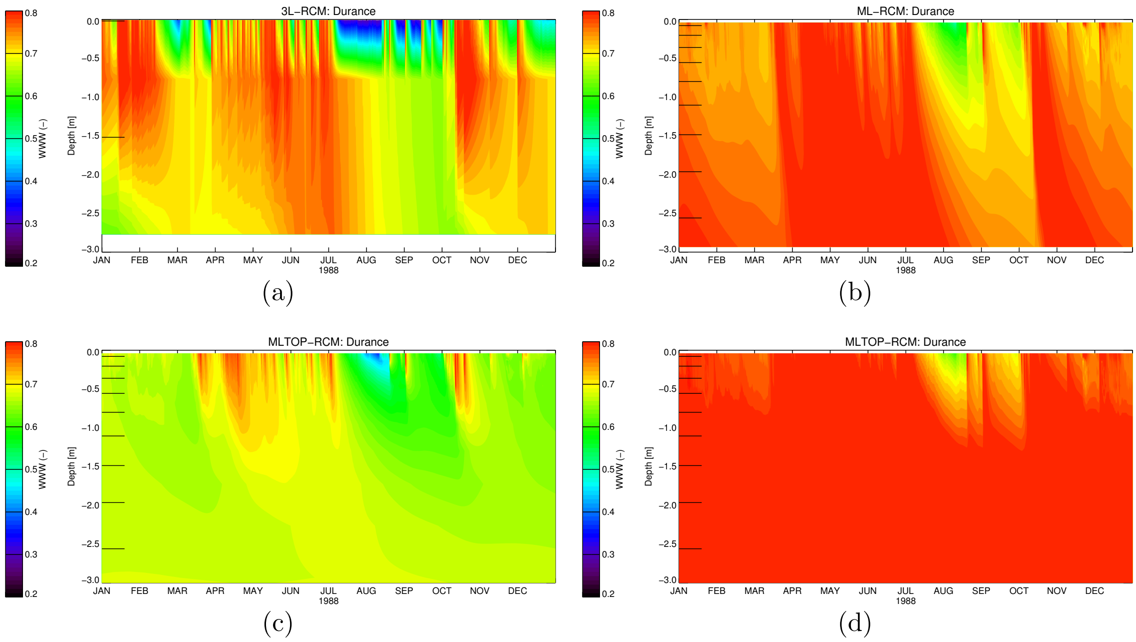

FIG. 4.12: Durance sub-catchment average temporal soil moisture evolution of the 3 layer (a), multilayer (b) and the multilayer-Topmodel (c: lowest W; d: highest W patches) during 1988

4.5 Conclusions

In this study, the influence of using 3-layer, multilayer and Topmodel soil moisture parameterizations in LSMs on evapotranspiration and runoff has been explored, conducting catchment-scale modeling experiments on various spatial scales over the Rhone catchment. Modeled runoff is compared to observed runoff on the daily and monthly time-scale for different sub-catchments covering a wide range of climatic conditions. With the help of snow depth measurements, and terrestrial water storage analysis as two supplementary validation datasets, a process based analysis of evapotranspiration, soil moisture and runoff processes is performed.

The results support the general finding that evapotranspiration and runoff are competing processes for soil moisture and thus the correct representation of both processes is important to model the seasonal water cycle. However, while the chosen soil moisture parameterization has a substantial effect on runoff, evapotranspiration showed very little sensitivity in the Rhone catchment. This result was explained by the very non-linear dependence of K on soil moisture, which results in a sharp decrease of runoff when soil moisture approaches field capacity. Except for very dry conditions, which only happen in the southern part of the Rhone catchment, plant roots can extract water from the soil even at very low soil moisture levels so that primarily runoff but not evapotranspiration is controlled by soil moisture. In the relatively drier Ardeche, vegetation however recovers differently from the dry season depending on the used soil moisture and runoff parameterization and this feedback may be of importance in more arid catchments.

Soil moisture has in the past often been considered as a residual variable in climate modeling, which may partly hold for evapotranspiration. The current findings show that it does not hold for runoff. The use of a subgrid-scale soil moisture scheme in large scale applications allows modeling runoff on the diurnal scale in the Mediterranean and Alpine catchments Ardeche and Durance. Runoff in the rather flat and continental Saone performs well at larger scales without any subgrid-scale parameterization. It was shown that a process-based LSM, using a multilayer hydrological soil coupled to Topmodel can be used in climate modeling to simulate runoff in various climates without the need for parameter adjustments of catchment-scale hydrological processes. Such a framework allows for soil moisture variations on the seasonal (due to groundwater flow), monthly (due to evapotranspiration) and diurnal to weekly (due to drainage on slopes) time-scales.

The following soil scheme dependent conclusions can be summarized:

- the classical 3-layer soil scheme neither accounts for the seasonal nor diurnal dynamics of runoff due to the strong interplay between evapotranspiration and runoff;
- the use of a multilayer soil scheme with a vertical root distribution performs well on the seasonal time scale and is able to represent the magnitude of the daily runoff but not its timing;
- the Topmodel approach holds on the daily scale (slightly overestimating baseflow) because it includes topography driven fast runoff and also the seasonal scale water table dynamics;
- none of the soil moisture parameterizations is able to compensate for the scale-dependency of snow accumulation and melt.

To further explore the latter point, a small experiment may be thought of, where the subgrid-scale soil moisture scheme used in the Topmodel approach also includes a subgrid-scale snow scheme. Since the wetness index distribution within a grid cell has a strong correlation to altitude (except for highland plateaus), the large scale temperature forcing could be scaled adiabatically according to the subgrid altitude distribution.

4.6 Acknowledgements

Funding for this study was provided by the National Centre of Competence in Research on climate variability, predictability, and climate risks (NCCR Climate) funded by the Swiss National Science Foundation (NSF) and by NASA contract NAS5-01070, Task No. 4a, and SSAI subcontract No. 2101-03-002. The support of the ETH Institute for Atmospheric and Climate Science is gratefully acknowledged. We thank Prof. Christoph Schär and Dr. habil. Achim Gurtz for their careful review and useful comments. Thanks to Florence Habets for additional Rhone-AGG data and to Sonia Seneviratne and Martin Hirschi for the ERA-40 derived TWS time-series. Thanks to Scott Denning (CSU) for the permission to use SiB2 and Mapper and to Jim Tucker, Jim Collatz and Sietse Los (NASA/GSFC) for their support on satellite remote sensing and land surface modeling.

Chapter 5

Conclusion and Outlook

5.1 Conclusion

The previous chapters explored seasonal-scale vegetation-atmosphere interactions over Europe with the help of satellite remote sensing, ecosystem measurements and land surface modeling, using a framework presented in the introduction and largely following the theoretical framework by Running et al. (1999) and Turner et al. (2004).

1. In Chapter 2, the influence of seasonal and interannual climate variability on vegetation phenology was shown. For this purpose satellite remote sensing was used to create a 20 year time-series with spatial and temporal dynamics of land surface vegetation phenology, which we call EFAI-$NDVI$, and biophysical land surface parameters were derived for use in LSMs. Using this dataset it was demonstrated, that spring greening varies by more than ± 20 days and is strongly linked to surface winter temperatures and also to the interannual variability of the NAO. Furthermore, for the last 20 years, a trend to earlier springs and later autumn dates is observed, being in the order of around 0.5 days per year. These measurements agree well with ground measured phenological time-series by Menzel (2000) and Defila and Clot (2001), and are consistent with observed global warming (Intergovernmental Panel on Climate Change, 2001) as well as to variations and trends in the atmospheric CO_2 concentrations, as presented in Keeling et al. (1996). We however were unable to link autumn phenological dates to climatic variables. Also, large uncertainties are associated with the phenological trends derived from 20 years of satellite data.

2. To explore the reverse process, namely the seasonal-scale feedback mechanisms from vegetation to the atmosphere, Chapter 3 applied LSMs of different complexity over a wide range of climatic environments and continuous and long-term ecosystem measurements from European FLUXNET sites (Baldocchi et al., 2001). This allowed to characterize relevant soil and vegetation processes. It was found that the time signature of the seasonal heat and water fluxes are largely dependent on the biophysical controls (e.g. in the Mediterranean), biochemical controls (e.g. in central Europe) and the abiotic surface heat balance (e.g. in northern Europe). These results could be related to processes of soil moisture storage, photosynthesis and soil heat storage through direct validation with measured quantities from FLUXNET. It was shown that only the inclusion of all these processes in LSMs allows to correctly represent the seasonal heat and water exchanges at the land surface.

3. Coupled climate simulations, however, use large-scale grids, and Chapter 4 aimed to explore the scale-dependency of land surface hydrological processes. LSMs have been applied at catchment-scale over the Rhone catchment and its sub-catchments, covering a wide range of climatic environments. The Rhone-AGG initiative (Boone et al., 2004) runoff and snow measurements as well as ERA-40 derived terrestrial water storage analysis allow for a process-based validatation of the modeled land surface hydrological cycle at catchment-scale. Results show that runoff is very sensitive to spatial resolution in semi-arid and alpine, but not in continental climates. The use of subgrid-scale soil moisture and lateral water fluxes allows to model catchment-scale runoff at the daily to seasonal time-scale without using a full hydrological model. It however could not compensate for the scale-dependency of snow accumulation and melt in large scale grids. It was shown that runoff is strongly dependent on the used soil moisture parameterization and scale, but that evapotranspiration does not show this sensitivity in the investigated catchments (except to a minor extent in the mediterranean part).

The thesis followed a step-by-step procedure, which was necessary to focus on individual aspects of the land surface heat and water cycle and to guarantee the interpretability of the produced modeling results: satellite remote sensing first showed the influence of climate on vegetation phenology, structure and photosynthetic activity. This technique presented a means to monitor the spatial distribution and temporal evolution of vegetation biophysical properties, and the observed variability strongly justifies to account for such dynamics in land surface schemes used in climate modeling. In climate modeling, satellite remote sensing is an intermediate step between the use of fixed vegetation parameters and of prognostic vegetation properties simulated by DGVMs (Dynamic Global Vegetation Models), which are needed in simulations of the future climates. For these simulations no satellite data exists, and anthropogenic land-use changes are difficult to prognose. The thorough understanding of land surface processes is only possible by the use of mechanistic formulations of the biosphere: having satellite derived biophysical vegetation parameters at hand, they were used as time-varying vegetation parameters in local scale modeling experiments in the second and third part of the thesis, and allowed to concentrate on the land surface - atmosphere feedbacks associated with boundary layer and soil-vegetation-atmosphere exchange processes. Satellite derived vegetation phenology in autumn could for example not be simply linked to temperature or precipitation anomalies in the first part of the thesis. An explanation for this was provided in the second part, where it was demonstrated that soil hydrological, plant biophysical and biochemical processes control soil-vegetation-atmosphere interactions during the summer in southern and central Europe. Although individual processes may govern seasonal-scale land surface - atmosphere feedbacks in distinct climatic environments and for individual months (for instance temperature limitation at the evergreen forest in Norunda, Sweden during January), it was demonstrated, that only the use of a photosynthesis-conductance 3rd generation LSM like SiB 2.5 including monthly or longer soil heat and water storage is able to reproduce the time signature and the magnitude of these interactions on the wide range of climatic environments found over Europe.

The use of a broad range of field measurements from ecology, biology, soil physics and biometeorology was valuable to validate the modeling experiments and to further understand them. While phenological observations allowed to verify satellite derived phenology, eddy-covariance tower flux measurements were used to validate modeled fluxes. Especially the comparison of modeled and measured integrated heat and water fluxes revealed substantial differences between the three applied LSM generations. Differences which could be linked to missing processes and their inclusion in multi-year coupled land surface - atmosphere simulations might show a large impact on the land surface hydrological cycle. Since the local scale did not provide useful information on runoff, the same modeling ideas were used at catchment scale in the last part of the thesis. There it was demonstrated that above-ground biophysics and biochemistry of a 3rd generation LSM was sufficient to get the seasonal LE fluxes and the integrated runoff (and therefore the yearly water balance) right at larger spatial scales (0.5° or 1°), but was not able to resolve the time signature nor the magnitude of the monthly runoff. At such spatial scales, subgrid-scale topography largely defines the grid-average runoff, and the inclusion of subgrid-scale soil moisture processes provided a means to parameterize the diurnal to monthly dynamics of runoff for large scale applications without altering any of the already established above-ground land surface - atmosphere interactions.

The thesis made use of new modeling and measurement techniques and aimed at integrating the manifold tools to a framework that enables to see connections within the land-surface hydrological cycle rather than its empirical or statistical description. Cross-validation between remote sensing, ecological measurements and land surface models helped to gain certainty in modeling land surface processes and their application at larger scales.

5.2 Outlook

My personal research aim is to continue with this integrative modeling framework, since it was successfully applied in this thesis and allowed to extend scientific knowledge in modeling land surface processes at a range of temporal and spatial scales. First, sensors like MODIS (MOderate Resolution Imaging Spectroradiometer) on board NASA's TERRA and AQUA spacecraft now offer a range of state-of-the-art derived land surface products at almost real-time and at a high confidence level. In addition to biophysical parameters used in this thesis, they now allow the direct assessment of carbon-exchange processes like net primary production (NPP, Running et al. (2004)). A forthcoming paper (in preparation) will extend methods used in the second part of the PhD thesis at Fluxnet and Carbomont tower sites to model seasonal heat, water and carbon fluxes. With the availability of MODIS NPP and eddy covariance measurements of NEP (Net Ecosystem Production), satellite remote sensing and tower measurements now offer an excellent cross-validation network for LSMs. However, one of the major tasks in this context is to link the terrestrial carbon sink (assimilation), which can be both, modeled and derived from satellite remote sensing, at large scale, with the terrestrial carbon sources (soil respiration) which depends on soil temperature and soil moisture and on preceeding land use changes, fire occurence and climatic forcings (Randerson et al., 2002). Since especially soil moisture shows such a high spatial variability and also changes to short-term precipitation fluxes and seasonal-scale water table variations as shown in Chapter 3, climate models should treat heterotrophic soil respiration as a subgrid-scale process. Therefore it would be a logical step to further evaluate subgrid-scale soil moisture, snow, runoff and radiation parameterizations for catchment- to regional-scale ecosystem modeling to gain certainty in the modeling of carbon sources and sinks at such scales.

Appendix A

Derivation of biophysical land surface parameters from $NDVI$

The basic relationships between $NDVI$ and the most common land surface parameters are reviewed in this section. Dye and Goward (1993) and Sellers et al. (1996b) show that $FPAR$ has a linear relationship with $NDVI$:

$$FPAR = \frac{NDVI - NDVI_{min}}{NDVI_{max} - NDVI_{min}}(FPAR_{max} - FPAR_{min}) + FPAR_{min} \tag{A.1}$$

where $NDVI_{min}$ is the 2% $NDVI$ value of the $NDVI$ distribution in a land cover class (see Table A.1), $NDVI_{max}$ is the 98% $NDVI$ value of the $NDVI$ distribution in a land cover class (see Table A.1), $FPAR$ is the Fraction of Photosynthetically Active Radiation absorbed by the green leaves of the canopy, $FPAR_{max} = 0.95$, $FPAR_{min} = 0.01$. Los et al. (2000) also use the RVI-$FPAR$ relationship, where RVI (ratio vegetation index, see e.g. Tucker (1979) is the ratio of the NIR and VIS reflectances:

$$RVI = \frac{NIR}{VIS} = \frac{1 + NDVI}{1 - NDVI} \tag{A.2}$$

$$FPAR = \frac{RVI - RVI_{min}}{RVI_{max} - RVI_{min}}(FPAR_{max} - FPAR_{min}) + FPAR_{min} \tag{A.3}$$

where RVI_{min} is the 2% RVI value of the RVI distribution in a land cover class (see Table A.1) and RVI_{max} is the 98% RVI value of the RVI distribution in a land cover class (see Table A.1). In both models the $FPAR$ values are scaled using a linear scaling factor within the observed EFAI-$NDVI$ range for each land cover class. The observed EFAI-$NDVI$ range for each land cover class (2% and 98% values of the $NDVI$ distributions) is documented in Table A.1. The recently published Hansen et al. (2000) 1km global land cover classification is spatially resampled to 0.1° x 0.1° and the 13 UMD land cover classes are translated into the 12 SiB land cover classes. The ice/glacier class is merged from the FAO soil distribution map. Following Los et al. (2000) the average of the two $FPAR$ scaling methods is used. For each grid cell, the vegetation cover fraction (vcf, time invariant) is determined:

$$vcf = \frac{max(FPAR)}{FPAR_{max}} \tag{A.4}$$

Table A.1: DeFries et al. (1998) - SiB land cover reclassification with $NDVI$-$FPAR$ scaling values

Class SiB	Class UMD	Dominant vegetation type	cover [%]	$NDVI_{min}$ [-]	$NDVI_{max}$ [-]	LAI_{max} [m^2m^{-2}]	LAI_s [m^2m^{-2}]	z_2 [m]
0	0	Ocean and Inland water	-	-	-	-	-	-
1	2	Broadleaf-Evergreen Trees[2]	-	-	-	7	0.08	35.0
2	4	Broadleaf-Deciduous Trees	0.4	0.008	0.766	7	0.08	20.0
3	5	Broadleaf and Needleleaf Trees	4.4	-0.015	0.757	7.5	0.08	20.0
4	1	Needleleaf Evergreen Trees	5.3	-0.102	0.742	8	0.08	17.0
5	3	Needleleaf-Deciduous Trees	0.0	-0.039	0.734	8	0.08	17.0
6	6	Broadleaf and Groundcover	7.4	-0.031	0.734	5	0.05	1.0
7	7	Grassland and Shrub Cover	9.3	-0.055	0.718	5	0.05	1.0
8	-	Shrubs and Groundcover[3]	-	-	-	5	0.05	1.0
9	8,9	Broadleaf Shrubs with Bare Soil	13.8	-0.039[1]	0.695[1]	5	0.05	0.5
10	13	Tundra	0.1	-0.023	0.688	5	0.05	0.6
11	12	Bare Soil and Desert	21.3	-0.039[1]	0.695[1]	5	0.05	1.0
12	10,11	Agriculture and Grasslands	24.9	-0.039	0.695	6	0.05	1.0
13	-	Ice[4]	12.9	-0.039[1]	0.695[1]	5	0.01	-

[1] These values were taken from the SiB Grassland class, since $NDVI$ for these vegetation types do not rise to a maximum $FPAR$

[2] There are no broadleaf evergreen trees (tropical rainforest) in the processed European domain

[3] For this SiB land cover class, no appropriate UMD class is found

[4] The Ice class was merged from the FAO Digital Soil Map of the World (FAO, 1995)

LAI_g (leaf area index of the green portion of the canopy) can be derived from $FPAR$ by a logarithmic relationship (Tucker and Sellers, 1986; Baret and Guyot, 1991; Sellers et al., 1996b):

$$LAI_g = \frac{\log\left(1 - \frac{FPAR}{vcf}\right) LAI_{g,max}}{\log\left(1 - FPAR_{max}\right)} vcf \tag{A.5}$$

where $LAI_{g,max}$ is the maximum allowed LAI_g for each land cover class (see Table A.1) and LAI_g is the LAI for the green part of the vegetation. The total leaf area index for a grid cell is then the sum of the green, the stem and the dead LAI (LAI_g, LAI_s, LAI_d):

$$LAI = LAI_g + LAI_s + LAI_d \tag{A.6}$$

where LAI_d is the dead LAI (dead leaves within a grid cell) and LAI_s is the stem area index by land cover class (see Table A.1). When LAI increases during the growing period, LAI_d has a minimum value of 0.0001. As soon as LAI begins to decrease, LAI_d is set to half of the LAI decrease between two time-steps. The canopy greenness $GREEN$ is simply calculated by the time dependent evolution of the total leaf area index:

$$GREEN = \frac{LAI_g}{LAI} \tag{A.7}$$

Studies show that there exists an exponential relationship between the LAI and z_0 (canopy roughness length), which leads to the empirical formulation (also found in Los (1998)):

$$z_0 = z_2(1 - ae^{-bLAI}) \tag{A.8}$$

where z_2 is the canopy height, by vegetation type (see Table A.1), $a = 0.91$ and $b = 0.0075$.

Appendix B

Prognostic canopy air space solutions for land surface exchanges

Prognostic canopy air space solutions for land surface exchanges *

Pier Luigi Vidale † and Reto Stöckli ‡

ABSTRACT

Three generations of land surface models have been developed over the course of the last twenty years, which include increasing levels of complexity. The latest generation incorporates photosynthesis and physiological responses to environmental CO_2, a gas that is strongly controlled by atmospheric vertical stability and by land surface exchanges. A new set of prognostic equations, providing a new solution core for one such land surface model, SiB2, is introduced here. The new equation set makes use of canopy air space variables which are prognostic and allow for the storage of heat, water and carbon at that level, providing both a new memory for the coupled system and a better representation of observed canopy processes. Results from off-line simulation using FLUXNET data from Europe, over a range of environmental and climatic conditions, indicate that the new solution core is able to represent land surface exchanges with equal or better skill than the set it replaces. At the same time, this new formulation provides a simplified mathematical framework, more suitable for further model development.

*accepted for publication in Theoretical and Applied Climatology on 4. August 2004

†Pier Luigi Vidale, Institute for Atmospheric and Climate Science, Winterthurerstrasse 190, 8057 Zürich, Switzerland. e-mail: pier-luigi.vidale@ethz.ch, phone: +41 1 635 5218

‡Reto Stöckli, Institute for Atmospheric and Climate Science, Winterthurerstrasse 190, 8057 Zürich, Switzerland. e-mail: stockli@env.ethz.ch, phone: +41 1 635 5209

TABLE B.1: Typical heat capacities near the land surface [a]

Variable (level)	Volume (m^3/m^2)	Total heat capacity MJ/m^2K
air, atmospheric reference[b]	30	0.03
air, CAS[c]	10	0.01
canopy leaves [d]	0.003	0.002
interception water	0.001	0.004
snow	0.01	0.07
soil	0.02	0.04

[a] values extracted from Sellers et al. (1996d)
[b] first atmospheric model level
[c] Canopy Air Space
[d] with LAI=3

B.1 Introduction

Soil-vegetation-atmosphere transfer schemes have been used for years in atmospheric models in order to describe the surface exchanges of heat, moisture, momentum and carbon. Several different strategies are followed in what concerns the complexity of the included bio-physical processes and the horizontal and vertical distribution of flux sources and pathways, which often depend on scaling criteria and target application. Extensive reviews are provided in Arora (2002), Pielke Sr (2001a) and in Sellers et al. (1997a).

The typical framework of a Land Surface Model (LSM), shown in Figure B.1, involves the ground surface, snow, canopy leaves and reference level atmosphere as prognostic variables. The model framework comprises individual grid boxes, covered by portions of bare ground, vegetation (as a one-layer elevated canopy) and snow, all interacting with the overlying atmosphere through the canopy air space (CAS), which acts as a flux mediator.

The CAS variables are usually solved for as a weighted average of the ground surface, canopy and reference level variables (see for instance Dickinson et al. (1993) and Bonan (1996)). This layer is, therefore, traditionally described in terms of a combination of the individual leaf, soil, snow and reference level variables, so that it has no properties of its own, and fluxes through it are instantaneously adjusted, with no possibility for time delays in the exchanges. This approach was justified in applications in which the thickness of the first atmospheric level (or the height of the probe) was much larger than the typical thickness of the CAS (order of 10m). In more modern models, with increased resolution in the boundary layer (BL) and an explicitly resolved surface layer (SL), with a typical height of 30m, this approach is not completely justified. This can be seen in Table B.1, which shows how the typical heat capacities of each variable in the framework have comparable magnitudes, indicating similar potentials for the storage of heat, water vapor and CO_2.

In the practice of flux calculations from eddy correlation tower data, however, it is recognized that the layer of air below the tower can store individual properties and these storage fluxes are calculated from the vertical divergence of the properties above and below the CAS. From the point of view of observational evidence, the need to consider CAS storage is supported by measurements at several micrometeorological towers (see for

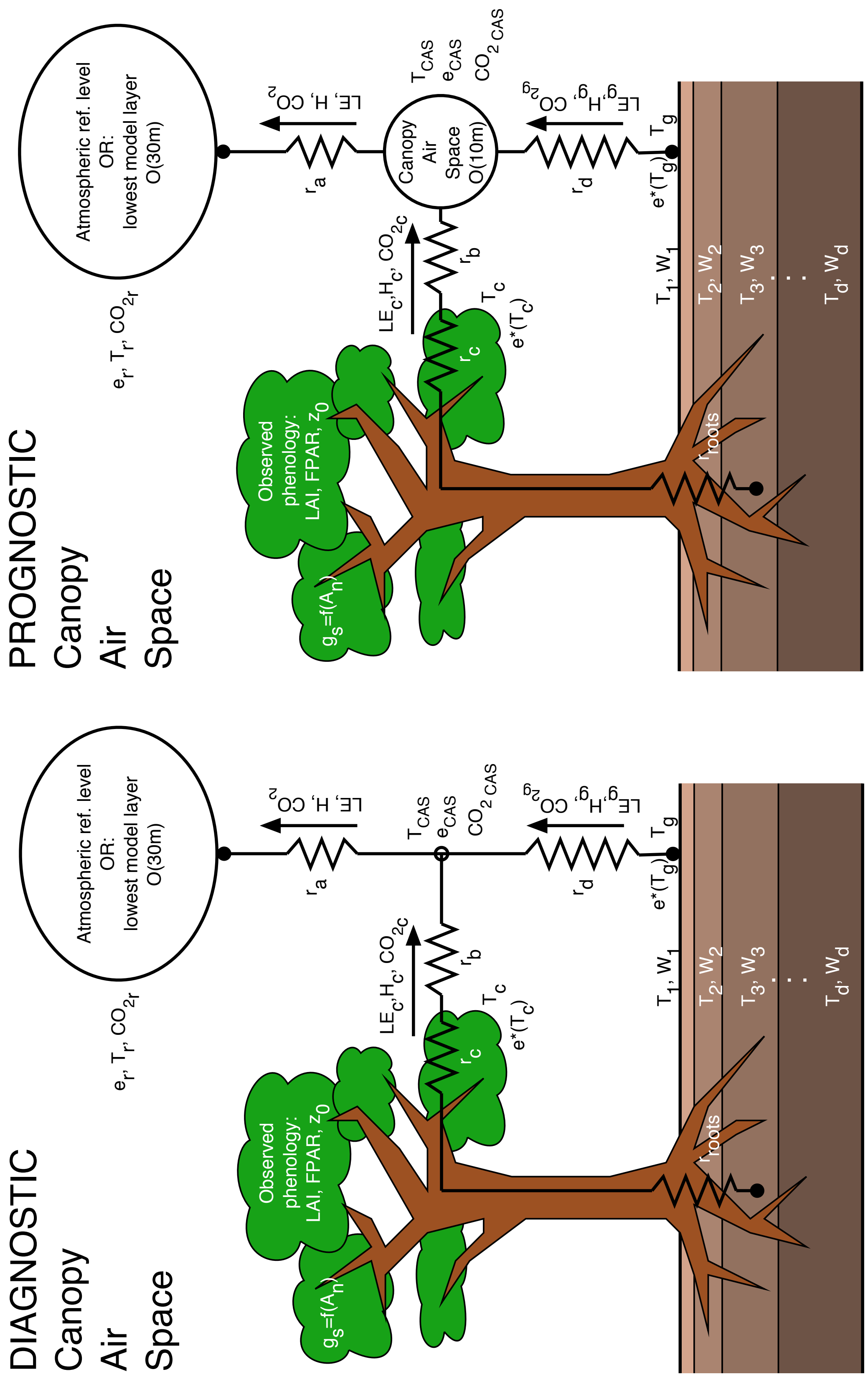

Fig. B.1: The SiB2 land surface model framework: the diagnostic CAS scheme (left) and the new prognostic CAS (right).

instance Schmid et al. (2003) or the FLUXNET data itself, Baldocchi et al. (2001)).

Furthermore, when trying to simulate these fluxes with a LSM coupled to a high resolution (in the vertical) atmospheric model, it is often the case that the model layer above the reference level has a thickness of the same order of magnitude as that of the CAS itself, in which case it would seem necessary to treat the CAS air as a finite vertical layer and not an infinitesimally thin one. Given the observational evidence and new modeling requirements we propose to introduce a CAS layer in a LSM framework in order to test the feasibility of such an approach and its degree of physicality.

The implementation presented here introduces, in correspondence to these storage capacities and associated fluxes, new prognostic variables for the CAS, similar to what was done by Walko et al. (2000), which result in three new prognostic equations. The SiB2 LSM (Sellers et al. (1996d)) has been extensively used in off-line and on-line mode over a wide range of spatial and temporal ranges, examples of which are given in Kim et al. (2001), Randall et al. (1996), Denning et al. (2003). It represents therefore an ideal test bed for this type of new prognostic approach.

The goal of this work is to document the new solution core that was implemented in the model (referred to as SiB2.5) and successfully used by Baker et al. (2003), Denning et al. (2003), and Stöckli and Vidale (2005). The existing solution set is thus initially discussed and the new prognostic core is introduced thereafter, together with some examples of off-line applications. Discretized versions of the prognostic equations, useful for numerical implementation, are presented in Appendix B.7.

B.2 Prognostic equations at the land surface in SiB2

The governing prognostic equations for the land surface variables, i.e., the heat and water of the ground-snow surface (suffix g) and canopy leaves (suffix c), were introduced in Sellers et al. (1996d) and the temperature relationships are summarized here for reference:

$$\begin{aligned} c_g \frac{\partial T_g}{\partial t} &= R_{n_g} - H_g - E_g - G \\ c_c \frac{\partial T_c}{\partial t} &= R_{n_c} - H_c - E_c \end{aligned} \tag{B.1}$$

where $T_{c,g}$ are the temperatures of the canopy leaves and snow-ground (K); $c_{g,c}$ are the effective heat capacities (J m^{-2} K^{-1}); R, H, E and G are the net radiation, sensible heat flux, latent heat flux and ground heat flux (W m^{-2}).

In that modeling system the canopy air space (CAS) acts as an instantaneous mediator between individual flux network components, and all fluxes through the CAS are additive, equaling the fluxes between CAS and the atmospheric reference level, as is explained in the next sub-section.

B.2.a Canopy air space (CAS) variables and their diagnostic treatment.

Referring again to Figure B.1 (left panel), the canopy air space is the portion of the surface layer which is in direct contact with the canopy leaves and which mediates the turbulent exchanges between leaves, bare ground, snow and the atmospheric reference level above.

In reference to the framework of the SiB2 model, in which the present solutions have been implemented, it is the distance between heights z_2 and z_1 (canopy top and canopy base) in Figure 1 of Sellers et al. (1996d).

In this context, the CAS has a storage capacity equivalent to the mass per square meter in the layer that comprises the vegetation canopy. In the original model of Sellers et al. (1996d), this quantity was considered infinitesimally small, so that the definition for CAS variables in SiB 2.0 are:

$$\begin{aligned}
T_a &= \frac{\frac{T_r}{r_a} + \frac{T_c}{r_b} + \frac{T_g}{r_d}}{\frac{1}{r_a} + \frac{1}{r_b} + \frac{1}{r_d}}; \\
e_a &= \frac{\frac{e_r}{r_a} + \frac{e_c}{r_c+2r_b} + \frac{e_g}{r_d}}{\frac{1}{r_a} + \frac{1}{r_c+2r_b} + \frac{1}{r_d}}; \\
CO_{2_a} &= \frac{\frac{CO_{2m}}{r_a} + \frac{CO_{2c}}{1.6r_c+2.8r_b} + \frac{CO_{2g}}{r_d}}{\frac{1}{r_a} + \frac{1}{1.6r_c+2.8r_b} + \frac{1}{r_d}}
\end{aligned} \tag{B.2}$$

where $T_{c,g,a,r}$ are the temperatures of the canopy leaves, snow-ground, CAS and reference level (K); $e_{c,g,a,r}$ are the vapor pressures (Pa); $CO_{2_{c,g,a,r}}$ are the CO_2 partial pressures (Pa); r_a, r_b, r_c, r_d are the resistances (sm^{-1}).

Scalar fluxes through the CAS are correspondingly additive and instantaneously adjusted, equaling therefore fluxes between CAS and atmospheric reference level:

$$\begin{aligned}
H_a &= H_c + H_g; \\
E_a &= E_c + E_g = E_{ci} + E_{ct} + E_{gi} + E_{gs}; \\
F_{CO_{2_a}} &= F_{CO_{2_c}} + F_{CO_{2_g}}
\end{aligned} \tag{B.3}$$

where $H_{c,g,a}$ are the sensible heat fluxes from canopy leaves, snow-ground and CAS (Wm^{-2}); $E_{c,g,a}$ are the latent heat fluxes from canopy leaves, snow-ground and CAS (Wm^{-2}); $F_{CO_{2_{c,g,a}}}$ are the carbon fluxes from canopy leaves, snow-ground and CAS (μmol $\mathrm{m}^{-2}\mathrm{s}^{-1}$). The subscripts i, t, s refer to water vapor originating from interception, transpiration and surface soil pore reservoirs, respectively.

A limitation of the standard implementation, using the classic weighted average approach to the calculation of the CAS capacity, is that it introduces dependencies on all prognostic variables when the partial derivatives are calculated, making the calculations cumbersome and preventing the use of the variables in some of the equations (most notably in the calculations of the r_b and r_d aerodynamic exchange coefficients, see Sellers et al. (1996d), Equations 10 and 11).

For example, in the case of the canopy leaves heat flux, H_c, Sato et al. (1989b), Sato et al. (1989a) and Sellers et al. (1996d) use a definition of the CAS temperature similar to that in other LSM (e.g. BATS), as was shown in Equation B.3. Because of this definition, the numerous flux cross-derivative terms used in the solution implementation (see Appendix B.7), for instance $\frac{\partial H_x}{\partial T_x}$, will contain terms involving all three boundary temperatures, that is the ground, leaves and reference air temperatures.

An example of the extensive and inconvenient flux derivative formulation resulting from this approach in the case of terms involving the heat flux from the canopy leaves, H_c:

$$H_c = \rho c_p \frac{(T_c - T_a)}{r_b}$$

so that:

$$\frac{\partial H_c}{\partial T_c} = \rho \frac{c_p}{r_b}\left(1 - \left[\frac{\frac{1}{r_b}}{\frac{1}{r_a} + \frac{1}{r_b} + \frac{1}{r_d}}\right]\right), \tag{B.4}$$

where ρ is the density (kg m^{-3}) and c_p is the heat capacity of air (J kg^{-1}K^{-1}), because of the definitions in Equations B.3 and B.4.

This approach was fully justified in applications for which the height of the reference level was much larger than the vertical extent of the canopy air space or in coupled systems in which only a bulk mixed layer (and no surface layer) are simulated (such as in the CSU GCM). If the vertical extent of the CAS and the distance to the reference level are of the same order of magnitude, however, a different treatment should be considered, since the capacities of the canopy air space and of the first atmospheric level in the host model are of similar magnitude.

B.2.b Canopy air space variables and their prognostic treatment: the new solution core.

More modern applications, off-line or coupled, assume that the atmospheric reference state is located much nearer to the surface, so that the heat (moisture, scalar) capacity of the layer of air that it represents is of the same order of magnitude as that of the canopy air space (CAS), that is, the amount of air contained within the (interacting directly with) canopy leaves. It is assumed here that the CAS spans the region between canopy base and top; an idealized picture of this new framework is shown in Figure B.1 b.

With both physical and numerical reasons in mind, CAS capacities and variables are proposed, together with corresponding prognostic equations at that vertical level, as was also done previously in Walko et al. (2000) for a simpler LSM. Two new prognostic equations for CAS temperature and moisture are thus added to the set in Equation B.1:

$$\begin{aligned} c_a \frac{\partial T_a}{\partial t} &= -H_a + H_c + H_g \\ c_a \frac{\partial e_a}{\partial t} &= -E_a + E_c + E_g \\ c_a \frac{\partial CO_{2_a}}{\partial t} &= -F_{CO_{2_a}} + F_{CO_{2_c}} + F_{CO_{2_g}} \end{aligned} \tag{B.5}$$

where c_a is the storage capacity of the CAS in J m^{-2} K^{-1} (for water this is expressed in units of J m^{-2} Pa^{-1}, and for CO_2 in units of μmol m^{-2}Pa^{-1}). The introduction of these new prognostic variables, T_a, e_a and CO_{2_a} makes it possible to define new fluxes originating at the CAS level:

$$\begin{aligned} H_a &= \rho c_p \frac{(T_a - T_r)}{r_a} \\ E_a &= \frac{\rho c_p}{\gamma} \frac{(e_a - e_r)}{r_a} \\ F_{CO_{2_a}} &= \kappa \frac{(CO_{2_a} - CO_{2_r})}{r_a} \end{aligned} \tag{B.6}$$

where γ is the psychrometric constant (Pa K $^{-1}$) and κ a unit conversion (μmol Pa^{-1}m^{-3}). These expressions smoothly reduce to the diagnostic expressions for the case of zero CAS thickness (e.g. for grasslands, although the canopy-reference level distance would also be much smaller in such a case), as, for instance:

$$\lim_{c_a \to 0} c_a \frac{\partial T_a}{\partial t} = 0 \Longrightarrow H_a = H_c + H_g \tag{B.7}$$

therefore:

$$T_a = T_r + r_a \frac{(H_c + H_g)}{\rho c_p} \tag{B.8}$$

which goes back exactly to the diagnostic expressions in (2). The same applies to e_a and CO_{2_a}.

These new definitions also greatly simplify the expressions for the partial derivative terms, eliminating the need to carry cross-derivative terms, for instance, in contrast to (4):

$$\frac{\partial H_c}{\partial T_c} = \frac{\rho c_p}{r_b} \tag{B.9}$$

because only the foliage and CAS temperatures are involved as independent variables. The same simplifications apply to all other cross-derivative terms and permits the overall elimination of 20 partial derivative terms which are programmed in different parts of the numerical implementation.

The new equation set that is formed by adding these three prognostic equations to the set in Equation B.1 and by altering the definitions of the individual fluxes comprises the new SiB2 solution core, which we be call SiB2.5 thereafter. The discretization and solutions to the new core equation system are shown in Appendix B.7.

B.3 Off-line simulations with diagnostic and prognostic solutions

The two model versions, 2.0 (diagnostic CAS) and 2.5 (prognostic CAS) have been run off-line for all Fluxnet sites for years between 1996 and 1999. The individual simulations were driven by meteorological data, with an update frequency of 30 minutes and were spun up for 5 years prior to the actual integration. Initial and boundary conditions (especially time-dependent ones) were pre-calculated with a SiB2 accessory tool, Mapper, in the same way as described in Sellers et al. (1996b), using the EFAI data sets of Stöckli and Vidale (2004). The reference level CO_{2_r} was fixed at 37.5 Pa, since it is not possible in off-line mode to simulate the boundary layer oscillation of CO_2 concentrations and it was deemed safer, at this stage, to keep this extra degree of freedom from influencing our assessment of the new model performance. The time step for the integrations is 10 minutes for both formulations. All integrations were continued for the period of availability of tower forcing data, which varies by site, but is always comprising of at least one full year of data. In this study we will provide examples from the Tharandt (Germany) site, while in the companion Stöckli and Vidale (2005) we provide a much wider range of applications at different European sites. The Tharandt Fluxnet tower measures micrometeorological variables and radiation, heat, water and carbon fluxes in a coniferous forest (mean LAI of 6.0) and is located in Germany (50°58'N 13°38'E). The site has a mean annual temperature of 7.5°C and receives 824mm of rain (climatological mean). Continuous measurements of surface fluxes and plant and soil biophysical data since 1996 provide a high quality time-series which is very useful for ecosystem modeling. We have used data of the year 1998, which are publicly available through the Fluxnet database (http://www-eosdis.ornl.gov/FLUXNET/). Data gap filling issues are discussed in Stöckli and Vidale (2005).

B.4 Discussion.

The novelty of this approach consists in the use of the storage capacities for the CAS variables, which allows for the 'memory' of the system, similar to what is done in the calculation of eddy correlation fluxes under a tower. This is particularly important at times of transition between a stable and an unstable surface layer, when differences arise in the two treatments due to the existence of storage fluxes within the CAS.

The strong simplifications in the calculation of the cross-coupling terms has also allowed for a more streamlined discretization of the prognostic equations, for the numerical implementation, than in the previous framework. One of the practical consequences is the inclusion of fully implicit long wave radiative terms in the net radiation components, which within this framework requires minimal effort and is physically justified. As discussed in Bonan (1996), however, this extra increment term is usually smaller than the other forcings, although it can become comparatively important at particular times of the diurnal cycle. The details of this implementation are available in the Appendix B.7.

The analysis of the comparative performance of the two models focuses on the production of prognostic variables and on the fluxes originating in the CAS. Much more substantial validation and testing, focusing on heat and water fluxes over different Fluxnet sites has been performed in a companion paper, also in this issue (see Stöckli and Vidale (2005)).

B.4.a Simulation of the yearly and diurnal cycle of canopy temperatures

The canopy leaves temperature T_c is a primary prognostic variable in SiB2 and the evolution of an average diurnal cycle in July 1998 is shown in Figure B.2 (a) for the Fluxnet site Tharandt; a complementary evolution is shown for the 1998 yearly temperature cycle in Figure B.2 (b). Comparisons with available observations shows that both model versions simulate the yearly cycle of temperature in a fairly accurate way, so that to the

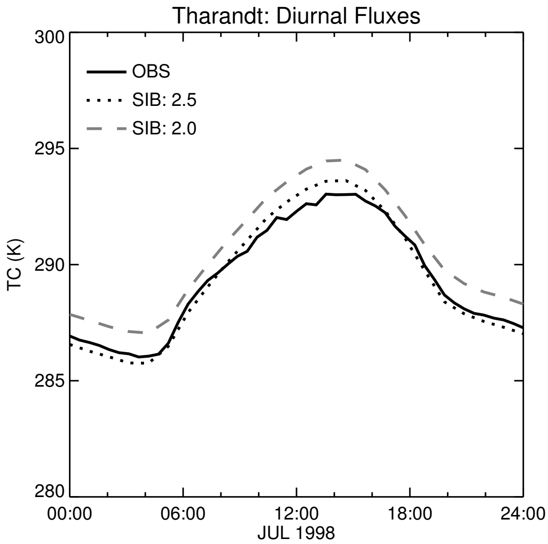

FIG. B.2: Prognostic (SiB2.0 and SiB2.5) of canopy leaves temperature T_c (K) at Tharandt, 1998: average diurnal cycle (left) in July and yearly time series (right). Observations at the site are also shown for reference.

first order both solutions are shown to be compatible. This was also true of other sites and prognostic variables (not shown). The diurnal plots show that the July mean diurnal cycle is better simulated by SiB2.5, since SiB2.0 tends to be consistently too warm. For the yearly cycle, SiB2.0, however, provided a better simulation of winter time temperatures, but is too warm by about 2K over the summer. SiB2.5, on the other hand, tends to be cold in winter (2-3 K), but simulates the summer temperatures accurately. This is important for biophysical feedbacks involving physiological responses: in SiB2.0 the summer vegetation tends to become temperature-stressed near noon, an event which is less frequent in SiB2.5 simulations. An explanation for the winter-time temperature evolution in SiB2.5 is connected with both the extra stratification, provided by the new CAS layer, and with the more extreme r_a and r_d values, which can now be produced by the use of the prognostic T_a variable in the definition of the aerodynamic resistances. Other effects derive from storage fluxes, which are explored in the following subsection.

B.4.b Simulation of CAS storage fluxes

Canopy storage fluxes are only available at a few sites in the Fluxnet dataset; we use the data from Tharandt as an example. Figure B.3 shows the storage latent and sensible heat fluxes at this site, as an average diurnal cycle for the entire year of 1998 (left panel). The data for July show that the SiB2.5 model is simulating the heat and moisture storage fluxes in the CAS in both magnitude (order of 10 Wm^{-2}) and phase. The right hand panel figures show the corresponding fluxes for the average diurnal cycle in the month of July 1998. The CAS is therefore a sink of heat in the early part of the day, and a source near sunset; for moisture, however, the CAS appears to function as a sink near both sunrise an sunset, in agreement with measured data. At these times CAS storage fluxes are at a maximum and time lags of up to 30 minutes appear in the surface soil/vegetation/atmosphere network:

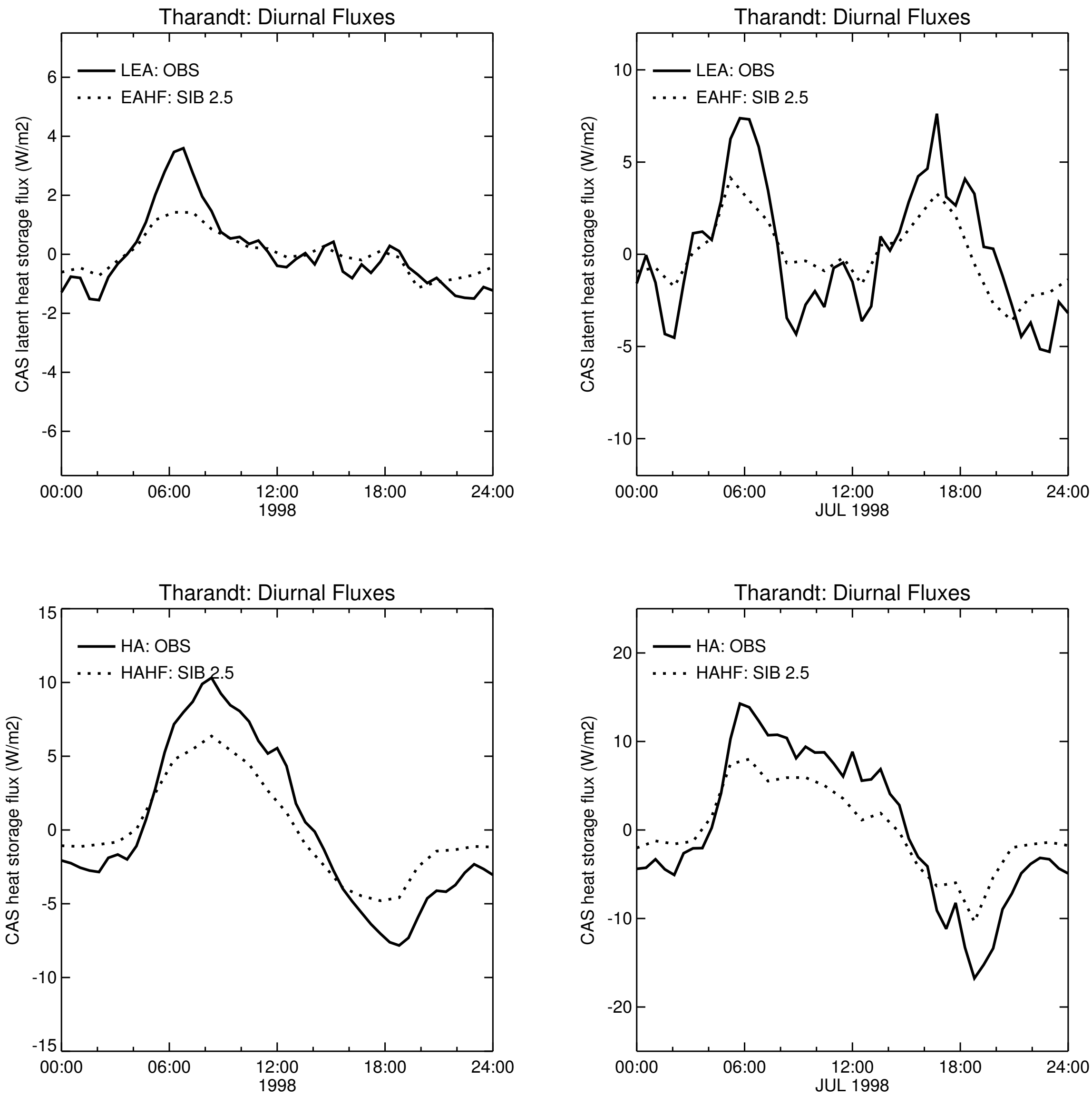

Fig. B.3: The SiB2.5 CAS water (top) and heat (bottom) storage fluxes (Wm^{-2}) for an average day in the year 1998 (left panels) and for an average day in July (right panels), Tharandt site. Measured values shown for reference.

therefore storage fluxes will introduce a lag in the fluxes originating at the CAS. The same interpretation is valid for the seasonal cycle (not shown), in which periods of larger stability (and large values of aerodynamic resistances) will coincide with more storage and flux lag, while periods of lower stability will see less storage, through diminished control imposed by the resistance network. The effects of these storage fluxes should become mostly evident in the CO_{2_a} evolution (see Fig ure B.4), which is controlled by two sources, one at the surface and one at the reference level, while being depleted by a single sink, at the canopy level.

B.4.c *Simulations of yearly and diurnal cycles of CAS CO_2 partial pressures*

As explained before, simulations were performed using a fixed reference level CO_2 partial pressure (37.5 Pa), which damps the diurnal cycle of CO_2, since no BL oscillation of CO_2 is fed to the model through the boundary data. The plots in figure B.4 show the yearly cycle on the x axis and the diurnal cycle on the y axis. The middle figure shows the observed CO_2 at the reference level at Tharandt for 1998 for comparison, while the other two panels show the partial pressures predicted by SiB2.0 and SiB2.5. The CO_2 at the reference level is not expected to be depressed by assimilation as much as in the CAS during times of poor vertical mixing; it should not, however, display higher level of CO_2 than found in the CAS during periods of high stability. The model reproduces reasonably well the yearly and diurnal cycles of CO_2, which is high during the winter and night (high vertical stability and no assimilation) and low during the summer and at daytime (mixed SL and assimilation is active). The different solutions in SiB2 and SiB2.5 are most evident near times of stable stratification in the surface layer (that is, night time or winter), when storage and reduced transfer between the reference level and the land surface components allow the CAS to accumulate CO_2. In general SiB2.5 is able to represent the winter and nighttime accumulation of CO_2 near the surface much better than SiB2.0. The feedback effect deriving from the synergy of stability and source/sink activity has been denominated "rectifier effect" in Denning et al. (1996), but cannot be fully investigated here because of our off-line methodology. The characteristic of the new prognostic model, the lag introduced by the CAS capacities seem to be consistent with the effect of storage fluxes.

B.4.d *Simulations of yearly and diurnal cycles of CAS CO_2 storage fluxes*

An example of the yearly and diurnal cycles of CO_2 storage fluxes produced in SiB2.5 is given in Figure B.5, which shows how the CAS is acting as a CO_2 sink in the early hours of each day and as a source near sunset over an extended yearly cycle, from April until October. The magnitude of the fluxes, about 1 μ mol m$^{-2}s^{-1}$, is about one order of magnitude less than the typical peak CO_2 flux (+5 at nighttime to -20 μ mol m$^{-2}s^{-1}$ during daytime), but quite relevant near the times of reversal of vertical stability, at sunset and sunrise. The "signature" of these fluxes appears therefore to be in agreement with theory and, by looking at the induced CO_2 partial pressures in the previous sections, also with observations.

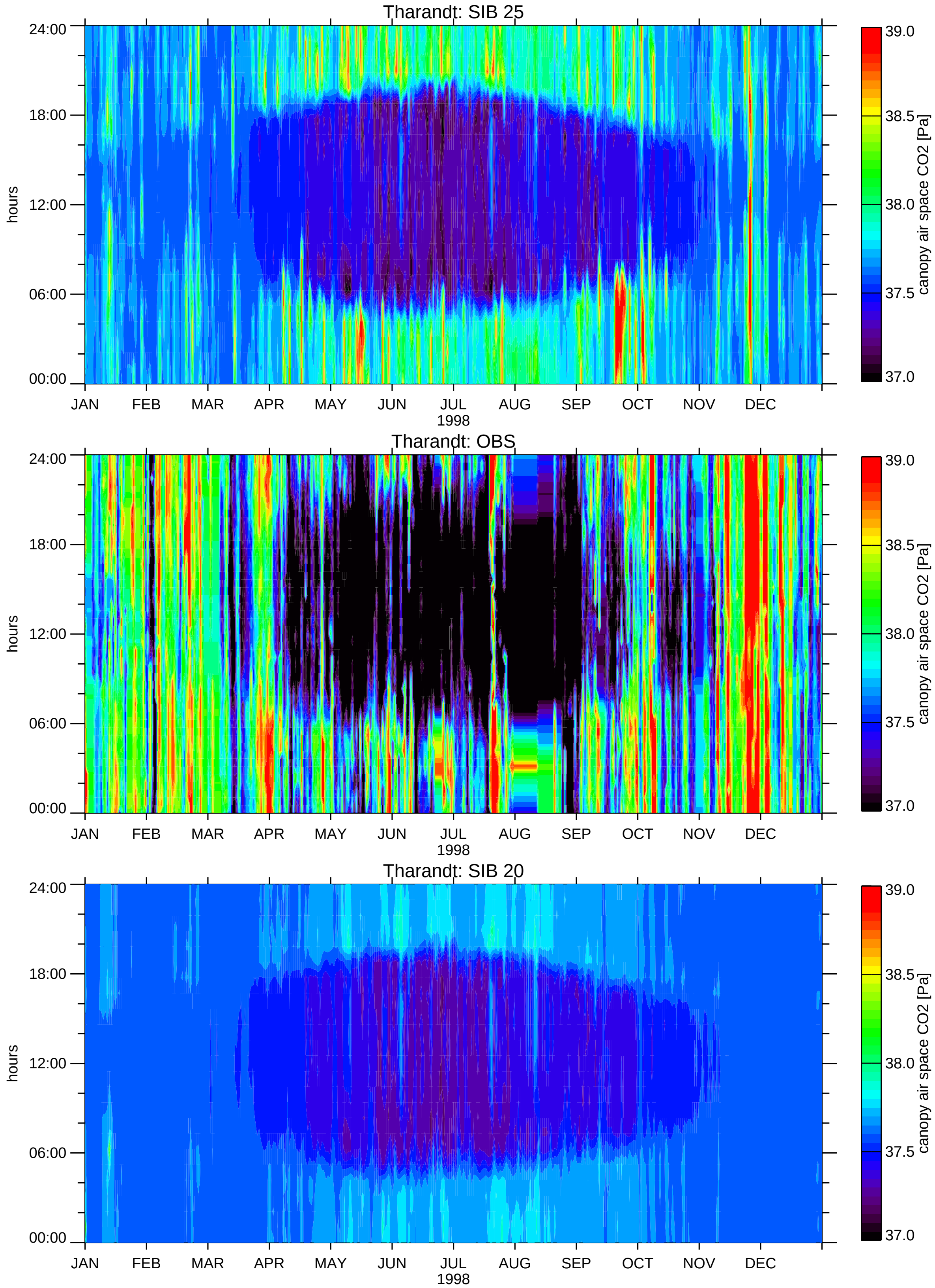

FIG. B.4: Diurnal and yearly evolution of CAS level CO_2 partial pressure (Pa) at Tharandt, 1998 for the two model versions (SiB2.5 top and SiB2.0, bottom). The middle panel shows the reference level observed pressure for reference.

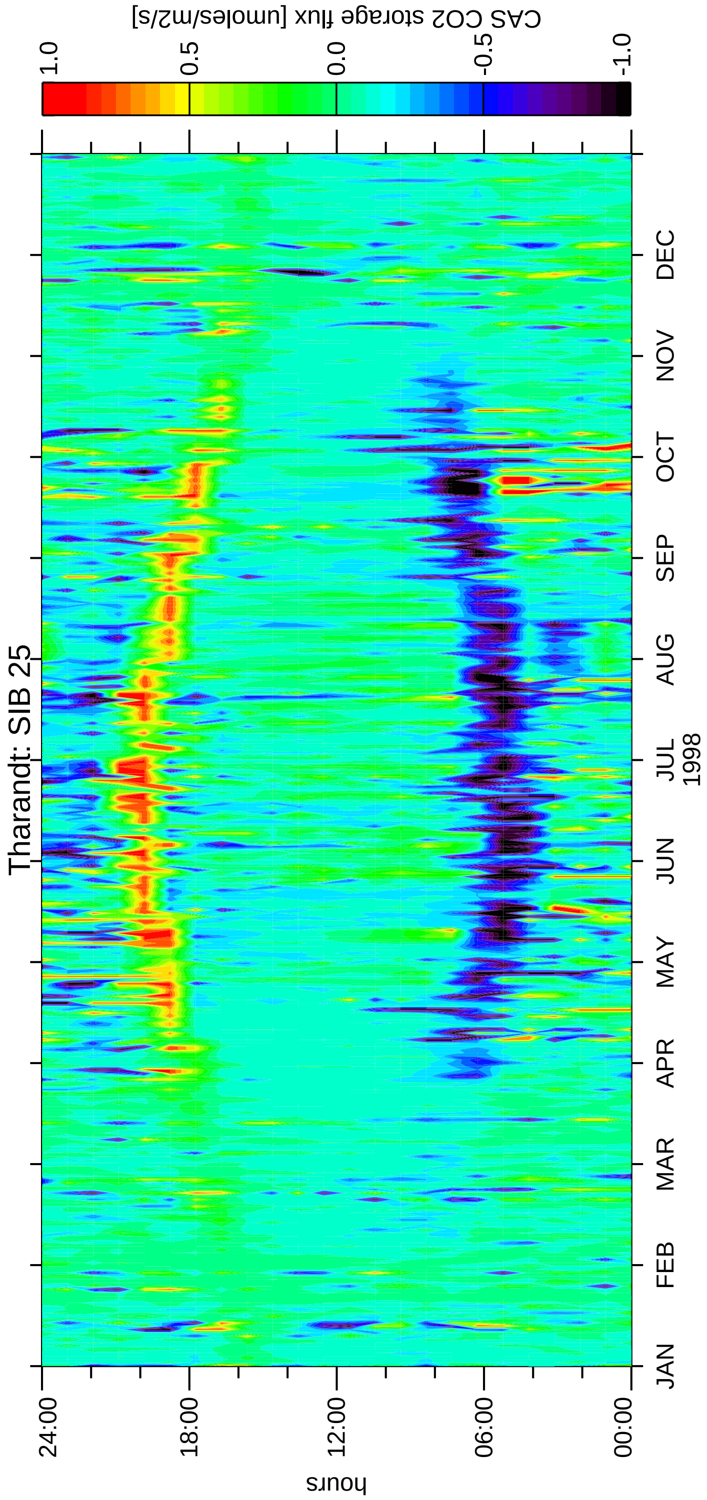

FIG. B.5: The SiB2.5 CAS CO_2 storage fluxes (μ mol m$^{-2}s^{-1}$) at Tharandt, 1998, diurnal and yearly cycles.

B.4.e Considerations on computing costs

The costs of a simulation with SiB2.5, for which three extra prognostic equations need to be solved, are offset by the overall reduction in accessory calculations (for the cross-derivative terms) and by faster convergence of the solutions. Overall, therefore, no significant changes in CPU requirements have been observed. The development and maintenance costs for the code have been greatly reduced through closer agreement of analytical and numerical solutions and through the elimination of a large number of cross derivative terms that need not be carried through the many different subroutines in the code.

B.5 Conclusions

A new solution core for the calculation of near-surface prognostics in an LSM has been developed and applied to the Sellers et al. (1996d) SiB2. The new approach consists of introducing canopy air space prognostic variables for CAS temperature (T_a), moisture (e_a) and carbon (CO_{2_a}), with corresponding storage capacities. The numerical implementation of the proposed prognostic approach introduced here has proven accurate, stable, efficient and above all easier to maintain than the diagnostic one it substitutes. We have applied the model to the off-line simulation of micrometeorological tower state variables, fluxes and concentrations from the Fluxnet project. Solutions for the prognostic variables show that the quality of the forecasts is at least as good as the one in the diagnostic system, but further reassurance about the soundness of the solutions is provided by the derived storage fluxes signatures and by the comparison of accumulated CO_2 near the surface, especially at times of large vertical stability. The diurnal and yearly evolutions of CAS variables and fluxes show that the adoption of the CAS prognostics can therefore be justified for both physical and numerical reasons. The model has been more thoroughly tested and validated in terms of heat and water fluxes over a wider variety of sites and environmental conditions in a companion paper by Stöckli and Vidale (2005). The next phase of the off-line simulations with similar micrometeorological data will include the introduction of time series of CO_2 concentrations at the reference level, in order to test the stability of the solutions and the magnitude of the response in a system with an extra degree of freedom. More dramatic effects are expected in coupled-mode experiments, in which the reference level CO_2 is allowed to oscillate freely; some of this work has already been accomplished in Denning et al. (2003) and Baker et al. (2003) for short-term studies.

B.6 Acknowledgments

This work was the result of cooperation with Prof. A.S. Denning and his group at Colorado State University, Fort Collins, CO, USA: P.L. Vidale initiated this work in 1998 while at CSU, and was supported at the time under grant US-DOE-NIGEC number DE-FC03-90ER61010. This research was later supported by the Swiss Ministry for Education and Science (BBW contract Nr. 97.008). The pre-processing of NDVI data used for driving SiB2 was accomplished at NASA Goddard, under contracts NAS5-01070, Task No. 4a, SSAI subcontract No. 2101-03-002. The original SiB2 model and all SiB2 pre-processing tools were also made available by Prof. Denning and his group. FLUXNET data were made available by R. Olson and E. Falge through the Fluxnet WWW site and CDROM.

B.7 Discretization and numerical solution of the land surface prognostic equations

The solution method, which lies at the heart of the Sato et al. (1989a) publication, simultaneously solves the system of equations for all state variables between the ground surface and the first atmospheric level (within the surface layer), including the canopy air space (CAS), having this general implicit-in-time form for each land surface prognostic variable in the LSM framework, S_x, similar to the treatment in Bhumralkar (1975):

$$c_x \frac{\partial S_x}{\partial t} \quad = \quad \sum F_x^{t+1}$$

which is discretized as:

$$c_x \frac{\Delta S_x}{\Delta t} \quad \cong \sum \quad (F_x^t + \frac{\partial F_x}{\partial t} \cdot \Delta t\} \tag{B.10}$$

where the t subscript is the time level and the x subscripts refer to any component of the system, e.g. c for canopy leaves and a for CAS. The summation is over all relevant fluxes for each variable. The original set of equations for the SiB2 LSM is described by Sato et al. (1989a) and by Sellers et al. (1996d) and comprises prognostic equations for T_g, T_c, and for soil water reservoirs.

The implementation corresponds to a backward implicit scheme in time. However, to be more general, when both left and right hand sides are at time level $t+1$, this is really an implicit system, if both are at time t, it is an open-explicit system, and, if any combination is applied, this corresponds to having a semi-implicit or even an explicit system, as discussed for instance in Polcher et al. (1998). In the original SiB2.0, parts of the right side were at time level t, so the system was semi-implicit. In the newer formulation presented here all terms but the resistance (r_x terms) network are at time $t+1$, making the new solution system, SiB2.5, fully implicit.

This set was solved with the "implicit with explicit coefficients" method of Sato et al. (1989a), which translates into using a truncated Taylor series approximation:

$$c_x \frac{\Delta S_x}{\Delta t} \cong \sum (F_x^t + \frac{\partial F_x}{\partial S_x} \cdot \frac{\partial S_x}{\partial t} \cdot \Delta t) = \sum (F_x^t + \frac{\partial F_x}{\partial S_x} \cdot \Delta S_x) \tag{B.11}$$

which forms the basis of the numerical model implementation, solving for the finite differences ΔS_x as in Sato et al. (1989a), Sellers et al. (1996d) and Randall et al. (1996).

Thus, starting with the Sellers et al. (1996d) Equations 1 through 3, and following the solution procedure implemented by Sato et al. (1989a) in Equations 1 through 5, the new (5x5) system of equations is:

$$\begin{aligned} &\left(\frac{c_c}{\Delta t} + \frac{\partial H_c}{\partial T_c} + \frac{\partial E_c}{\partial T_c} + \frac{\partial L_c}{\partial T_c}\right) \Delta T_c + \frac{\partial L_c}{\partial T_g} (1 - A_s) \Delta T_g + \frac{\partial L_c}{\partial T_s} (A_s) \Delta T_s \; + \\ &\qquad \frac{\partial H_c}{\partial T_a} \Delta T_a + \frac{\rho c_p}{\gamma} \frac{\partial e_c}{\partial e_a} \Delta e_a = R_{net_c}^t - H_c^t - E_c^t \end{aligned} \tag{B.12}$$

$$\frac{\partial L_g}{\partial T_c}\Delta T_c + \left(\frac{c_g}{\Delta t} + \frac{\partial H_g}{\partial T_g} + \frac{\partial E_g}{\partial T_g} + \frac{\partial L_g}{\partial T_g} + S_\lambda\right)\Delta T_g + \frac{\partial H_g}{\partial T_a}\Delta T_a + \frac{\rho c_p}{\gamma}\frac{\partial e_g}{\partial e_a}\Delta e_a = R^t_{net_g} - H^t_g - E^t_g - S_\lambda\left(T^t_g - T^t_d\right) \tag{B.13}$$

$$\frac{\partial L_s}{\partial T_c}\Delta T_c + \left(\frac{c_s}{\Delta t} + \frac{\partial H_s}{\partial T_s} + \frac{\partial E_s}{\partial T_s} + \frac{\partial L_s}{\partial T_s} + S_\lambda\right)\Delta T_s + \frac{\partial H_s}{\partial T_a}\Delta T_a + \frac{\rho c_p}{\gamma}\frac{\partial e_s}{\partial e_a}\Delta e_a = R^t_{net_s} - H^t_s - E^t_s - S_\lambda\left(T^t_s - T^t_d\right) \tag{B.14}$$

$$-\frac{\partial H_c}{\partial T_c}\Delta T_c - \frac{\partial H_g}{\partial T_g}\left(1-A_s\right)\Delta T_g - \frac{\partial H_s}{\partial T_s}A_s\Delta T_s + \frac{\partial H_a}{\partial T_r}\Delta T_r + \left(\frac{c_a}{\Delta t} - \frac{\partial H_c}{\partial T_a} + \frac{\partial H_a}{\partial T_a} - \left(1-A_s\right)\frac{\partial H_g}{\partial T_a} - A_s\frac{\partial H_s}{\partial T_a}\right)\Delta T_a = H^t_c - H^t_a + \left(1-A_s\right)H^t_g + A_s H^t_s \tag{B.15}$$

$$-\frac{\partial E_c}{\partial T_c}\Delta T_c - \frac{\partial E_g}{\partial T_g}\left(1-A_s\right)\Delta T_g - \frac{\partial E_s}{\partial T_s}A_s\Delta T_s + \frac{\partial E_a}{\partial e_r}\Delta e_r + \left(\frac{c_a}{\Delta t} - \frac{\partial E_c}{\partial e_a} + \frac{\partial E_a}{\partial e_a} - \left(1-A_s\right)\frac{\partial E_g}{\partial e_a} - A_s\frac{\partial E_s}{\partial e_a}\right)\Delta e_a = E^t_c - E^t_a + \left(1-A_s\right)E^t_g + A_s E^t_s \tag{B.16}$$

where the usual variable indexes apply, with the introduction of T_s, A_s for snow temperature (K) and area extent (%), and L_x for emitted longwave fluxes from each component (Wm^{-2}), so that, for instance, ΔT_c is the leaves temperature increment (K); ΔT_a is the CAS temperature increment (K); ΔT_g is the bare ground surface temperature increment (K); ΔT_s is the snow temperature increment (K); ΔT_r is the reference level temperature increment (K); Δe_a is the CAS water pressure increment (Pa); Δe_r is the ref. lev. water pressure increment (Pa); c_c is the leaves' heat capacity ($Jm^{-2}K^{-1}$); c_a is the CAS heat capacity ($Jm^{-2}K^{-1}$); c_g is the bare ground heat capacity ($Jm^{-2}K^{-1}$); c_s is the snow heat capacity ($Jm^{-2}K^{-1}$); H is the sensible heat flux (Wm^{-2}); E is the latent heat flux (Wm^{-2}). For the moisture variables, the capacities are in $Jm^{-2}Pa^{-1}$.

The temperatures of ground and snow at time t (right hand side of equations) are the same, prior to each time step, since energy exchanges and areal adjustments involving snow growth/melting are carried out between time steps. Only the time increments ΔT_g and ΔT_s are allowed to diverge into separate solutions during the simultaneous solution calculation; by the time the next prognostic time step is reached the two temperatures will be once more identical.

This system of equations is solved simultaneously by Gaussian elimination at each time step. Within the CSU GCM Randall et al. (1996), it is also possible to solve simultaneously for the evolution of the bulk mixed layer prognostic (reference) variables as influenced by surface fluxes. This option is inactive when the model is run off-line (thus the reference level variables represent boundary conditions) or when the model is coupled to a host atmospheric model that has a discrete multi-layer treatment of the boundary layer. This raises the number of equations to be simultaneously solved to 7x7.

$$-\frac{\partial H_a}{\partial T_a}\Delta T_a + \left(\frac{c_r}{\Delta t} + \frac{\partial H_a}{\partial T_r}\right)\Delta T_r = H_a^t \tag{B.17}$$

$$-\frac{\partial E_a}{\partial T_a}\Delta T_a + \left(\frac{c_r}{\Delta t} + \frac{\partial E_a}{\partial e_r}\right)\Delta e_r = E_a^t \tag{B.18}$$

where:
ΔT_a is the CAS temperature increment (K); ΔT_r is the reference level temperature increment (K); Δe_a is the CAS water pressure increment (Pa); Δe_r is the ref. lev. water pressure increment (Pa); c_a is the CAS heat capacity $(Jm^{-2}K^{-1})$; c_r is the reference level heat capacity $(Jm^{-2}K^{-1}$ or $Jm^{-2}Pa^{-1}$ for vapor pressure); H is the sensible heat flux (Wm^{-2}); E is the moisture flux $(Wm^{-2}s^{-1})$;

The expression for the individual (H and E) fluxes remains identical to the ones in Table 4, Sellers et al. (1996d), while it is their derivatives that are now simplified. The only new expressions are the ones relative to the total surface fluxes of heat and moisture, which are:

$$H_a = \rho c_p \frac{T_a - T_r}{r_a}; \qquad E_a = \frac{\rho c_p}{\gamma}\frac{e_a - e_r}{r_a} \tag{B.19}$$

The expressions for the individual resistances, r_b, r_d, r_a, r_c are now true to their definition, once T_a is now a prognostic variable and thus can be included in those equations (see the discussion on page 685 of Sellers et al. (1996d)).

In SiB2 stomatal conductance is calculated through the Ball-Berry equation, Ball et al. (1987), Ball (1988), which relates carbon assimilation to the loss of water through the stomata. This calculation is necessary to calculate transpiration rates, but also concludes the updating of the resistance network prior to the simultaneous calculation of the surface prognostic variables and will also determine the carbon flux from the surface to the first atmospheric level, according to Equation B.7.

B.8 Energy and water limitations in the implicit solution system

The partial derivative terms appearing in Equations B.12-B.16 can potentially violate water conservation, since they implicitly depend on temperature increments in the prognostic time step, which makes it difficult to establish, a priori, that water reservoirs in the canopy, soil and at the ground surface will not be exhausted during the time step.

In SiB2 a complex system of energy and water checks was responsible for restoring water levels to conservative amounts after a time step in which they had been exhausted, converting the exhausted latent heat into sensible heat.

In the new solution core, this system is both undesirable and unnecessary and the following criteria are used in order to guarantee that the "flux payback" system is not activated.

$$\begin{aligned}
\frac{\partial E_{ci}}{\partial t}\Delta t &\cong \frac{\partial E_{ci}}{\partial T}\Delta T_c \leq \alpha\lambda W_{ci}\\
\frac{\partial E_{ct}}{\partial t}\Delta t &\cong \frac{\partial E_{ct}}{\partial T}\Delta T_c \leq \alpha\lambda W_{gd}\\
\frac{\partial E_{gs}}{\partial t}\Delta t &\cong \frac{\partial E_{gs}}{\partial T}\Delta T_g \leq \alpha\lambda W_{gs}\\
\frac{\partial E_{gi}}{\partial t}\Delta t &\cong \frac{\partial E_{gi}}{\partial T}\Delta T_g \leq \alpha\lambda W_{gi}
\end{aligned} \tag{B.20}$$

where W_x are the water reservoirs (kg). Subscripts i and t refer, respectively, to interception and transpiration, while d and s refer to deep (root zone) and superficial (upper soil level). The security constant α is specified (currently 0.75) and meant to prevent the exhaustion of any reservoir over a single time step. For this specific set of secondary calculations (which are found to have a contribution much smaller than the balance of fluxes to the right of Equations B.12-B.16, a maximum possible ΔT of 3K and Δe of 500 Pa for each individual component over each time step is also imposed in order to solve the system, with the result of "slowing down" the time evolution of each prognostic as forced by these secondary feedback mechanisms.

Evaporation from individual reservoirs is also limited by energy availability:

$$\begin{aligned}
\frac{\partial E_{ci}}{\partial t}\Delta t &\cong \frac{\partial E_{ci}}{\partial T}\Delta T_c \leq \beta R_{n_c}\\
\frac{\partial E_{ct}}{\partial t}\Delta t &\cong \frac{\partial E_{ct}}{\partial T}\Delta T_c \leq \beta R_{n_c}\\
\frac{\partial E_{gs}}{\partial t}\Delta t &\cong \frac{\partial E_{gs}}{\partial T}\Delta T_g \leq \beta R_{n_g}\\
\frac{\partial E_{gi}}{\partial t}\Delta t &\cong \frac{\partial E_{gi}}{\partial T}\Delta T_g \leq \beta R_{n_g}
\end{aligned} \tag{B.21}$$

where β is a security constant (currently 0.5) meant to energetically limit the exhaustion of each reservoir over a single time step.

From these expressions it is possible to derive the limitations to the partial derivatives of vapor pressure with relation to temperature that are to be used in the solution core (previous section) so that no reservoir will be exhausted a priori during a single time step. A maximum possible ΔT of 3K for each component over one time step is also imposed here.

Appendix C

Analytical and numerical formulations for soil water transfer

C.1 Vertical water transfer scheme

The soil water scheme used in this study is part of the land surface scheme SiB 2.5. The formulation is based on Bonan (1996) and is a standard multilayer diffusive soil water transfer scheme like is used in most of todays land surface models (e.g. CLM2 (Dai et al., 2003) used in CCM3, or MOSES (Cox et al., 1999) used in HadCM3).

C.1.a Analytical formulation

Soil water content changes according to the conservation equation

$$\frac{\partial \theta}{\partial t} = -\frac{\partial q}{\partial z} - \frac{\partial e}{\partial z}, \tag{C.1}$$

where θ is the volumetric water content [$m^3 m^{-3}$], z is the soil depth [m] (negative downwards), q is the vertical water flux [ms^{-1}] and t is the time [s]. e is the evapotranspiration flux [ms^{-1}] and $e = e_T + e_E$, thus consists of transpiration and evaporation. The vertical water flux q (positive is upwards) is described by Darcy's law

$$q = -K\left(\frac{\partial \psi}{\partial z} + 1\right) = -K\left(\frac{\partial \psi}{\partial \theta}\frac{\partial \theta}{\partial z} + 1\right), \tag{C.2}$$

where

$$K = K_s S^{2B+3} e^{fz} \quad \text{and} \quad \psi = \psi_s S^{-B} \quad \text{and} \quad S = \theta/\eta_s. \tag{C.3}$$

Here K and K_s are the unsaturated and saturated hydraulic conductivies [ms^{-1}], S is the soil moisture relative to saturation [-], B is an empirical soil texture parameter [-] based on Clapp and Hornberger (1978), f is the exponential decay parameter of the hydraulic conductivity [m^{-1}], ψ and ψ_s are the unsaturated and the saturated soil matrix tensions [m] and η_s is the soil porosity [-]. Combining equations C.1 and C.2 results in the Richards equation

$$\frac{\partial \theta}{\partial t} = \frac{\partial}{\partial z}\left[K\left(\frac{\partial \psi}{\partial \theta}\frac{\partial \theta}{\partial z} + 1\right) - e\right], \tag{C.4}$$

which describes the temporal and spatial evolution of soil moisture.

C.1.b Numerical solution

A finite number L of soil layers with layer thickness Δz_j are defined and the spatial discretization uses a staggered conservative grid. Soil moisture and soil water tension are defined at the center of each layer. The soil moisture storage change in soil layer j is calculated according to

$$\frac{\partial \theta_j}{\partial t} = \frac{1}{\Delta z_j}\left[-q_{j-\frac{1}{2}} + q_{j+\frac{1}{2}} - \frac{f_{w,j} r_j e_T}{\sum_{j=1}^{L} f_{w,j} r_j}\right], \tag{C.5}$$

where $q_{j-\frac{1}{2}}$ is the water flux between layers $j-1$ and j, and $q_{j+\frac{1}{2}}$ is the water flux between layers j and $j+1$. For the topmost soil layer, $q_{j-\frac{1}{2}}$ is the soil infiltration flux from rainfall or snowmelt and the evaporation flux $-e_E$ [ms^{-1}] is also part of right-hand side of equation C.5. For the lowest soil layer $q_{j+\frac{1}{2}}$ is the drainage flux (equal K_j), which is gravitational drainage only and is added to the land surface model runoff. Transpiration loss is discretized for each layer by multiplying the transpiration flux e_T with the root fraction r_j [-] of the respective soil layer (after Zeng (2001)). In the 3-layer formulation $r_2 = 1$ and $r_{1,3} = 0$ since all roots are constrained to the 2nd layer (root layer). $f_{w,j}$ is a model diagnostic variable (Sellers et al., 1996d) limiting transpiration by soil layer depending on soil moisture and is calculated as

$$f_{w,j} = \frac{1}{1+\exp\left[0.02(\psi_c - \psi_j)\right]}; \quad \text{and} \quad f_w = \sum_{j=1}^{L} f_{w,j} r_j, \tag{C.6}$$

is the total transpiration limitation, where ψ_c is the critical water potential [m], a vegetation type dependent parameter (see Sellers et al. (1996d)). The flux between layers $j-1$ and j, $q_{j-\frac{1}{2}}$, is discretized as

$$q_{j-\frac{1}{2}} = K_{j-\frac{1}{2}}\left(\frac{2(\psi_j - \psi_{j-1})}{\Delta z_j + \Delta z_{j-1}} + 1\right). \tag{C.7}$$

(similarly for $q_{j+\frac{1}{2}}$). For the discretization in time of the hydrological fluxes an implicit finite difference scheme is used

$$\frac{\Delta \theta_j}{\Delta t} = \frac{1}{\Delta z_j}\left[-q^{n+1}_{j-\frac{1}{2}} + q^{n+1}_{j+\frac{1}{2}}\right]. \tag{C.8}$$

Since K and ψ are non-linear functions of θ (see equation C.3), $q_{j-\frac{1}{2}}$ and $q_{j+\frac{1}{2}}$ are functions of θ_{j-1},θ_j and θ_{j+1}. This is locally linearized according to

$$q^{n+1}_{j-\frac{1}{2}} = q^{n}_{j-\frac{1}{2}} + \frac{\partial q^{n}_{j-\frac{1}{2}}}{\partial \theta_{j-1}}\Delta\theta_{j-1} + \frac{\partial q^{n}_{j-\frac{1}{2}}}{\partial \theta_{j}}\Delta\theta_{j}. \tag{C.9}$$

This linear equation set is applied to solve equation C.5 for the changes in soil moisture $\Delta\theta_j$ in each layer j by the use of a tridiagonal solving algorithm, generally used for solving the finite difference diffusion equation. Since it has been recognized (e.g. by Wu et al. (2002)) that this solution scheme could lead to unrealistic soil moisture conditions, authors (e.g. Dai et al. (2003) or Yang and Niu (2003)) have proposed numerical constraints for this scheme. [1]

The following constraints are used here: to derive $K_{j-\frac{1}{2}}$ from θ_j and θ_{j-1}, $S_{j-\frac{1}{2}}$ is calculated as $S_{j-\frac{1}{2}} = max(\theta_{j-1}, \theta_j)/\eta_s$, except for the first soil layer, where $S_1 = \theta_1/\eta_s$. This formulation has been shown to give better results for the calculation of wetness fronts, where the high spatial variability of K at the interface between wet and dry soil layers can unrealistically block vertical water transfer. A simple analytical experiment justifies the use of this numerical constraint: Let us assume a loamy soil with $K_s = 7.2 \cdot 10^{-6}$ [ms^{-1}], $\psi_s = -0.57$ [m], $B = 5.3$ [-], $\eta_s = 0.49$ and three soil layers with $\theta_{j-1} = 0.47$ [-], $\theta_j = 0.1$ [-] and $\theta_{j+1} = 0.1$ [-]. A typical wetness front where the top soil is almost saturated while the lower soil is at wilting point. Substituting equation C.7 into C.9 includes 1st order derivates of K to θ, which determine the updated water fluxes at $t+1$. When defining K at the center of each layer these derivates are high for the top layer (K sensitive to $\Delta\theta$) but K is insensitive to $\Delta\theta$ in the lower layer

$$\frac{\partial K_{j-1}}{\partial \theta_{j-1}} = 1.2 \cdot 10^{-4} \ , \ \frac{\partial K_j}{\partial \theta_j} = 4.0 \cdot 10^{-7}. \tag{C.10}$$

Defining K at the interface between layers, the non-linear dependence of K from θ also unrealistically inhibits water flux from the saturated to the unsaturated layer

$$\frac{\partial K_{j-\frac{1}{2}}}{\partial \theta_{j-1}} = 1.3 \cdot 10^{-7} \ , \ \frac{\partial K_{j-\frac{1}{2}}}{\partial \theta_j} = 6.2 \cdot 10^{-7}, \tag{C.11}$$

because K for $\theta = (0.47 + 0.1)/2$ is by orders of magnitude smaller than for $\theta = 0.47$. When defining K from the maximum θ of two interfacing layers, K is sensitive to $\Delta\theta$ between the wet/dry layers $j-1$ and j, but is insensitive between lower dry/dry layers. This allows for the wetness front to propagate downwards even in the extreme situations exemplified above

$$\frac{\partial K_{j-\frac{1}{2}}}{\partial \theta_{j-1}} = 1.2 \cdot 10^{-4} \ , \ \frac{\partial K_{j-\frac{1}{2}}}{\partial \theta_j} = 5.6 \cdot 10^{-4}. \tag{C.12}$$

Soil freezing can physically inhibit water transfer and thus K and ψ are adjusted for soil temperature $T_j[°C]$ in each layer (like in Sellers et al. (1996d)) according to

$$K_{f,j} = K_j f_{f,j}, \quad \psi_{f,j} = \psi_j / f_{f,j} \quad \text{where} \quad f_{f,j} = \begin{cases} 1 \cdot 10^{-8} & \text{if } T_j < -7.5°C \\ (7.5 - T_i)/7.5 & \text{if } 0°C > T_j > -7.5°C \\ 1 & \text{if } T_j > 0°C \end{cases} \tag{C.13}$$

As described in Sellers et al. (1996d) saturation excess runoff may be produced from the topmost soil layer at each time step. If water in lower soil layers exceeds their saturation capacity, it is added to the soil column by saturating soil layers, starting from the topmost saturated layer. Multilayer soil moisture schemes like the one presented here are used in most recent LSMs (e.g. LSM, CLM2, MOSES) but the authors suggest that their validity

[1] K is linearly approximated at $t+1$ as described above. The non-linear dependence of K from θ however makes this approximation problematic in certain cases, also described above. A better solution needs to be found despite this scheme being currently state-of-the-art in the LSM community.

is tested in a range of climatic environments, where long time-series of atmospheric forcing and soil moisture data are available.

C.1.c Numerical accuracy and consistency

To simplify the calculations of stability by assuming K constant, by replacing ψ and θ with u, and by excluding the evapotranspiration term,

$$\frac{\partial u}{\partial t} = K\frac{\partial^2 u}{\partial z^2} \tag{C.14}$$

can be used instead of equation C.4. Combining equations C.5 and C.9 results in a standard finite difference diffusion scheme, backward in time and centered in space and its simplified form is

$$\frac{u_j^{n+1} - u_j^n}{\Delta t} = K\frac{u_{j+1}^{n+1} - 2u_j^{n+1} + u_{j-1}^{n+1}}{\Delta z^2}. \tag{C.15}$$

The accuracy of the scheme is found by expanding the terms like u_j^{n+1} in Taylor series about t_0 and z_0 and substituting these expansions into the above finite difference formula

$$\frac{\partial u}{\partial t} = K\frac{\partial^2 u}{\partial z^2} - \frac{\Delta t}{2}\frac{\partial^2 u}{\partial t^2} - \frac{\Delta z^2}{12K}\frac{\partial^2 u}{\partial t^2} + O\left(\Delta t^2, \Delta z^4\right). \tag{C.16}$$

The lowest order of Δz and Δt in the Taylor series are the truncation error and determine the order of accuracy. The finite difference scheme is therefore first order accurate in time and second order in space. Accuracy can be improved by reducing Δt. The vertical soil water transfer scheme can be used at partial LSM time steps (currently 1/5 of Δt_{LSM}). With Δz and $\Delta t \to 0$ equation C.16 converges to its analytical formulation, equation C.5, thus the scheme is consistent.

C.1.d Numerical stability and convergence

The same assumptions as above are made to test the numerical stability by the use of the von Neumann's Method. Equation C.15 is transformed in a finite Fourier series by the use of the following relationships

$$u_j^n = e^{ikj\Delta z} \quad \text{and} \quad u_j^{n+1} = A_k u_j^n \quad \text{and} \quad s = K\frac{\Delta t}{\Delta z^2}, \tag{C.17}$$

where A_k is a complex constant, the amplification factor between two time steps Δt. Substituting terms in the diffusion scheme by these relationships we get

$$A_k e^{ikj\Delta z} = e^{ikj\Delta z} + A_k s e^{ik(j+1)\Delta z} - 2A_k s e^{ikj\Delta z} + A_k s e^{ik(j-1)\Delta z}, \tag{C.18}$$

which can be solved for A_k

$$A_k = \left[1 + 2s(1 - \cos k\Delta z)\right]^{-1}, \tag{C.19}$$

and thus, for any Δz, Δt and K $|A_k| \leq 1$. In other words, the scheme is unconditionally stable. Consistency and stability are sufficient to guarantee convergence.

C.1.e Idealized infiltration and drainage experiments

Idealized infiltration and drainage experiments (not including evapotranspiration losses and soil freezing) have been conducted to demonstrate the validity of the above described scheme. In these experiments the upper boundary includes surface runoff and infiltration and the lower boundary has drainage runoff due to gravitation. In the top plots of figure C.1 dry soils (initialized with a relative soil moisture to saturation of 0.2) are infiltrated with a constant value (set to K_s of the respective soil type). Sandy soil shows a very fast transfer of the wetting front, becoming saturated within a few hours, while loamy and clay soils, with a much lower hydraulic conductivity, show a slow movement of the wetting front. Soils in the bottom plots of figure C.1 were initialized to saturation and were allowed to drain without providing any infiltration flux. While after around 100h the sandy soil has nearly reached its field capacity and only drains slowly after that, the loamy soil shows a steady decrease of the soil wetness even after 200h or more. The clay soil retains soil moisture for a much longer time. Drainage occurs slower in lower layers because K decays exponentially with depth according to equation C.3.

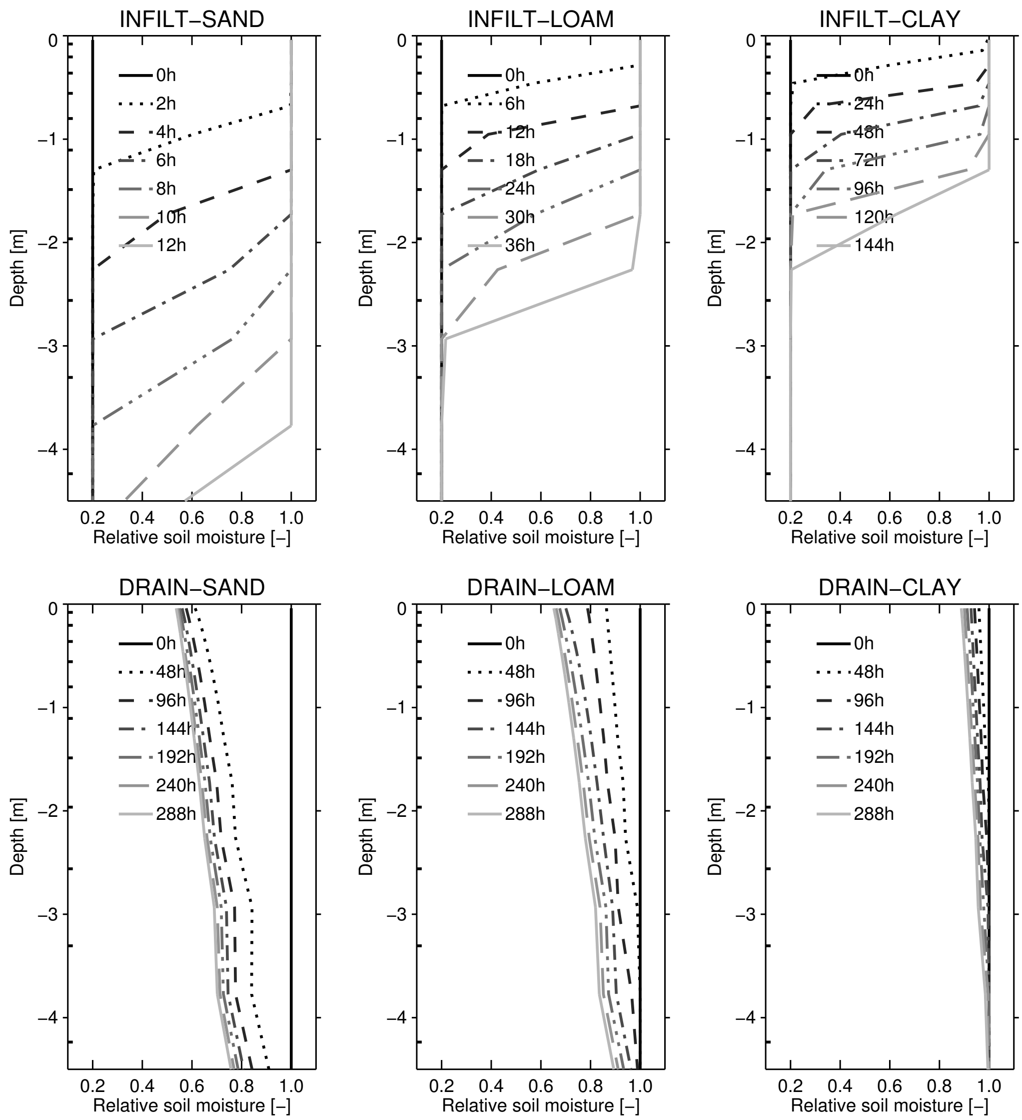

Fig. C.1: Idealized infiltration (top) and drainage (bottom) experiments using a multi-layer soil scheme

C.2 Horizontal water transfer scheme

The analytical formulation of the Topmodel approach used here is based on Beven and Kirkby (1979), while the numerical implementation is similar to the one used in Walko et al. (2000) and Gedney and Cox (2003).

C.2.a Analytical formulation

The saturated hydraulic conductivity decreases exponentially with depth

$$K_s(z) = K_s(0)e^{fz}, \tag{C.20}$$

where $K_s(0)$ is the saturated hydraulic conductivity [ms^{-1}] at the surface, z is the negative depth [m] in the soil, and f is the e-folding depth [m^{-1}] of K_s. With this formulation, hydraulic conductivity ceases below a certain depth and sufficient rainfall/snowmelt will create a water table, where the soil becomes saturated. The parameter f is an empirical tuning parameter and sensitivity experiments (e.g. by Niu and Yang (2003)) show that especially the water table depth and also runoff depend on it. Integrating K_s over the whole depth results in the saturated hydraulic transmissivity T_0 [m^2s^{-1}]

$$T_0 = \int_{-\infty}^{0} K_s(0)e^{fz}dz = \frac{K_s(0)}{f}. \tag{C.21}$$

With topography, Topmodel assumes that the water table is parallel to the soil surface and the slope $\tan\beta$ [-] generates a local lateral water flux, which is expressed as discharge per unit topography contour length q [m^2s^{-1}]. q can be derived by vertically integrating equation C.20 to the local steady-state water table z_w^∞

$$q = aR = T_0 e^{fz_w^\infty} \tan\beta. \tag{C.22}$$

This local lateral water flux can be sustained by a steady-state horizontally recharging precipitation R [ms^{-1}] supplied by the the upstream catchment area per unit topography contour length a [m]. The steady-state local water table is then derived by solving equation C.22 for z_w^∞

$$z_w^\infty = \frac{1}{f}\ln\left(\frac{aR}{T_0\tan\beta}\right). \tag{C.23}$$

The mean water table in the catchment is calculated by integrating equation C.23 over the catchment area A [m^2]

$$\overline{z_w} = \frac{1}{A}\int_A z_w^\infty dA = \frac{1}{A}\int_A \frac{1}{f}\ln\left(\frac{a}{\tan\beta}\right)dA - \frac{1}{A}\int_A \frac{1}{f}\ln T_0 dA + \frac{1}{f}\ln R, \tag{C.24}$$

and the steady-state local water table can be related to the mean catchment water table by solving the above equation for R and substituting it into equation C.23, resulting in

$$z_w^\infty = \overline{z_w} + \frac{1}{f}(W - \overline{W}), \tag{C.25}$$

where

$$W = \ln\left(\frac{aT_e}{T_0 \tan\beta}\right), \tag{C.26}$$

$$\overline{W} = \frac{1}{A}\int_A W dA, \tag{C.27}$$

and

$$\ln T_e = \frac{1}{A}\int_A \ln T_0 dA. \tag{C.28}$$

The steady-state local water table z_w^∞ is therefore dependent on its catchment mean value $\overline{z_w}$ and on the the local deviation of the so called wetness index W from its catchment mean value $\overline{W}$. The wetness index is a time-invariant function of slope β, local (area mean) hydraulic transmissivity T_0 (T_e) and upstream catchment area per unit topography contour length a. A low wetness index may occur because of a small upstream catchment area or because of a high local slope angle. Very different terrain configurations can have similar wetness indices, thus having a similar tendency to gain or lose water in the saturated zone.

There is a net lowering of the catchment mean water table if no recharge occurs, thus the recharge for maintaining the catchment mean (and therefore the local) water table can be calculated by substituting equations C.26, C.27 and C.23 into equation C.25 and solving for

$$R = T_e e^{f\overline{z_w}} e^{-\overline{W}}. \tag{C.29}$$

R is also the catchment average drainage rate for the catchment mean water table $\overline{z_w}$. With no precipitation recharge, $\overline{z_w}$ is lowered by velocity R/η_s, where η_s is the porosity of the soil [-]. The response time of this lateral sub-surface water flow is largely dependent on the mean water table depth due to the exponential decay of the hydraulic conductivity with depth and on the catchment mean wetness index. The characteristic time-scale of the catchment mean lateral water flux can be calculated as

$$\tau = \frac{\eta_s}{fT_e e^{f\overline{z_w}} e^{-\overline{W}}}. \tag{C.30}$$

Table C.1: Sample τ [days] for a range of mean water table depths $\overline{z_w}$ and mean wetness index values $\overline{W}$ ($K_s = 7.2 \cdot 10^{-6}$ [ms^{-1}], $\eta_s = 0.49$ [-], $f = 0.5$ [m^{-1}])

	$\overline{W}$ [-]		
$\overline{z_w}$ [m]	5	7	9
-0.1	122	908	6710
-1.0	192	1424	$1.1 \cdot 10^4$
-3.0	524	3870	$2.8 \cdot 10^4$

As shown in table C.1, the lateral water flux is not effective at low water table depths and in lowland areas (high $\overline{W}$).

C.2.b Numerical solution

Originally Topmodel was developed to provide a catchment-scale water balance and an explicit routing of groundwater downslope may be formulated using the analytical equations described above. In climate modeling applications a statistical solution of the above physically-based solution is preferred, due to the high computational cost of an explicit routing of groundwater downslope in a catchment. For a typical grid cell of a regional or global climate model (in our study 0.5° and 1°), the time-invariant wetness indices are derived according to equation C.26 by the use of a high resolution (to include local-scale variability, see Wolock and McCabe (2000) for a review of the resolution dependence of the wetness index) topography dataset. The spatial discretization of equation C.25 is achieved by deriving N patches p for each grid cell of the model domain and wetness indices W_p are binned uniformly, and area fractions A_p are derived for each of the patches, such that

$$\overline{W} = \sum_{p=1}^{N} W_p A_p \quad \text{where} \quad \sum_{p=1}^{N} A_p = 1. \tag{C.31}$$

With $\overline{W}$, W_p and $z_p(t)$ available for every patch at time t, equation C.25 can be used to calculate the steady-state local water table z_p^∞ from the grid cell mean water table $\overline{z}(t)$ by the use of the topography related wetness indices

$$z_p^\infty = \overline{z}(t) + \frac{1}{f}(W_p - \overline{W}) \quad \text{where} \quad \overline{z}(t) = \sum_{p=1}^{N} z_p(t) A_p. \tag{C.32}$$

This steady-state water table will not equal the instantaneous water local table during the simulation. The assumption of a steady-state soil water table due to a constant recharge is not directly applicable when the Topmodel approach is coupled to a LSM. Precipitation, evapotranspiration and surface runoff processes influence the recharge of the water table on a wide range of spatial and temporal scales. Instead of assuming steady-state conditions, the charcteristic time-scale τ is used to redistribute water according to the instantaneous and the steady-state water table for each subgrid patch p. Discretization in time is achieved by applying a forward time differencing scheme

$$z_p^{n+1} = z_p^n + (z_p^\infty - z_p^n)\frac{\Delta t}{\tau}, \tag{C.33}$$

where Δt is the model time step and is generally by orders-of-magnitude shorter than τ (table C.1).

C.2.c Interaction between Topmodel and the multilayer soil

At every LSM time-step n the instantaneous local water table depth z_p^n of every individual patch p is diagnosed by counting the saturated soil layers from the bottom of the multilayer soil profile until the first unsaturated soil layer is found. This procedure requires a multilayer soil scheme like the one described in the previous Appendix section. For diagnosing saturation a threshold of $0.95\eta_s$ is used. A small downward adjustment of the water table is made for the last saturated soil level by subtracting its saturation deficit

$(1 - S)dz$ [m] from the diagnosed water table depth, where S is the soil water content relative to saturation [-].

For patches where the water table falls, the soil moisture profile is updated by subtracting the negative water table change from the topmost saturated soil layer. For patches with a rising water table, the water table change is used to saturate the soil column, starting from the lowest unsaturated soil layer. In the case of total saturation of the whole soil column, saturation excess runoff is produced. Complete drainage of a soil column cannot occur in this scheme, because the lateral soil moisture transfer ceases rapidly with low soil moisture and deep water tables.

In comparison to the multilayer soil scheme described in the previous section, Topmodel creates lateral water fluxes not only from the bottom layer, but also from other layers depending on water table depth. The subgrid-patches also provide a means to relate these fluxes to local-scale topographic variability. The sub-surface drainage $R_{p,j}$ [ms^{-1}] out of the grid box is summed over every patch p and soil layer j according to the patch slope $(\tan\beta)_p$ and hydraulic conductivity (determined in the vertical water transfer scheme, see previous section) $K_{p,j}$ [ms^{-1}]

$$R_{p,j} = K_{p,j}(\tan\beta)_p. \tag{C.34}$$

This drainage formulation is sensitive to the terrain slope and to the height of the water table (which influences K). After a rainfall event, saturated near-surface layers in slopy patches (with low wetness indices) will generate a fast response sub-surface drainage into the stream-bed and lowland patches, while drainage from these lowland patches (having high wetness indices) generate a slower drainage response, resulting from the slow rise of the local water table, due to vertical and lateral water inflow. In contrast to the multilayer soil scheme, where runoff can only occur from the surface or from baseflow, a continuous distribution between these two runoff processes is provided by the use of the Topmodel formulation, since the lateral water distribution links the time-scales of fast runoff from topography and slow drainage from water table changes.

The above described Topmodel+Multilayer formulation conserves water per grid box (or per catchment, depending on how the grid boxes are defined), and not per patch, since water flows between patches according to their W_p deviation from the grid average $\overline{W}$ (equations C.32 and C.33), and grid-average runoff is calculated as shown in equation C.34.

C.2.d Numerical accuracy and consistency

To test numerical accuracy and convergence, equation C.33 is transformed into a forward upstream finite difference scheme by substituting z with u and τ with $\Delta x/c$, resulting in

$$\frac{u_j^{n+1} - u_j^n}{\Delta t} = c\frac{u_{j+1}^n - u_j^n}{\Delta x}, \tag{C.35}$$

A Taylor expansion about u_j^n results in

$$\frac{\partial u}{\partial t} = c\frac{\partial u}{\partial x} + \frac{\partial^2 u}{\partial t^2}\frac{\Delta t}{2} + c\frac{\partial^2 u}{\partial x^2}\frac{\Delta x}{2} + O(\Delta t^2, \Delta x^2). \tag{C.36}$$

which means that the scheme is first order accurate in time and space and is convergent for Δt and $\Delta x \to 0$, thus the scheme is consistent.

C.2.e Numerical stability

The von Neumann method is used to test numerical stability. By applying the following relationships

$$u_j^n = e^{ikj\Delta z} \quad \text{and} \quad u_j^{n+1} = A_k u_j^n \quad \text{and} \quad s = c\frac{\Delta t}{\Delta x}, \tag{C.37}$$

equation C.35 is transformed into a finite Fourier series and solved for the amplification factor A_k

$$\begin{aligned} A_k e^{ikj\Delta x} &= e^{ikj\Delta x} + s e^{ik(j+1)\Delta x} - s e^{ikj\Delta x}, \\ A_k &= 1 + s(e^{ik\Delta x} - 1), \\ |A_k| &= 1 - 2s(1-s)(1 - \cos k\Delta x) \leq 1. \end{aligned} \tag{C.38}$$

Since $(1 - \cos k\Delta x) \geq 0$ for all $k\Delta x$, the inequalilty reduces to $2s(1-s) \geq 0$, which is satisfied by $0 \leq s \leq 1$. The scheme therefore is conditionally stable under the following constraints

$$0 \leq \frac{\Delta t}{\tau} \leq 1. \tag{C.39}$$

Δt is the model time step and is in the order of minutes, τ is the response time for catchment-scale groundwater flow and is in the order of 10's of days to 1000's of days as this was found in our idealized experiments and shown in table C.1. The stability condition is therefore fullfilled for the chosen application of groundwater flow. Given that the scheme is stable and consistent, convergence is also satisfied.

C.2.f Diagnostic of water table in a discrete soil scheme

The application of Topmodel within an LSM requires to diagnose the water table from a multilayer soil scheme and the accuracy of this procedure depends on the number of soil layers. For this study, 12 soil layers were used. Idealized experiments have been performed beforehand to evaluate the number of soil layers that allow an accurate derivation of the water table. The experiments were performed using a fixed soil depth of 12.6m, a saturated hydraulic conductivity $K_s = 35 \cdot 10^{-6}$ [ms^{-1}] with an exponential decay parameter $f = 0.5$ [m^{-1}], porosity $\eta_s = 0.4$ and a sample catchment with wetness index values ranging between 3.9 - 13.2. The soil was initialized fully saturated, setting the water table depth at $z = 0$m. Topmodel was integrated for a year and no recharge due to precipitation/snowmelt was included. 10 subgrid patches were used in the numerical experiments. In figure C.2 (left) the catchment average mean water table is plotted for this idealized simulation. In the analytical solution the water table is not diagnosed from discretized soil layers but its decay is calculated from the integration of equation C.29 (catchment-mean topography driven runoff, divided by η_s). It shows the fast decay (resulting in large runoff) at high water table levels and slow water table changes at the end of the simulation. While in the 24 and 12 layer experiments the influence of the discrete soil scheme is still visible (R^2=0.996 and 0.985, respectively), the decay is well corresponding to the analytical solution. The 6 and 3 layer soil schemes have trouble to properly diagnose the temporal evolution of the water table (R^2=0.976 and 0.914). From

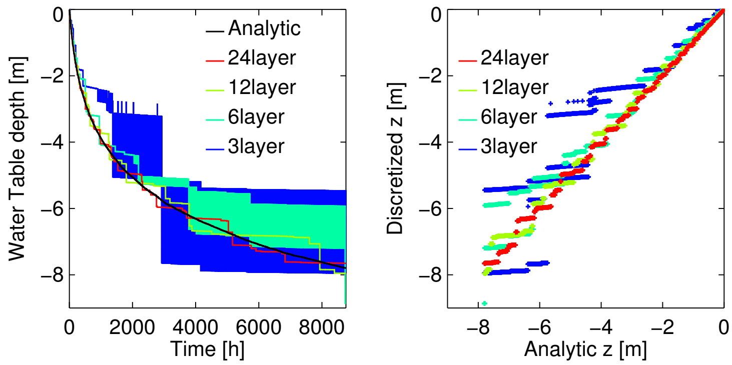

FIG. C.2: catchment wide mean water table evolution in an idealized experiment by diagnosing the water table from discretized soil layers (3, 6, 12 and 24) and by analytically calculating it.

the right part of figure C.2 it can furthermore seen that the diagnosed water table in the 3 and 6 layer formulation is bound to certain depth ranges, which of course are the soil layer depths. Increasing numbers of soil layers (an infinite number may be though of) converges the discrete water table diagnosis to the analytical solution. A multilayer soil scheme is therefore a requirement for the proper coupling of the Topmodel to an LSM. The widely used 3-4 layer or single layer (Bucket) soil schemes do not hold for this application.

The above experiment used a soil type which corresponds to a sandy-loam soil. Sand and clay soils have also been tested and show similar sensitivity to the chosen discretization of the soil.

References

Arora, V. K., 2002: Modeling vegetation as a dynamic component in soil-vegetation-atmosphere transfer schemes and hydrological models. *Reviews of Geophysics*, **40**, 3–1 – 3–27.

Arora, V. K., and G. J. Boer, 2002: A GCM-based assessment of the global moisture budget and the role of land-surface moisture reservoirs in processing precipitation. *Climate Dynamics*, **20**, 13–29.

—, 2003: A Representation of Variable Root Distribution in Dynamic Vegetation Models. *Earth Interactions*, **7**, 1–19.

Asrar, G., E. T. Kanemasu, R. D. Jackson, and P. J. Pinter, 1985: Estimation of total above-ground phytomass production using remotely sensed data. *Remote Sens. Environ.*, **17**, 211–220.

Avissar, R., P. L. S. Dias, M. A. F. S. Dias, and C. Nobre, 2002: The Large-Scale Biosphere-atmosphere Experiment in Amazonia (LBA): Insights and future research needs. *J. Geophys. Res.-Atmos.*, **107**, art. no.–8086.

Avissar, R., and R. A. Pielke, 1989: A parameterization of heterogeneous land surfaces for atmospheric numerical models and its impact on regional meteorology. *Monthly Weather Review*, **117**, 2113–2136.

Baker, I., A. S. Denning, N. Hanan, L. Prihodko, M. Uliasz, P. L. Vidale, K. Davis, and P. Bakwin, 2003: Simulated and observed fluxes of sensible and latent heat and CO2 at the WLEF-TV tower using SiB2.5. *Glob. Change Biol.*, **9**, 1262–1277.

Baldocchi, D., E. Falge, L. Gu, R. Olson, D. Hollinger, S. Running, P. Anthoni, C. Bernhofer, K. Davis, R. Evans, J. Fuentes, A. Goldstein, G. Katul, B. Law, X. Lee, Y. Malhi, T. Meyers, W. Munger, W. Oechel, K. T. P. U, K. Pilegaard, H. P. Schmid, R. Valentini, S. Verma, T. Vesala, K. Wilson, and S. Wofsyn, 2001: FLUXNET: A New Tool to Study the Temporal and Spatial Variability of Ecosystem-Scale Carbon Dioxide, Water Vapor, and Energy Flux Densities. *Bulletin of the American Meteorological Society*, **82**, 2415–2433.

Ball, J. T., 1988: An analysis of stomatal conductance. Ph.D. dissertation, Department of Biological Sciences, Stanford University.

Ball, J. T., I. E. Woodrow, and J. A. Berry, 1987: A model predicting stomatal conductance and its contribution to the control of photosynthesis under different environmental conditions. *Progress in Photosynthesis Research*, J. Biggins, Ed., Nihjoff, Dordrecht, 221–224.

Baret, F., and G. Guyot, 1991: Potentials and limits of vegetation indexes for LAI and APAR assessment. *Remote Sens. Environ.*, **35**, 161–173.

Betts, A., P. Viterbo, A. C. M. Beljaars, and B. J. J. M. van den Hurk, 2001: Impact of Boreas on the ECMWF forecast model. *Journal of Geophysical Research*, **106**, 33 593–33 604.

Betts, A. K., and J. H. Ball, 1997: Albedo over the boreal forest. *J. Geophys. Res.-Atmos.*, **102**, 28 901–28 909.

Betts, R. A., P. M. Cox, S. E. Lee, and F. I. Woodward, 1997: Contrasting physiological and structural vegetation feedbacks in climate change simulations. *Nature*, **387**, 796–799.

Betts, R. A., P. M. Cox, and F. I. Woodward, 2000: Simulated responses of potential vegetation to doubled-CO2 climate change and feedbacks on near-surface temperature. *Glob. Ecol. Biogeogr.*, **9**, 171–180.

Beven, K. J., and M. J. Kirkby, 1979: A physically based, variable contributing area model of basin hydrology. *Hydrological Sciences Bulletin*, **24**, 43–69.

Bhumralkar, C. M., 1975: Numerical experiments on computation of ground surface-temperature in an atmospheric general circulation model. *J. of Applied Meteorology*, **14**, 1246–1258.

Bonan, G. B., 1996: A land surface model (LSM version 1.0) for ecological, hydrological, and atmospheric studies: technical description and user's guide. NCAR Technical Note NCAR/TN-417+STR, NCAR, Boulder, Colorado USA.

—, 2002: *Ecological Climatology*. Cambridge University Press, Cambridge.

Boone, A., F. Habets, J. Noilhan, D. Clark, P. Dirmayer, S. Fox, Y. Gusev, I. Haddeland, R. Koster, D. Lohmann, S. Mahanama, K. Mitchell, O. Nasonova, G.-Y. Niu, A. Pitman, J. Polcher, B. Shmakin, K. Tanaka, B. van den Hurk, S. Verant, D. Verseghy, and P. Viterbo, 2004: The Rhône-Aggregation Land Surface Scheme Intercomparison Project: An Overview. *Journal of Climate*, **17**, 187–208.

Bounoua, L., G. J. Collatz, S. O. Los, P. J. Sellers, D. A. Dazlich, C. J. Tucker, and D. A. Randall, 2000: Sensitivity of climate to changes in NDVI. *J. Clim.*, **13**, 2277–2292.

Bounoua, L., G. J. Collatz, P. J. Sellers, D. A. Randall, D. A. Dazlich, S. O. Los, J. A. Berry, I. Fung, C. J. Tucker, C. B. Field, and T. G. Jensen, 1999: Interactions between vegetation and climate: Radiative and physiological effects of doubled atmospheric CO2. *J. Clim.*, **12**, 309–324.

Bounoua, L., R. DeFries, G. J. Collatz, P. Sellers, and H. Khan, 2002: Effects of land cover conversion on surface climate. *Clim. Change*, **52**, 29–64.

Bowling, L. C., D. P. Lettenmaier, B. Nijssen, L. P. Graham, D. B. Clark, M. E. Maayar, R. Essery, S. Goers, Y. M. Gusev, F. Habets, B. van den Hurk, J. M. Jin, D. Kahan, D. Lohmann, X. Y. Ma, S. Mahanama, D. Mocko, O. Nasonova, G. Y. Niu, P. Samuelsson, A. B. Shmakin, K. Takata, D. Verseghy, P. Viterbo, Y. L. Xia, Y. K. Xue, and Z. L. Yang, 2003a: Simulation of high-latitude hydrological processes in the Torne-Kalix basin: PILPS phase 2(e) - 1: Experiment description and summary intercomparisons. *Glob. Planet. Change*, **38**, 1–30.

Bowling, L. C., D. P. Lettenmaier, B. Nijssen, J. Polcher, R. D. Koster, and D. Lohmann, 2003b: Simulation of high-latitude hydrological processes in the Torne-Kalix basin: PILPS phase 2(e) - 3: Equivalent model representation and sensitivity experiments. *Glob. Planet. Change*, **38**, 55–71.

Buermann, W., B. Anderson, C. J. Tucker, R. E. Dickinson, W. Lucht, C. S. Potter, and R. B. Myneni, 2003: Interannual covariability in Northern Hemisphere air temperatures and greenness associated with El Nin o-Southern Oscillation and the Arctic Oscillation. *Journal of Geophysical Research*, **108**, 11–1 – 11–16.

Buermann, W., J. R. Dong, X. B. Zeng, R. B. Myneni, and R. E. Dickinson, 2001: Evaluation of the utility of satellite-based vegetation leaf area index data for climate simulations. *J. Clim.*, **14**, 3536–3550.

Canadell, J. G., H. A. Mooney, D. D. Baldocchi, J. A. Berry, J. R. Ehleringer, C. B. Field, S. T. Gower, D. Y. Hollinger, J. E. Hunt, R. B. Jackson, S. W. Running, G. R. Shaver, W. Steffen, S. E. Trumbore, R. Valentini, and B. Y. Bond, 2000: Carbon metabolism of the terrestrial biosphere: A multitechnique approach for improved understanding. *Ecosystems*, **3**, 115–130.

Champeaux, J.-L., D. Arcos, E. Bazile, D. Giard, J.-P. Goutorbe, F. Habets, J. Noilhan, and J.-L. Roujean, 2000: AHVRR-derived vegetation mapping over Western Europe for use in Numerical Weather Prediction models. *Int. J. Remote Sensing*, **21**, 1183–1199.

Charney, J., W. J. Quirk, S.-H. Chow, and J. Kornfield, 1977: A comparative study of the effects of albedo change on drought in semi arid regions. *Journal of the Atmospheric Sciences*, **34**, 1366–1385.

Chase, T. N., R. A. Pielke, T. G. F. Kittel, R. R. Nemani, and S. W. Running, 2000: Simulated impacts of historical land cover changes on global climate in northern winter. *Clim. Dyn.*, **16**, 93–105.

Chen, F., R. A. Pielke, and K. Mitchell, 2001: *Land surface hydrology, meteorology, and climate: observations and modeling. Water science and application.*. Vol. 3. American Geophysical Union, Washington, 107-135 pp.

Chen, T. H., A. Henderson-Sellers, P. C. D. Milly, A. J. Pitman, A. C. M. Beljaars, J. Polcher, F. Abramopoulos, A. Boone, S. Chang, F. Chen, Y. Dai, C. E. Desborough, R. E. Dickinson, L. Dumenil, M. Ek, J. R. Garratt, N. Gedney, Y. M. Gusev, J. Kim, R. Koster, E. A. Kowalczyk, K. Laval, J. Lean, D. Lettenmaier, X. Liang, J. F. Mahfouf, H. T. Mengelkamp, K. Mitchell, O. N. Nasonova, J. Noilhan, A. Robock, C. Rosenzweig, J. Schaake, C. A. Schlosser, J. P. Schulz, Y. Shao, A. B. Shmakin, D. L. Verseghy,

P. Wetzel, E. F. Wood, Y. Xue, Z. L. Yang, and Q. Zeng, 1997: Cabauw experimental results from the project for intercomparison of land-surface parameterization schemes. *J. Clim.*, **10**, 1194–1215.

Cihlar, J., D. Manak, and N. Voisin, 1994: AVHRR bidirectional reflectance effects and compositing. *Remote Sens. Environ.*, **48**, 77–88.

Ciret, C., and A. Henderson-Sellers, 1997: Sensitivity of global vegetation models to present-day climate simulated by global climate models. *Glob. Biogeochem. Cycle*, **11**, 415–434.

Clapp, R. B., and G. M. Hornberger, 1978: Empirical equations for some soil hydraulic properties. *Water Resour. Res.*, **14**, 601–604.

Collatz, G. J., L. Bounoua, S. O. Los, D. A. Randall, I. Y. Fung, and P. J. Sellers, 2000: A mechanism for the influence of vegetation on the response of the diurnal temperature range to changing climate. *Geophys. Res. Lett.*, **27**, 3381–3384.

Cox, P. M., 2001: Description of the TRIFFID dynamic global vegetation model. Tech. Rep. 24, Hadley Center, Bracknell, U.K.

Cox, P. M., R. A. Betts, C. B. Bunton, R. L. H. Essery, P. R. Rowntree, and J. Smith, 1999: The impact of new land surface physics on the GCM simulation of climate and climate sensitivity. *Clim. Dyn.*, **15**, 183–203.

Cox, P. M., R. A. Betts, C. D. Jones, S. A. Spall, and I. J. Totterdell, 2000: Acceleration of global warming due to carbon-cycle feedbacks in a coupled climate model. *Nature*, **408**, 184–187.

Cox, P. M., C. Huntingford, and R. J. Harding, 1998: A canopy conductance and photosynthesis model for use in a GCM land surface scheme. *Journal of Hydrology*, **212-213**, 79–94.

Cramer, W., A. Bondeau, F. I. Woodward, I. C. Prentice, R. A. Betts, V. Brovkin, P. M. Cox, V. Fisher, J. A. Foley, A. D. Friend, C. Kucharik, M. R. Lomas, N. Ramankutty, S. Sitch, B. Smith, A. White, and C. Young-Molling, 2001: Global response of terrestrial ecosystem structure and function to CO2 and climate change: results from six dynamic global vegetation models. *Glob. Change Biol.*, **7**, 357–373.

Dai, Y. J., X. B. Zeng, R. E. Dickinson, I. Baker, G. B. Bonan, M. G. Bosilovich, A. S. Denning, P. A. Dirmeyer, P. R. Houser, G. Y. Niu, K. W. Oleson, C. A. Schlosser, and Z. L. Yang, 2003: The Common Land Model. *Bull. Amer. Meteorol. Soc.*, **84**, 1013–1023.

Deardorff, J. W., 1978: Efficient prediction of ground surface temperature and moisture with inclusion of a layer of vegetation. *Journal of Geophysical Research*, **83**, 1889–1903.

Defila, C., and B. Clot, 2001: Phytophenological trends in Switzerland. *Int J. Biometeorol.*, **45**, 203–207.

DeFries, R. S., M. Hansen, J. R. G. Townshend, and R. Sohlberg, 1998: Global land cover classifications at 8 km spatial resolution: the use of training data derived from Landsat imagery in decision tree classifiers. *Int. J. Remote Sens.*, **19**, 3141–3168.

Denning, A. S., G. J. Collatz, C. G. Zhang, D. A. Randall, J. A. Berry, P. J. Sellers, G. D. Colello, and D. A. Dazlich, 1996: Simulations of terrestrial carbon metabolism and atmospheric CO2 in a general circulation model. 1. Surface carbon fluxes. *Tellus Ser. B-Chem. Phys. Meteorol.*, **48**, 521–542.

Denning, A. S., M. Nicholls, L. Prihodko, I. Baker, P. L. Vidale, K. Davis, and P. Bakwin, 2003: Simulated variations in atmospheric CO2 over a Wisconsin forest using a coupled ecosystem-atmosphere model. *Glob. Change Biol.*, **9**, 1241–1250.

Dickinson, R. E., 1984: Modeling evapotranspiration for three-dimensional global climate models. *Climate Processes and Climate Sensitivity*, J. E. Hansen and T. Takehashi, Eds., American Geophysical Union, Washington, 58–72.

—, 2001: Linking Ground Hydrology to Ecosystems and Carbon Cycle in a Climate Model. *Present and Future of Modeling Global Environmental Change: Toward Integrated Modeling*, T. Matsuno and H. Kida, Eds., TERRAPUB, 137–144.

Dickinson, R. E., J. A. Berry, G. B. Bonan, G. J. Collatz, C. B. Field, I. Y. Fung, M. Goulden, W. A. Hoffmann, R. B. Jackson, R. Myneni, P. J. Sellers, and M. Shaikh, 2002: Nitrogen controls on climate model evapotranspiration. *J. Clim.*, **15**, 278–295.

Dickinson, R. E., A. Henderson-Sellers, and P. J. Kennedy, 1993: Biosphere-atmosphere transfer scheme (BATS) version 1e as coupled to the NCAR community climate model. NCAR Technical Note NCAR/TN-387+STR, NCAR.

Dickinson, R. E., A. Henderson-Sellers, P. J. Kennedy, and M. F. Wilson, 1986: Biosphere-Atmosphere Transfer Scheme (BATS) for the NCAR Community Climate Model. Tech. Rep. NCAR/TN-275+STR, NCAR.

Douville, H., 2003: Assessing the influence of soil moisture on seasonal climate variability with AGCMs. *J. Hydrometeorol.*, **4**, 1044–1066.

—, 2004: Relevance of soil moisture for seasonal atmospheric predictions: is it an initial value problem? *Clim. Dyn.*, **22**, 429–446.

Ducharne, A., R. D. Koster, M. J. Suarez, M. Stieglitz, and P. Kumar, 2000: A catchment-based approach to modeling land surface processes in a general circulation model. 2. Parameter estimation and model demonstration. *Journal of Geophysical Research*, **105**, 24 823–24 838.

Ducharne, A., K. Laval, and J. Polcher, 1998: Sensitivity of the hydrological cycle to the parameterization of soil hydrology in a GCM. *Clim. Dyn.*, **14**, 307–327.

Dye, D. G., and S. N. Goward, 1993: Photosynthetically active radiation absorbed by global land vegetation in august 1984. *Int. J. Remote Sens.*, **14**, 3361–3364.

Eastman, J. L., M. B. Coughenour, and R. A. Pielke, 2001: The regional effects of CO2 and landscape change using a coupled plant and meteorological model. *Glob. Change Biol.*, **7**, 797–815.

Eltahir, E. A. B., 1998: A soil moisture rainfall feedback mechanism 1. Theory and observations. *Water Resour. Res.*, **34**, 765–776.

Falge, E., D. Baldocchi, R. Olson, P. Anthoni, M. Aubinet, C. Bernhofer, G. Burba, R. Ceulemans, R. Clement, H. Dolmani, A. Granier, P. Gross, T. Grünwald, D. Hollinger, N.-O. Jensen, G. Katulm, P. Keronen, A. Kowalski, C. T. Lai, B. E. Law, T. Meyers, J. Moncrieff, E. Moorsi, J. W. Munger, K. Pilegaard, Ü. Rannik, C. Rebmann, A. Suyker, J. Tenhunen, K. Tu, S. Verma, T. Vesala, K. Wilson, and S. Wofsy, 2001: Gap filling strategies for defensible annual sums of net ecosystem exchange. *Agricultural and Forest Meteorology*, **107**, 43–69.

FAO, 1995: A Digital Soil Map of the World. Published on CD-ROM.

Farquhar, G. D., S. V. Caemmerer, and J. A. Berry, 1980: A biochemical-model of photosynthetic CO2 assimilation in leaves of C-3 species. *Planta*, **149**, 78–90.

Foley, J. A., S. Levis, M. H. Costa, W. Cramer, and D. Pollard, 2000: Incorporating dynamic vegetation cover within global climate models. *Ecol. Appl.*, **10**, 1620–1632.

Fung, I., 2001: Modeling Carbon-Climate Interactions. *Present and Future of Modeling Global Environmental Change: Toward Integrated Modeling*, TERRAPUB, 187–194.

Gedney, N., and P. M. Cox, 2003: The sensitivity of global climate model simulations to the representation of soil moisture heterogeneity. *J. Hydrometeorol.*, **4**, 1265–1275.

Gedney, N., P. M. Cox, H. Douville, J. Polcher, and P. J. Valdes, 2000: Characterizing GCM land surface schemes to understand their responses to climate change. *J. Clim.*, **13**, 3066–3079.

Gordon, H. R., J. W. Brown, and R. H. Evans, 1988: Exact rayleigh-scattering calculations for use with the nimbus- 7 coastal zone color scanner. *Appl. Optics*, **27**, 862–871.

Goward, S. N., B. Markham, D. G. Dye, W. Dulaney, and J. L. Yang, 1991: Normalized Difference Vegetation Index measurements from the Advanced Very High-Resolution Radiometer. *Remote Sens. Environ.*, **35**, 257–277.

Guillevic, P., R. D. Koster, M. J. Suarez, L. Bounoua, G. J. Collatz, S. O. Los, and S. P. P. Mahanama, 2002: Influence of the interannual variability of vegetation on the surface energy balance - A global sensitivity study. *J. Hydrometeorol.*, **3**, 617–629.

Gutman, G., and A. Ignatov, 1995: Global land monitoring from AVHRR - potential and limitations. *Int. J. Remote Sens.*, **16**, 2301–2309.

Halldin, S., S.-E. Gryning, L. Gottschalk, A. Jochum, L.-C. Lundin, and A. A. van de Griend, 1999: Energy, water and carbon exchange in a boreal forest landscape - NOPEX experiences. *Agricultural and Forest Meteorology*, **98-99**, 5–29.

Hansen, M. C., R. Defries, J. R. G. Townshend, and R.Sohlberg, 2000: Global land cover classification at 1km spatial resolution using a classification tree approach. *Int. J. Remote Sensing*, **21**, 1331–1364.

Heck, P., D. Luthi, and C. Schär, 1999: The influence of vegetation on the summertime evolution of European soil moisture. *Phys. Chem. Earth (B) -Hydrol. Oceans Atmos.*, **24**, 609–614.

Heck, P., D. Luthi, H. Wernli, and C. Schär, 2001: Climate impacts of European-scale anthropogenic vegetation changes: A sensitivity study using a regional climate model. *J. Geophys. Res.-Atmos.*, **106**, 7817–7835.

Henderson-Sellers, A., P. Irannejad, K. McGuffie, and A. J. Pitman, 2003: Predicting land-surface climates - better skill or moving targets? *Geophys. Res. Lett.*, **30**, art. no.–1777.

Hirschi, M., S. I. Seneviratne, and C. Schär, 2006: Seasonal variations in terrestrial water storage for major mid-latitude river basins. *Journal of Hydrometeorology*, **7**, 39–60.

Holben, B. N., 1986: Characteristics of maximum-value composite images from temporal AVHRR data. *Int. J. Remote Sens.*, **7**, 1417–1434.

Holtslag, A. A. M., and M. Ek, 1996: Simulation of surface fluxes and boundary layer development over the pine forest in HAPEX-MOBILHY. *Journal of Applied Meteorology*, **35**, 202–213.

Hurrell, J. W., 1995: Decadal trends in the north-atlantic oscillation - regional temperatures and precipitation. *Science*, **269**, 676–679.

Idso, S. B., 1981: A set of equations for full spectrum and 8-mu-m to 14-mu-m and 10.5-mu-m to 12.5-mu-m thermal-radiation from cloudless skies. *Water Resour. Res.*, **17**, 295–304.

Intergovernmental Panel on Climate Change, 2001: *Climate Change 2001: The Scientific Basis. Contribution of Working Group I to the Third Assessment Report of the Intergovernmental panel on Climate Change*. Cambridge University Press, Cambridge.

James, M. E., and S. N. V. Kalluri, 1994: The pathfinder AVHRR land data set - an improved coarse resolution data set for terrestrial monitoring. *Int. J. Remote Sens.*, **15**, 3347–3363.

Jarvis, P. G., 1976: The interpretation of the variations in leaf water potential and stomatal conductance found in canopies in the field. *Philosophical Transactions of the Royal Society of London, Series B*, **273**, 593–610.

Justice, C. O., J. R. G. Townshend, B. N. Holben, and C. J. Tucker, 1985: Analysis of the phenology of global vegetation using meteorological satellite data. *Int. J. Remote Sens.*, **6**, 1271–1318.

Keeling, C. D., J. F. S. Chin, and T. P. Whorf, 1996: Increased activity of northern vegetation inferred from atmospheric CO2 measurements. *Nature*, **382**, 146–149.

Kim, W., T. Arai, S. Kanae, T. Oki, and K. Musiake, 2001: Application of the simple biosphere model (SiB2) to a paddy field for a period of growing season in GAME-Tropics. *J. Meteorol. Soc. Jpn.*, **79**, 387–400.

Koster, R. D., and P. C. D. Milly, 1997: The interplay between transpiration and runoff formulations in land surface schemes used with atmospheric models. *J. Clim.*, **10**, 1578–1591.

Koster, R. D., and M. J. Suarez, 1992: Modeling the land surface boundary in climate models as a composite of independent vegetation stands. *J. Geophys. Res.*, **97**, 2697–2715.

—, 2001: Soil moisture memory in climate models. *J. Hydrometeorol.*, **2**, 558–570.

Koster, R. D., M. J. Suarez, A. Ducharne, M. Stieglitz, and P. Kumar, 2000a: A catchment-based approach to modeling land surface processes in a general circulation model. 1. model structure. *Journal of Geophysical Research*, **105**, 24 809–24 822.

Koster, R. D., M. J. Suarez, and M. Heiser, 2000b: Variance and predictability of precipitation at seasonal-to- interannual timescales. *J. Hydrometeorol.*, **1**, 26–46.

Lettenmaier, D. P., 2001: Macroscale Hydrology: Challenges and Opportunities. *Present and Future of Modeling Global Environmental Change: Toward Integrated Modeling*, TERRAPUB, 111–136.

Levis, S., J. A. Foley, and D. Pollard, 2000: Large-scale vegetation feedbacks on a doubled CO2 climate. *J. Clim.*, **13**, 1313–1325.

Liang, X., E. F. Wood, D. P. Lettenmaier, D. Lohmann, A. Boone, S. Chang, F. Chen, Y. Dai, C. Desborough, R. E. Dickinson, Q. Duan, M. Ek, Y. M. Gusev, F. Habets, P. Irannejad, R. Koster, K. E. Mitchell, O. N. Nasonova, J. Noilhan, J. Schaake, A. Schlosser, Y. Shao, A. B. Shmakin, D. Verseghy, K. Warrach, P. Wetzel, Y. Xue, Z.-L. Yang, and Q.-C. Zeng, 1998: The Project for Intercomparison of Land-surface Parameterization Schemes PILPS phase 2c Red-Arkansas River basin experiment: 2. Spatial and temporal analysis of energy fluxes. *Global and Planetary Change*, **19**, 137–159.

Liang, X., and Z. Xie, 2001: A new surface runoff parameterization with subgrid-scale soil heterogeneity for land surface models. *Advances in Water Resources*, **24**, 1173–1193.

Lohmann, D., D. P. Lettenmaier, X. Liang, E. F. Wood, A. Boone, S. Chang, F. Chen, Y. Dai, C. Desborough, R. E. Dickinson, Q. Duan, M. Ek, Y. M. Gusev, F. Habets, P. Irannejad, R. Koster, K. E. Mitchell, O. N. Nasonova, J. Noilhan, J. Schaake, A. Schlosser, Y. Shao, A. B. Shmakin, D. Verseghy, K. Warrach, P. Wetzel, Y. Xue, Z.-L. Yang, and Q.-C. Zeng, 1998: The Project for Intercomparison of Land-surface Parameterization Schemes PILPS phase 2c Red-Arkansas River basin experiment: 3. Spatial and temporal analysis of water fluxes. *Global and Planetary Change*, **19**, 161–179.

Los, S. O., 1998: Linkages between global vegetation and climate: an analysis based on NOAA-Advanced Very High Resolution Radiometer Data. Ph.D. dissertation, Vrije Universiteit, Amsterdam.

Los, S. O., G. J. Collatz, L. Bounoua, P. J. Sellers, and C. J. Tucker, 2001: Global interannual variations in sea surface temperature and land surface vegetation, air temperature, and precipitation. *J. Clim.*, **14**, 1535–1549.

Los, S. O., G. J. Collatz, P. J. Sellers, C. M. Malmstrom, N. H. Pollack, R. S. DeFries, L. Bounoua, M. T. Parris, C. J. Tucker, and D. A. Dazlich, 2000: A global 9-yr biophysical land surface dataset from NOAA AVHRR data. *J. Hydrometeorol.*, **1**, 183–199.

Loveland, T. R., B. C. Reed, J. F. Brown, D. O. Ohlen, Z. Zhu, L. Yang, and J. W. Merchants, 2000: Development of a global land cover characteristics database and IGBP DISCover from 1km AVHRR data. *Int. J. Remote Sensing*, **21**, 1303–1330.

Manabe, S., 1969: Climate and the ocean circulation. 1 The atmospheric circulation and the hydrology of the earth's surface. *Monthly Weather Review*, **97**, 739–774.

Matthews, E., 1983: Global vegetation and land-use - new high-resolution data-bases for climate studies. *J. Clim. Appl. Meteorol.*, **22**, 474–487.

McCaughey, J. H., P. M. Lafleur, D. W. Joiner, P. A. Bartlett, A. M. Costello, D. E. Jelinski, and M. G. Ryan, 1997: Magnitudes and seasonal patterns of energy, water, and carbon exchanges at a boreal young jack pine forest in the BOREAS northern study area. *J. Geophys. Res.-Atmos.*, **102**, 28 997–29 007.

Menzel, A., 2000: Trends in phenological phases in Europe between 1951 and 1996. *Int. J. Biometeorol.*, **44**, 76–81.

Milly, P. C. D., and K. A. Dunne, 1994: Sensitivity of the global water cycle to the water-holding capacity of land. *J. Clim.*, **7**, 506–526.

Moncrieff, J. B., J. M. Massheder, H. de Bruin, J. Elbers, T. Friborg, H. Heusinkveld, P. Kabat, S. Scott, H. Soegaard, and A. Verhoef, 1997: A system to measure surface fluxes of momentum, sensible heat, water vapour and carbon dioxide. *Journal of Hydrology*, **188-189**, 589–611.

Moulin, S., L. Kergoat, N. Viovy, and G. Dedieu, 1997: Global-scale assessment of vegetation phenology using NOAA/AVHRR satellite measurements. *J. Clim.*, **10**, 1154–1170.

Myneni, R. B., C. D. Keeling, C. J. Tucker, G. Asrar, and R. R. Nemani, 1997: Increased plant growth in the northern high latitudes from 1981 to 1991. *Nature*, **386**, 698–702.

Nijssen, B., L. C. Bowling, D. P. Lettenmaier, D. B. Clark, M. E. Maayar, R. Essery, S. Goers, Y. M. Gusev, F. Habets, B. van den Hurk, J. M. Jin, D. Kahan, D. Lohmann, X. Y. Ma, S. Mahanama, D. Mocko, O. Nasonova, G. Y. Niu, P. Samuelsson, A. B. Schmakin, K. Takata, D. Verseghy, P. Viterbo, Y. L. Xia, Y. K. Xue, and Z. L. Yang, 2003: Simulation of high latitude hydrological processes in the Torne-Kalix basin: PILPS phase 2(e) - 2: Comparison of model results with observations. *Glob. Planet. Change*, **38**, 31–53.

Niu, G. Y., and Z. L. Yang, 2003: The versatile integrator of surface atmospheric processes - Part 2: evaluation of three topography-based runoff schemes. *Glob. Planet. Change*, **38**, 191–208.

Noilhan, J., P. Lacarre, A. J. Dolman, and E. M. Blyth, 1997: Defining area-average parameters in meteorological models for land surfaces with mesoscale heterogeneity. *Journal of Hydrology*, **190**, 302–316.

Parton, W. J., M. Hartman, D. Ojima, and D. Schimel, 1998: DAYCENT and its land surface submodel: description and testing. *Global and Planetary Change*, **19**, 35–48.

Petit, J. R., J. Jouzel, D. Raynaud, N. I. Barkov, J. M. Barnola, I. Basile, M. Bender, J. Chappellaz, M. Davis, G. Delaygue, M. Delmotte, V. M. Kotlyakov, M. Legrand, V. Y. Lipenkov, C. Lorius, L. Pepin, C. Ritz, E. Saltzman, and M. Stievenard, 1999: Climate and atmospheric history of the past 420,000 years from the Vostok ice core, Antarctica. *Nature*, **399**, 429–436.

Pielke Sr, R. A., 2001a: Earth System Modeling–An Integrated Assessment Tool for Environmental Studies. *Present and Future of Modeling Global Environmental Change: Toward Integrated Modeling*, TERRAPUB, 311–337.

—, 2001b: Influence of the spatial distribution of vegetation and soils on the prediction of cumulus convective rainfall. *Reviews of Geophysics*, **39**, 151–177.

Pielke Sr, R. A., G. E. Liston, J. L. Eastman, and L. Lu, 1999: Seasonal weather prediction as an initial value problem. *Journal of Geophysical Research*, **104**, 19 463–19 479.

Pitman, A. J., 2003: Review the evolution of, and revolution in, land surface schemes designed for climate models. *International Journal of Climatology*, **23**, 479–510.

Pitman, A. J., and A. Henderson-Sellers, 1998: Recent progress and results from the project for the intercomparison of landsurface parameterization schemes. *J. Hydrol.*, **213**, 128–135.

Pitman, A. J., A. Henderson-Sellers, C. E. Desborough, Z. L. Yang, F. Abramopoulos, A. Boone, R. E. Dickinson, N. Gedney, R. Koster, E. Kowalczyk, D. Lettenmaier, X. Liang, J. F. Mahfouf, J. Noilhan, J. Polcher, W. Qu, A. Robock, C. Rosenzweig, C. A. Schlosser, A. B. Shmakin, J. Smith, M. Suarez, D. Verseghy, P. Wetzel, E. Wood, and Y. Xue, 1999: Key results and implications from phase 1(c) of the Project for Intercomparison of Land-Surface Parametrization Schemes. *Clim. Dyn.*, **15**, 673–684.

Polcher, J., B. McAvaney, P. Viterbo, M.-A. Gaertner, A. Hahmann, J.-F. Mahfouf, J. Noilhan, T. Phillips, A. Pitman, C. A. Schlosser, J.-P. Schulz, B. Timbal, D. Verseghy, and Y. Xue, 1998: A proposal for a general interface between land surface schemes and general circulation models. *Global and Planetary Change*, **19**, 261–276.

Post, E., and N. C. Stenseth, 1999: Climatic variability, plant phenology, and northern ungulates. *Ecology*, **80**, 1322–1339.

Randall, D. A., D. A. Dazlich, C. Zhang, A. S. Denning, P. J. Sellers, C. J. Tucker, L. Bounoua, S. O. Los, C. O. Justice, and I. Fung, 1996: A revised land surface parameterization (SiB2) for GCMs .3. The greening of the Colorado State University general circulation model. *J. Clim.*, **9**, 738–763.

Randerson, J. T., F. S. Chapin, J. W. Harden, J. C. Neff, and M. E. Harmon, 2002: Net ecosystem production: A comprehensive measure of net carbon accumulation by ecosystems. *Ecol. Appl.*, **12**, 937–947.

Rao, C. R. N., and J. H. Chen, 1996: Post-launch calibration of the visible and near-infrared channels of the advanced very high resolution radiometer on the NOAA-14 spacecraft. *Int. J. Remote Sens.*, **17**, 2743–2747.

Reale, O., and P. Dirmeyer, 2000: Modeling the effects of vegetation on Mediterranean climate during the Roman Classical Period Part I: Climate history and model sensitivity. *Glob. Planet. Change*, **25**, 163–184.

Reale, O., and J. Shukla, 2000: Modeling the effects of vegetation on Mediterranean climate during the Roman Classical Period: Part II. Model simulation. *Glob. Planet. Change*, **25**, 185–214.

Reed, B. C., J. F. Brown, D. Vanderzee, T. R. Loveland, J. W. Merchant, and D. O. Ohlen, 1994: Measuring phenological variability from satellite imagery. *J. Veg. Sci.*, **5**, 703–714.

Roetzer, T., M. Wittenzeller, H. Haeckel, and J. Nekovar, 2000: Phenology in central Europe - differences and trends of spring phenophases in urban and rural areas. *Int. J. Biometeorol.*, **44**, 60–66.

Running, S. W., D. D. Baldocchi, D. P. Turner, S. T. Gower, P. S. Bakwin, and K. A. Hibbard, 1999: A Global Terrestrial Monitoring Network Integrating Tower Fluxes, Flask Sampling, Ecosystem Modeling and EOS Satellite Data. *Remote Sens. Environ.*, **70**, 108–127.

Running, S. W., R. R. Nemani, F. A. Heinsch, M. S. Zhao, M. Reeves, and H. Hashimoto, 2004: A continuous satellite-derived measure of global terrestrial primary production. *Bioscience*, **54**, 547–560.

Sato, N., P. J. Sellers, D. A. Randall, E. K. Schneider, J. Shukla, J. Kinter, Y.-T. Hou, and E. R. Albertazzi, 1989a: Effects of implementing the Simple Biosphere model (SiB) in a GCM: Methodology and results. Tech. Rep., NASA HQ, Independence Avenue, Washington, D.C. 20545, USA.

Sato, N., P. J. Sellers, D. A. Randall, E. K. Schneider, J. Shukla, J. L. Kinter, Y. T. Hou, and E. Albertazzi, 1989b: Effects of implementing the simple biosphere model in a general-circulation model. *J. Atmos. Sci.*, **46**, 2757–2782.

Schär, C., D. Luthi, and U. Beyerle, 1999: The Soil-Precipitation Feedback: A Process Study with a Regional Climate Model. *Journal of Climate*, **12**, 722–741.

Schmid, H. P., H. B. Su, C. S. Vogel, and P. S. Curtis, 2003: Ecosystem-atmosphere exchange of carbon dioxide over a mixed hardwood forest in northern lower Michigan. *J. Geophys. Res.-Atmos.*, **108**, art. no.–4417.

Sellers, P. J., L. Bounoua, G. J. Collatz, D. A. Randall, D. A. Dazlich, S. O. Los, J. A. Berry, I. Fung, C. J. Tucker, C. B. Field, and T. G. Jensen, 1996a: Comparison of radiative and physiological effects of doubled atmospheric CO2 on climate. *Science*, **271**, 1402–1406.

Sellers, P. J., R. E. Dickinson, D. A. Randall, A. K. Betts, F. Hall, J. Berry, G. Collatz, A. Denning, H. Mooney, C. Nobre, N. Sato, C. Field, and A. Henderson-Sellers, 1997a: Modeling the Exchanges of Energy, Water, and Carbon between Continents and the Atmosphere. *Science*, **275**, 502–509.

Sellers, P. J., F. G. Hall, G. Asrar, D. E. Strebel, and R. E. Murphy, 1988: The 1st ISLSCP field experiment (FIFE). *Bull. Amer. Meteorol. Soc.*, **69**, 22–27.

Sellers, P. J., F. G. Hall, R. D. Kelly, A. Black, D. Baldocchi, J. Berry, M. Ryan, K. J. Ranson, P. M. Crill, D. P. Lettenmaier, H. Margolis, J. Cihlar, J. Newcomer, D. Fitzjarrald, P. G. Jarvis, S. T. Gower, D. Halliwell, D. Williams, B. Goodison, D. E. Wickland, and F. E. Guertin, 1997b: BOREAS in 1997: Experiment overview, scientific results, and future directions. *J. Geophys. Res.-Atmos.*, **102**, 28 731–28 769.

Sellers, P. J., S. O. Los, C. J. Tucker, C. O. Justice, D. A. Dazlich, G. J. Collatz, and D. A. Randall, 1996b: A revised land surface parameterization (SiB2) for atmospheric GCMs .2. The generation of global fields of terrestrial biophysical parameters from satellite data. *J. Clim.*, **9**, 706–737.

Sellers, P. J., B. W. Meeson, J. Closs, J. Collatz, F. Corprew, D. Dazlich, F. G. Hall, Y. Kerr, R. Koster, S. Los, K. Mitchell, J. McManus, D. Myers, K. J. Sun, and P. Try, 1996c: The ISLSCP initiative I global datasets: Surface boundary conditions and atmospheric forcings for land-atmosphere studies. *Bull. Amer. Meteorol. Soc.*, **77**, 1987–2005.

Sellers, P. J., Y. Mintz, Y. C. Sud, and A. Dalcher, 1986: A Simple Biosphere model (SiB) for use within general circulation models. *Journal of the Atmospheric Sciences*, **43**, 505–531.

Sellers, P. J., D. A. Randall, G. J. Collatz, J. A. Berry, C. B. Field, D. A. Dazlich, C. Zhang, G. D. Collelo, and L. Bounoua, 1996d: A revised land surface parameterization (SiB2) for atmospheric GCMs .1. Model formulation. *J. Clim.*, **9**, 676–705.

Seneviratne, S. I., J. S. Pal, E. A. B. Eltahir, and C. Schär, 2002: Summer dryness in a warmer climate: a process study with a regional climate model. *Clim. Dyn.*, **20**, 69–85.

Seneviratne, S. I., P. Viterbo, D. Luthi, and C. Schär, 2004: Inferring changes in terrestrial water storage using ERA-40 reanalysis data: The Mississippi River basin. *Journal of Climate*, **17**, 2039–2057.

Shukla, J., and Y. Mintz, 1982: Influence of land-surface evaporation on the Earth's climate. *Science*, **215**, 1498–1501.

Stieglitz, M., D. Rind, J. Famiglietti, and C. Rosenzweig, 1997: An efficient approach to modeling the topographic control of surface hydrology for regional and global climate modeling. *J. Clim.*, **10**, 118–137.

Stöckli, R., and P. L. Vidale, 2004: European plant phenology and climate as seen in a 20-year AVHRR land-surface parameter dataset. *Int. J. Remote Sens.*, **25**, 3303–3330.

—, 2005: Modeling diurnal to seasonal water and heat exchanges at European Fluxnet sites. *Theor. Appl. Climatol.*, **80**, 229–243.

Stöckli, R., P. L. Vidale, A. Boone, M. Hirschi, and C. Schär, in preparation: Sensitivity of the diurnal and seasonal course of modeled runoff to three different land surface model soil moisture parameterizations. *J. Hydrometeorol.*.

Tucker, C. J., 1979: Red and photographic infrared linear combinations for monitoring vegetation. *Remote Sens. Environ.*, **8**, 127–150.

Tucker, C. J., and M. Matson, 1985: Determination of volcanic dust deposition from El-Chichon using ground and satellite data. *Int. J. Remote Sens.*, **6**, 619–627.

Tucker, C. J., and P. J. Sellers, 1986: Satellite remote-sensing of primary production. *Int. J. Remote Sens.*, **7**, 1395–1416.

Turner, D. P., S. V. Ollinger, and J. S. Kimball, 2004: Integrating remote sensing and ecosystem process models for landscape- to regional-scale analysis of the carbon cycle. *Bioscience*, **54**, 573–584.

v. Humboldt, A., 1817: *De Distributione Geographica Plantarum - secundum coeli temperiem et altitudinem montium, prolegomena*. Lutetiae Parisorum (Paris).

—, 1849: *Ansichten der Natur, mit wissenschaftlichen Erläuterungen*. Cotta, Stuttgart.

Vermote, E. F., N. ElSaleous, C. O. Justice, Y. J. Kaufman, J. L. Privette, L. Remer, J. C. Roger, and D. Tanre, 1997: Atmospheric correction of visible to middle-infrared EOS-MODIS data over land surfaces: Background, operational algorithm and validation. *J. Geophys. Res.-Atmos.*, **102**, 17 131–17 141.

Vidale, P. L., D. Luthi, C. Frei, S. I. Seneviratne, and C. Schär, 2003: Predictability and uncertainty in a regional climate model. *J. Geophys. Res.-Atmos.*, **108**, art. no.–4586.

Vidale, P. L., and R. Stöckli, 2005: Prognostic canopy air space solutions for land surface exchanges. *Theor. Appl. Climatol.*, **80**, 245–257.

Viovy, N., and G. Saint, 1994: Hidden markov-models applied to vegetation dynamics analysis using satellite remote-sensing. *IEEE Trans. Geosci. Remote Sensing*, **32**, 906–917.

Viterbo, P., A. Beljaars, J. F. Mahfouf, and J. Teixeira, 1999: The representation of soil moisture freezing and its impact on the stable boundary layer. *Q. J. R. Meteorol. Soc.*, **125**, 2401–2426.

Walko, R. L., L. E. Band, J. Baron, T. G. F. Kittel, R. Lammers, T. J. Lee, D. Ojima, R. A. Pielke, C. Taylor, C. J. Tremback, P. L. Vidale, and C. Tague, 2000: Coupled Atmosphere-Biophysics-Hydrology models for Environmental Modeling. *Journal of Applied Meteorology*, **39**, 931–944.

Western, A. W., R. B. Grayson, and G. Blosch, 2002: Scaling of soil moisture: a hydrologyic perspective. *Annual Reviews of Earth Planetary Science*, **30**, 149–180.

Wilson, K., A. Goldstein, E. Falge, M. Aubinet, D. Baldocchi, P. Berbigier, C. Bernhofer, R. Ceulemans, H. Doplman, C. Field, A. Grelle, A. Kowalski, T. Meyers, J. M¡oncrieff, R. Monson, W. Oechel, J. Tenhunen, R. Valentini, and S. Verma, 2002: Energy balance closure at FLUXNET sites. *Agricultural and Forest Meteorology*, **113**, 223–243.

Wilson, M. F., and A. Henderson-Sellers, 1985: A global archive of land cover and soils data for use in general-circulation climate models. *J. Climatol.*, **5**, 119–143.

Wolock, D. M., and G. J. McCabe, 2000: Differences in topographic characteristics computed from 100- and 1000-m resolution digital elevation model data. *Hydrol. Process.*, **14**, 987–1002.

Wood, E. F., D. P. L. adn X. Liang, D. Lohmann, A. Boone, S. Chang, F. Chen, Y. Dai, R. E. Dickinson, Q. Duan, M. Ek, Y. M. Gusev, F. Habets, P. Irannejad, R. Koster, K. E. Mitchell, O. N. Nasonova, J. Noilhan, J. Schaake, A. Schlosser, Y. Shao, A. B. Shmakin, D. Verseghy, K. Warrach, P. Wetzel, Y. Xue, Z.-L. Yang, and Q.-C. Zeng, 1998: The Project for Intercomparison of Land-surface Parameterization Schemes PILPS Phase 2c Red-Arkansas River basin experiment: 1. Experiment description and summary intercomparisons. *Global and Planetary Change*, **19**, 115–135.

Wu, W., M. A. Geller, and R. E. Dickinson, 2002: A case study for land model evaluation: Simulation of soil moisture amplitude damping and phase shift. *Journal of Geophysical Research*, **107**, 4793.

Yang, Z.-L., and G.-Y. Niu, 2003: The versatile integrator of surface atmospheric processes - Part 1: Model description. *Glob. Planet. Change*, **38**, 175–189.

Zeng, X. B., 2001: Global vegetation root distribution for land modeling. *J. Hydrometeorol.*, **2**, 525–530.

Zheng, X., and E. A. B. Eltahir, 1998: A soil moisture-rainfall feedback mechanism 2. Numerical experiments. *Water Resour. Res.*, **34**, 777–785.

Zhou, L. M., C. J. Tucker, R. K. Kaufmann, D. Slayback, N. V. Shabanov, and R. B. Myneni, 2001: Variations in northern vegetation activity inferred from satellite data of vegetation index during 1981 to 1999. *J. Geophys. Res.-Atmos.*, **106**, 20 069–20 083.

Acknowledgements

As the Nobel museum in Stockholm presents in its exhibition "Cultures of Creativity", science is a creative activity, and can only happen in creative environments such as informal discussions at the coffee break, mountain hikes far from conference halls and in a milieu which is supported by manifold social interactions. I have been in such an environment during my PhD thesis and I would like to thank everyone who contributed to it.

First of all, I would like to express my gratitude to Christoph Schär for accepting me as a PhD student after I conducted my diploma thesis in his group. He has been a very open-minded supporter for my research ideas, which have taken me on a somewhat remote "exploration" path away the institute's backyard. I therefore greatly appreciate his responsibility and guidance, which helped me to stay focused on my scientific track.

I am most grateful to Pier Luigi Vidale, who guided my diploma and PhD thesis and provided a substantial part of the creative environment for this work. His broad scientific background and his extraordinary knowledge in the field of my study made him an highly competent supervisor for my thesis. I greatly appreciate his social skills and his sense of humor, especially when it comes to politics or NASA's EOS program. I am in depth to him for his readiness, and the time he spent in reviewing, discussing and guiding my work. I look forward to continue such a productive scientific work relationship with him.

My co-examiner Hans Peter Schmid has provided invaluable insights into the ecosystem measurement world, which were helpful for our collaborative work, and I would like to thank him for supporting the idea of integrating satellite remote sensing, ecosystem measurement and modeling techniques, this being the main focus my thesis.

Special thanks go to Dani Lüthi and Martin Hirschi for their knowledgeable management of our computing ressources, and for accepting my special needs to host the numerous NASA-owned machines in our Institute.

I would like to acknowledge my friends at the NASA Goddard Space Flight Center, especially Fritz Hasler, who, back in 1998, gave me the possibility to stay in his group for a five month lasting internship, and to Michael King, Yoram Kaufman and David Herring, for supporting and guiding my visualization work during the past years. This wouldn't have been possible without the financial support of my contractor company SSAI (Science Systems and Applications Inc.). My team members at Goddard, Craig, Cathy, Jacques, Jesse, George, Lisa, Marit, Mark, Rob, Ted, Vicky and many others receive many thanks for the creative environment we share in our projects.

The fruitful collaboration with NASA's Earth Science community was not limited to visualization of satellite remote sensing products, but a number scientists of NASA's EOS project have substantially influenced my scientific thinking and therefore this PhD thesis. I owe great thanks for discussions and helpful ideas to Jim Collatz, Steve Running, Jim Tucker, Eric Vermote and Sietse Los. Although I have neither seen nor talked to him, but science by Piers Sellers has greatly driven this work and I would like to thank him for turning the land surface, as used in climate research, from a physical to an interdisciplinary science as we have it today.

I highly appreciate and honor the contribution of data and models used in this study. Firstly, most sincere thanks to Scott Denning and his group at CSU, for sharing the SiB 2 model code and related utilities with us and for the possibility to contribute to its development with new ideas. Then, numerous thanks go to the FLUXNET community (Richard Olson and Eva Falge) and the Rhone-AGG initiative (Aaron Boone and Florence Habets) for providing ecosystem measurement datasets of high quality, which were a substantial back-bone for this study.

Many institute members and friends contributed directly or indirectly to this study. I particularly would like to thank Oliver Fuhrer, my flatmate, who deliberately motivated me for hiking and skiing trips when work deadlines were requesting otherwise. His positive worldview should be guidance for any social and scientific interaction. Many thanks go to the other "7Up" flatmates for providing such a great creative environment at home. Whether it was on drinking a strong espresso coffee at midnight, cleaning bathrooms, a discussion on grappa or a week of great windsurfing, it all directly contributed to this work, and I can't remove it from there! Greatest thanks go to Sonia Seneviratne for funny, extravagant and long discussions on land surface modeling utopia. I would like to express my warmest thanks to Sibylle Dueri, I highly appreciate her nice friendship and her tolerant worldview and am grateful for her support during the last part of my thesis. Nele Rogiers receives many thanks since she has been a great friend during the last year, and our crazy freetime projects have motivated for an exquisite scientific collaboration, and I look forward to continue it.

Finally and most importantly, I feel indebted to my parents, Lotti and Josef Stöckli and my sister Sibylle, for their love and support during all these years. They provided the necessary "solid ground", which is important in a turbulent world, and a social environment, which allowed me to focus on the science quest for which I am up to.

Curriculum Vitae

Reto Stöckli, Stampfenbachstr. 151, 8006 Zürich
born on 15 July 1973 in Wolhusen; citizen of Luthern LU

Education and Professional Training

Jul 2000 – Sep 2004	Ph. D. student in the group of Prof. C. Schär, at the Institute for Atmospheric and Climate Science, ETH Zürich, Switzerland.
Apr 1998 – present	Visualization of satellite remote sensing data for public outreach at the NASA Goddard Space Flight Center Visualization and Analysis Lab (Code 912) and at the Climate and Radiation Branch (Code 913). Team member of NASA's Earth Observatory.
Oct 1994 – Apr 2000	Studies in Environmental Sciences (atmosphere and physics) at ETH Zürich, Switzerland. Diploma thesis "Time and Space dependent Biophysical Land Surface Parameters from AVHRR NDVI Data for Use in Regional Climate Models" under the guidance of Prof. C. Schär and Dr. P. L. Vidale.
Aug 1986 – Jun 1993	Gymnasium type C in Sursee, Switzerland. Matura thesis "Radioaktivität" under the guidance of Otto Steiger.
Feb 1983 – Jul 1986	Primary School, Escola Suiço-Brasileira, Rio de Janeiro, Brazil.
Aug 1980 – Jan 1983	Primary School, Sursee, Switzerland.

International Conferences and Workshops

EGU General Assembly, 2000, 2001, 2003 and 2004, Nice (France); AMS Annual Meeting, 2003, Long Beach (USA); ICTP Conference and Workshop on Climate Variability and Land-Surface Processes, 2001, Trieste (IT); AQUA satellite workshop, 2003, Greenbelt (USA); MODIS Vegetation Workshop II, 2004, Missoula (USA); CO2 and Water Workshop, 2002, Basel; Satellitenmeteorologie und NWP Workshop Meteoschweiz, 2002, Zürich